Doctoral Thesis

Probabilistic Forecasting of Solar Irradiance Using a Mesoscale Meteorological Model

メソ気象予報モデルを用いた日射強度の確率予測

2016

Environmental and Renewable Energy Systems Division

Graduate School of Engineering

Gifu University

Yuanyuan Liu

ABSTRACT

Huge amount of solar photovoltaic (PV) power generation systems have been installed and connected to electric power grids in recent years. As the number of installations continues to increase, grid operators are growing increasingly worried that intermittent and uncontrolled PV generation can destabilize the electricity grid. In order to mitigate the destabilizing effect of PV generation system, the prediction of solar PV power generation or the forecasting of the solar irradiance is urgently required. The reliable forecasting information will help the grid operators for better management of the electric power balance between demand and generation. Previous studies mainly focused on the solar irradiance forecasting using the numerical weather prediction models. Detailed studies for the probabilistic forecasting of solar irradiance are very limited.

Accordingly, this study is conducted for the investigation of (1) solar irradiance forecasting by applying a meteorological model, (2) improvement of solar irradiance forecasting, (3) forecasting reliability or prediction interval forecasting of solar irradiance, and (4) the effect of the improvement of solar irradiance forecasting to the forecasting of the prediction interval. For these purposes, the Weather Research and Forecasting (WRF) model, developed by the National Centers for Atmospheric Research (NCAR) and the National Centers for Environmental Prediction (NCEP), is employed. The post-processing method Kalman Filter and ensemble forecasting method are applied in this study.

The WRF simulation on a 2km resolution grid is performed with parallelized computer cluster systems, and the accuracy and characteristic of the WRF-simulated

solar irradiance is examined using on-situ observations in the central region of Japan. Compared to the persistent model as a reference, it is clear that the WRF model has enough accuracy for the solar irradiance forecasting. On the other hand, a comparison with on-site observations exhibited that the intra-day solar irradiance simulated by WRF has a positive bias of more than +29% of the observed data. This indicates that the improvement of forecasting accuracy of simulated solar irradiance is necessary for evaluating the solar PV power generation.

In order to increase the forecasting accuracy of the WRF-simulated solar irradiance, the results are analyzed separately for the use of the univariate Kalman Filter and the multivariate Kalman Filter. The accuracy of the WRF-simulated solar irradiance for the intra-day forecasting after applying univariate Kalman Filter is finally reduced to have a bias of -2.4 W/m^2 and RMSE of 79.1 W/m^2. Due to the application of multivariate Kalman Filter, the bias on average of the WRF-simulated solar irradiance for the intra-day forecasting is removed around 99.5%, and RMSE is improved around 25%. Moreover, correlation coefficients (CORRs) of both Kalman Filters are also slightly increased.

To evaluate the forecasting reliability, the solar irradiance ensemble forecasting system is performed with the WRF model. The spread of the ensemble forecasting is calculated as a parameter corresponding to the unreliability of the forecasting, and the relationship of the spread and the forecasting error is discussed to evaluate the prediction interval. The size of the prediction interval changes with the reliability of the forecasting. The empirical coverage rates of the prediction interval are a little lower than the corresponding nominal ones in this ensemble. It may be caused by the overestimation of the solar irradiance computed with WRF. The reductions of the

empirical coverage rates from the nominal ones are about 0.3 of the nominal coverage rates, and not so large. The ensemble forecasting of solar irradiance with the prediction interval works well. Improvement of the solar irradiance forecasting may be needed to recover the reductions of the empirical coverage rates.

To improve the forecasting accuracy of the prediction interval, two bias-correction methods are applied to the solar irradiance ensemble forecasting system with the WRF model. The forecasted results with the univariate Kalman Filter and the multivariate Kalman Filter are investigated separately. As a result, through the application of Kalman Filters as the post processor of the forecasting, the sizes of the prediction intervals reduce, and the empirical coverage rates increase and approach well to the nominal coverage rates. Consequently, the improvement by applying the Kalman Filter is not only for the solar irradiance forecasting itself, but also for the prediction interval estimation in the ensemble forecasting.

Keywords: solar irradiance, meteorological model, Weather Research and Forecasting (WRF), ensemble forecasting, prediction interval, Lagged Averaged Forecast (LAF) method, spread, empirical coverage rate, nominal coverage rate, Kalman Filter

TABLE OF CONTENTS

Page

Chapter 1 Introduction

1.1 Background and objectives

It is well known that fossil fuels are limited and nonrenewable. British Petroleum (BP) statistical review of world energy 2015 pointed out the available years of fossil fuels. Specifically coal lasts about 110 years, oil lasts about 53 years, and natural gas lasts about 54 years. Also, fossil fuel use is the primary sources of CO_2, leading to global warming. In particular, Japan is a country of fossil import dependence. Besides, human activities contribute to the global warming by adding excessive amounts of greenhouse gases to the atmosphere. Today, Japan uses renewable energy for only 1.3% of the total energy usage. While current renewable energy usage remains low, Japan is planning to accelerate further renewable energy development. Among them, solar energy is considered as one of the most promising energy alternatives.

In order to build a low-carbon society, huge amount of solar photovoltaic (PV) power generation systems have been installed in recent years. According to International Energy Agency (IEA) Photovoltaic Power Systems (PVPS) report 2015, at least 38.7 GW of solar PV systems have been installed and connected to the electric power grids in the world in 2014. Japan was the second market for PV in 2014 with an estimated 9.7 GW of PV installations. The boom in solar PV power generation system got started since the introduction in Japan of a new feed-in tariff (FIT) scheme for renewable energy in July 2012 (METI, 2015). Under this FIT scheme, regional utilities have to purchase power from solar and other renewable energy producers for non-household use at preset prices for a period of 20 years. By the end of 2014, cumulative capacity reached 23.3 GW, becoming the world's third largest power producer from solar PV with the help of the

Japanese government subsidy and the FIT scheme (IEA PVPS, 2015). Moreover, to promote photovoltaic (PV) in households, the Japanese government offers subsidies for installation costs.

Large-scale solar PV power generation systems have been installed and connected to the electric power grids, and the prediction of their power generations or the forecasting of the solar irradiance are required to manage the electric grids for the stable energy supply. However, the solar power production is dominantly affected by the weather conditions. Besides, the fluctuation of solar PV power generation due to weather is an uncertain factor for the power grid's management. The evaluation or forecasting of the solar irradiance is the first and the most essential step to estimate the PV generation and its fluctuation. But the forecasting error will have a relatively large influence in the projection of PV generation amount (Lorenz *et al*. 2009). Not only the solar irradiance forecasting but also its forecasting reliability should be urgently required for the management of the power grid containing large amount of PV systems.

In this work, first of all is to employ a meteorological model for the solar irradiance forecasting. Next is to improve the accuracy by applying a post-processing approach of the meteorological computation. The reliable forecasting information will help the grid operators for better management of the electrical power balance between demand and generation (Heinemann *et al*. 2006; Hashimoto and Kobayashi 2011; Lorenz *et al*. 2009; Diagne *et al*. 2013). Therefore, the author applies an ensemble method (Palmer *et al*. 2000; Richardson *et al*. 2000; Furukawa and Sakai 2004), and also evaluates the prediction interval of the solar irradiance forecasting as the forecasted reliability. Furthermore, the effect of the improvement to the forecasting of the prediction interval with the post-processing approach is also discussed in this work.

1.2 Outline of this thesis

This thesis presents the results gained from investigations of probabilistic forecasting of solar irradiance using the Weather Research and Forecasting (WRF) model. Following Chapter 1 which describes the background and the objective of this study, Chapter 2 states the on-situ observations used for the validation of the accuracy of solar irradiance forecasting, and the evaluation of solar irradiance forecasting reliability. Chapter 3 states governing equations and physical options of the WRF model. Also, a WRF simulation is performed, and the accuracy of the simulated solar irradiance (Global Horizontal Irradiance, GHI) is examined using the on-situ observations illustrated in the chapter 2. Chapter 4 presents an attempt at increasing the accuracy of the WRF-simulated solar GHI with the use of Kalman Filter as a post-processing method. In order to evaluate the prediction interval of solar irradiance forecasting, ensemble forecasting is employed in Chapter 5 and solar irradiance GHI ensemble forecasting with Kalman Filter is also discussed in Chapter 6. Finally, the conclusions of the whole study and some suggestions for future studies are given in Chapter 7.

Chapter 2　On-site observations

2.1 Pyranometer

The observed solar irradiance (Global Horizontal Irradiance, GHI) data used in the work are measured by the Chubu Electric Power Co. Inc. under PV300 project, supported by the Ministry of Economy, Trade and Industry of Japan. Solar irradiance GHI, which refers to hemispherical solar irradiance received on a horizontal plane surface, is measured by using the EKO Pyranometer MS-402 (EKO instruments manual).

The MS-402 conforms to the First Class specifications defined by ISO9060 and its robust brass mechanical construction makes it a durable sensor suitable to be used in harsh environments for routine global irradiance measurements. The MS-402 can be applied as multipurpose high quality monitoring sensor in the PV and Meteorological market.

Specifications of EKO Pyranometer MS-402 are listed in **Table 2.1**. The appearance and outline drawing of MS-402 Pyranometer are shown in **Fig. 2.1** and **Fig. 2.2**, respectively. Glass domes are used to reject infrared radiation of wavelength above 3μm for thermopile-type sensors. Key features of MS-402 are: response time (95% signal level in < 8s); temperature compensated over a wide temperature range.

Fig. 2.1 Appearance of MS-402 Pyranometer

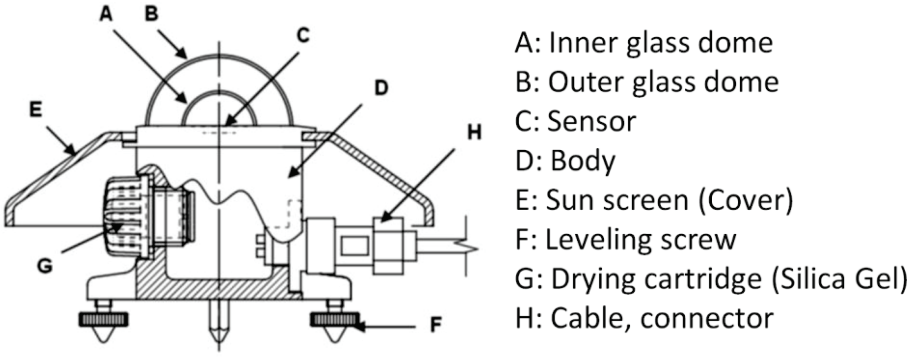

Fig. 2.2 Outline drawing of MS-402 Pyranometer

Table 2.1 Specifications of EKO Pyranometer MS-402

Characteristics	MS-402
ISO9060 classification	First Class
Response time 95% (sec)	Approx. 8
Zero offset－Thermal radiation (200W/m^2)	< 6W/m^2
Zero offset－Temperature change (5K/hr)	< 2W/m^2
Non-stability (change/year)	< 0.5%
Non-linearity (at 1000W/m^2)	< 0.2%
Directional response (at 1000W/m^2)	< 20W/m^2
Spectral selectivity (0.35－1.5μm)	< 1%
Temp. response (for 50°C band)	< 1%
Tilt response (at 1000W/m^2)	< 0.2%
Sensitivity (μV/W・m^{-2})	Approx. 7
Impedance (Ω)	Approx. 500
Operating temperature range (°C)	-40 to +80
Cable length	10m
Wavelength range	285 to 3000nm

※ISO9060: an ISO norm (International Standard), defines the pyranometer and pyrheliometer characteristics, their requirements and corresponding categories.

2.2 Target area

The target area for the solar irradiance forecasting in this work is the central region of Japan; that is, Nagano, Gifu, Aichi, Mie and Shizuoka prefectures. There are 61 observation sites for the solar irradiance in the area. **Figure 2.3** shows an overview on the locations of the sites. Detailed information of the sites on coordinates is provided in **Table 2.2**.

Table 2.2 Locations of observation sites

No.	Site	Longitude	Latitude
1	Daiti001	136.95˚E	35.06˚N
2	Daiti002	136.94˚E	35.08˚N
3	Daiti003	136.93˚E	35.07˚N
4	Daiti004	136.99˚E	35.04˚N
5	Daiti005	136.90˚E	35.05˚N
6	Daiti006	136.90˚E	35.09˚N
7	Daiti007	136.88˚E	35.07˚N
8	Daiti008	136.99˚E	35.13˚N
9	Daiti009	136.91˚E	35.13˚N
10	Daiti010	137.01˚E	34.99˚N
11	Daiti011	136.84˚E	35.11˚N
12	Daiti012	136.92˚E	35.16˚N
13	Daiti013	136.86˚E	35.17˚N
14	Daiti014	137.08˚E	35.13˚N
15	Daiti015	136.93˚E	35.20˚N
16	Daiti016	137.01˚E	35.20˚N
17	Daiti017	136.78˚E	35.12˚N
18	Daiti018	136.94˚E	34.89˚N
19	Daiti019	137.15˚E	35.12˚N
20	Daiti020	136.97˚E	35.25˚N
21	Dmie021	136.67˚E	35.06˚N
22	Daiti022	136.94˚E	35.32˚N
23	Daiti023	136.81˚E	35.31˚N

24	Daiti024	137.37˚E	34.83˚N
25	Daiti025	137.28˚E	34.67˚N
26	Dsizu026	137.51˚E	34.71˚N
27	Dsizu027	137.72˚E	34.70˚N
28	Dsizu028	137.86˚E	34.71˚N
29	Dsizu029	138.01˚E	34.77˚N
30	Dsizu030	138.17˚E	34.83˚N
31	Dsizu031	138.41˚E	34.98˚N
32	Daiti032	137.16˚E	34.94˚N
33	Dnaga033	138.36˚E	36.84˚N
34	Dnaga034	137.91˚E	36.30˚N
35	Dnaga035	137.98˚E	36.23˚N
36	Dnaga036	138.30˚E	36.37˚N
37	Dnaga037	138.46˚E	36.23˚N
38	Dnaga038	138.22˚E	36.67˚N
39	Dnaga039	138.15˚E	36.58˚N
40	Dnaga040	137.96˚E	36.11˚N
41	Dnaga041	138.08˚E	36.07˚N
42	Dnaga042	137.83˚E	35.52˚N
43	Dnaga043	137.97˚E	35.84˚N
44	Dgifu044	136.76˚E	35.42˚N
45	Dgifu045	136.93˚E	35.49˚N
46	Dgifu046	137.13˚E	35.34˚N
47	Dgifu047	136.62˚E	35.36˚N
48	Dmie048	136.53˚E	34.87˚N
49	Dmie049	136.13˚E	34.75˚N
50	Dgifu050	137.03˚E	35.44˚N
51	Dgifu051	136.74˚E	35.39˚N
52	Dgifu052	137.50˚E	35.50˚N
53	Dgifu053	137.26˚E	36.15˚N
54	Dmie054	136.40˚E	34.22˚N
55	Dmie055	136.71˚E	34.49˚N
56	Dmie056	136.63˚E	34.97˚N
57	Dmie057	136.20˚E	34.07˚N
58	Dgifu058	137.21˚E	35.87˚N
59	Dgifu059	136.85˚E	35.40˚N
60	Dmie060	136.51˚E	34.71˚N
61	Dmie061	136.54˚E	34.58˚N

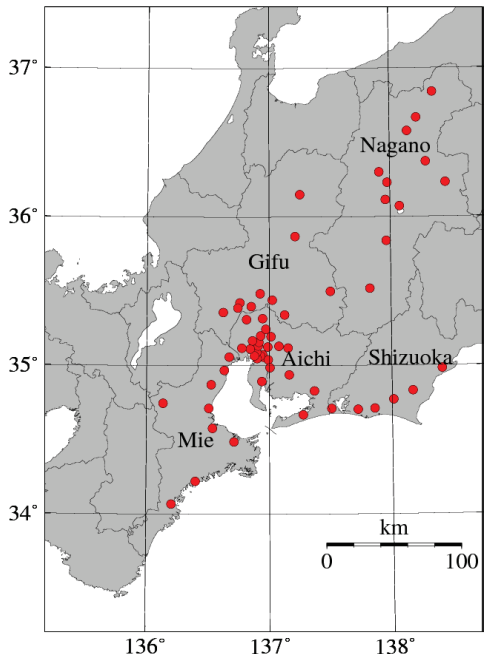

Fig. 2.3 Target area of the solar irradiance forecasting and observation sites (red dots). This area is corresponding to the Domain D03 in Fig. 3.3 and Table 3.6.

2.3 Observation data

Each site observes the solar irradiance on the horizontal ground plane (Global Horizontal Irradiance, GHI) with 10-second interval. The observation data with high time resolution contain short-term fluctuations, but the averaged irradiance is more important for the applications (Lorenz *et al*. 2009). The observation data are, therefore, smoothed within 30-minute interval and then averaged with all sites, because all sites are in the area of one commercial electric power grid.

Figure 2.4 depicts the time series of observed irradiance (GHI) from 10-second interval, 30-minutely average at single site (136.95˚E, 35.06˚N) and 30-minutely average at 61 observation-point average during the daytime on July 1st, 2013. The fluctuation of the solar irradiance in the single site is reduced and the trend of the time

variation of the irradiance is emphasized by calculating mean value in time and space as found in this figure. The observed data are used for the verification of the solar irradiance forecasting and also for the evaluation of its prediction interval.

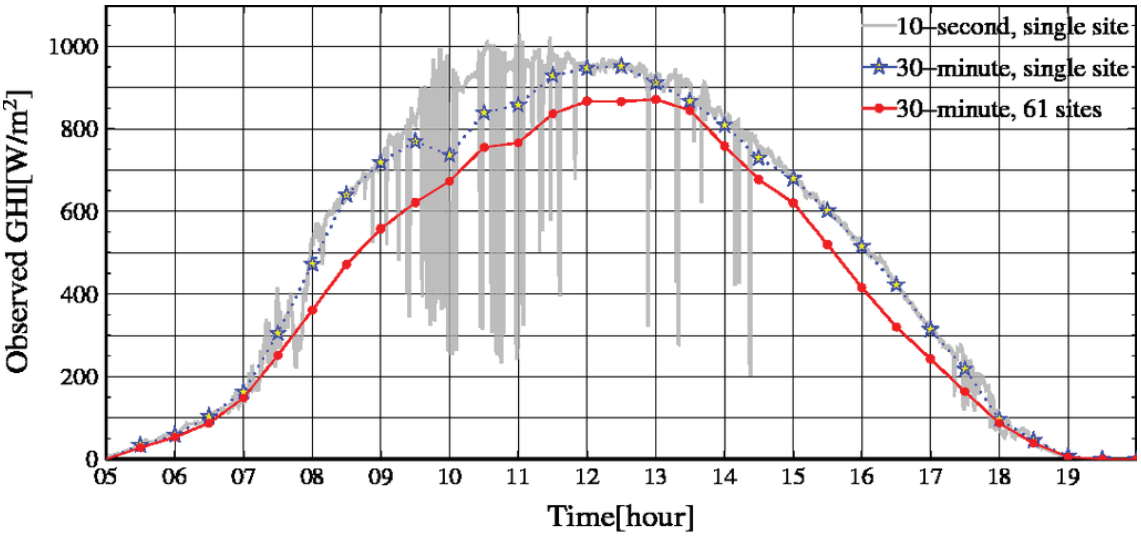

Fig. 2.4 Time series of observed solar irradiance (GHI) in 10-second interval, 30-minutely average at single site (136.95˚E, 35.06˚N) and 30-minutely average at 61 observation-point average (from 05:00:00 to 20:00:00 LST, July 1st, 2013)

Chapter 3 Solar irradiance forecasting by applying a mesoscale meteorological model

3.1 Introduction

The attempts on solar irradiance forecasting have been started more than thirty years ago (Jensenius and Cotton 1981). Up to the present, different approaches to forecast the solar irradiance in different time horizons have been proposed. Hammer *et al*. (2003) analyzes satellite images for the irradiance forecasting. Reikard (2009) applies statistical models and forecasts the irradiance by analyzing data of the past. Lorenz *et al*. (2009), Hashimoto *et al*. (2011) and Shimada *et al*. (2012) represent the physical atmospheric conditions by applying numerical weather prediction (NWP) models, and forecast the solar irradiance. Perez *et al*. (2010) compares the solar irradiance forecasts with some approaches, and shows that the satellite image approach is better than others until 5 hour ahead forecasting; but after that, the NWP forecasting becomes better. The forecasting period of this work is of several days ahead, therefore, a NWP model for the solar irradiance forecasting is employed.

3.2 Methodology

3.2.1 Meteorological model WRF

This thesis employed the Advanced Research Weather Research and Forecasting (WRF) model (ARW; Skamarock *et al*. 2008) for forecasting weather and the solar irradiance in the several days ahead. This model is a fully compressible, non-hydrostatic mesoscale model developed by National Centers for Atmospheric Research (NCAR) and National Centers for Environmental Prediction (NCEP). This model is designed to be a flexible, state-of-the-art atmospheric simulation system that is

portable and efficient on available parallel computing platforms. This model is commonly used worldwide these days in the meteorological field. For the estimation of the renewable energy resources, this model is also used extensively, because it can simulate the realistic weather with high resolution. For example, Heinemann *et al*. (2006) investigates the resources of the solar energy in recent years based on daily weather forecasting with this model.

3.2.2 Governing equations of WRF

The WRF dynamics solver integrates the compressible, non-hydrostatic Euler equations casted in a flux (conservative) form where the vertical coordinate, denoted as η, is defined by a normalized hydrostatic pressure (or mass) (Laprise 1992).

$$\eta = \frac{(p_h - p_{ht})}{\mu} \qquad \text{where } \mu = p_{hs} - p_{ht} \tag{3.1}$$

Where p_h is the hydrostatic component of the pressure, and p_{hs} and p_{ht} are the values for the dry atmosphere at the surface and top boundaries, respectively. Following common practice, here sets p_{ht} = constant. η decreases monotonically from a value of 1 at the surface to 0 at the upper boundary of the model domain. This coordinate definition proposed by Laprise, and depicted in **Fig. 3.1**.

The grid staggering of the WRF model is the Arakawa-C grid. As shown in **Fig. 3.2**, the u and v components of horizontal velocity are normal to the respective faces of the grid cell, and the mass/thermodynamic/scalar/chemistry variables are located in the center of the cell. The solid lines denote coarse grid cell boundaries, and the dashed lines are the boundaries for each fine grid cell. The horizontal components of velocity (u

and v) are defined along the normal cell face, and the thermodynamic variables (θ) are defined at the center of the grid cell (each square). The bold typeface variables along the interface between the coarse and the fine grid define the locations where the specified lateral boundaries for the nest are in effect.

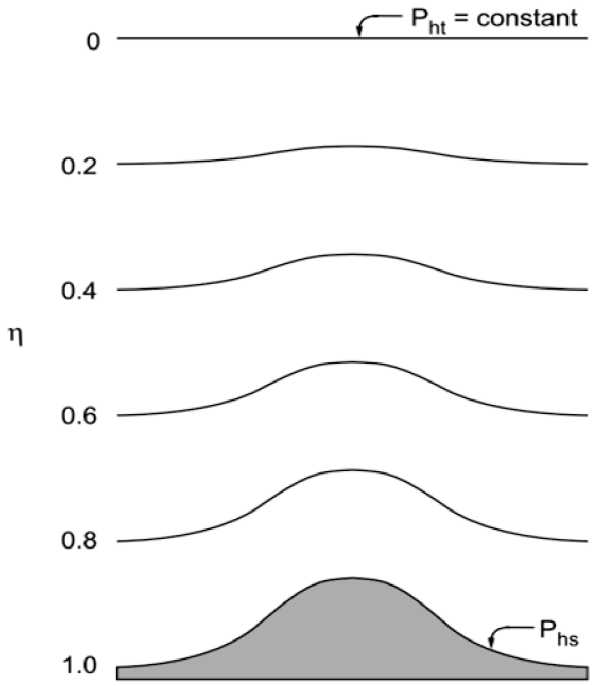

Fig. 3.1 Schematic of the terrain following η coordinate of WRF

(Skamarock et al. 2008)

Using the terrain following η vertical coordinate, the flux-form moist Euler equations are expressed as:

$$\frac{\partial U}{\partial t} + (\nabla \cdot \vec{V} u) + P_x(p,\phi) = F_U \tag{3.2}$$

$$\frac{\partial V}{\partial t} + (\nabla \cdot \vec{V} v) + P_y(p,\phi) = F_V \tag{3.3}$$

$$\frac{\partial W}{\partial t} + (\nabla \cdot \vec{V} w) + P_\eta(p, \phi) = F_W \tag{3.4}$$

$$\frac{\partial \Theta}{\partial t} + (\nabla \cdot \vec{V} \theta) = F_\Theta \tag{3.5}$$

$$\frac{\partial \mu}{\partial t} + (\nabla \cdot \vec{V}) = 0 \tag{3.6}$$

$$\frac{\partial \phi}{\partial t} + \frac{1}{\mu}\left[(\vec{V} \cdot \nabla \phi) - gW \right] = 0 \tag{3.7}$$

$$\frac{\partial Q_m}{\partial t} + (\nabla \cdot \vec{V} Q_m) = F_{Q_m} \tag{3.8}$$

Where $\mu(x, y)$ represents the mass of the dry air per unit area with the column in the model domain at (x, y), hence the flux form variables are defined as

$$\vec{V} = \frac{\mu}{m}\vec{v} = (U, V, W), \quad U = \frac{\mu u}{m}, \quad V = \frac{\mu v}{m}, \quad W = \frac{\mu w}{m}, \quad \Omega = \frac{\mu \dot{\eta}}{m}, \quad \Theta = \frac{\mu \theta}{m} \tag{3.9}$$

Where m is a map-scale factor that allows mapping of the equations to the sphere (Haltiner and Williams, 1980) and is given as

$$m = \frac{(\Delta x, \Delta y)}{\text{distance on the earth}} \tag{3.10}$$

The velocities $\vec{v} = (u, v, w)$ are the physical velocities in the two horizontal and vertical directions, respectively, $w = \dot{\eta}$ is the transformed 'vertical' velocity, and θ is the potential temperature. $Q_m = \mu q_m$; $q_m = q_v, q_c, q_i, \cdots,$ represent the mass of water

vapor, cloud, rain, ice, etc, and q_* are their mixing ratios (mass per mass of dry air). Here also defines non-conserved variables $\phi = gz$ (the geopotential), p (pressure), and $\alpha = 1/\rho$ (the specific volume) that appear in the governing equations. α_d refers to the specific volume of the dry air, and α is the specific volume including all moist species, i.e. $\alpha = \alpha_d (1 + q_v + q_c + q_i \cdots)^{-1}$, as described in Skamarock *et al*. (2008).

To close the system, we use the diagnostic relation for the specific volume (that is, the hydrostatic relation for dry air)

$$\phi_\eta = -\alpha_d \mu \tag{3.11}$$

and the moist equation of state

$$p = p_0 \left(\frac{R_d \theta_m}{p_0 \alpha_d} \right)^\gamma \quad \text{where} \quad \theta_m = \theta \left(1 + \frac{R_v}{R_d} q_v \right) \approx \theta (1 + 1.61 q_v) \tag{3.12}$$

where $\gamma = c_p / c_v = 1.4$ is the ratio of the heat capacities for dry air, R_d is the gas constant for dry air, and p_0 is a reference pressure (typically 10^5 Pa). And

$$\nabla \cdot \vec{V} a = m^2 \left[\frac{\partial}{\partial x} (Ua) + \frac{\partial}{\partial y} (Va) \right] + \frac{\partial}{\partial \eta} (\Omega a) \tag{3.13}$$

$$\vec{V} \cdot \nabla a = m^2 \left[U \frac{\partial a}{\partial x} + V \frac{\partial a}{\partial y} \right] + m \Omega \frac{\partial a}{\partial \eta} \tag{3.14}$$

Where a represents a generic scalar variable. The pressure gradient terms in Eqs. (3.2) to (3.4) are given by

$$\frac{\partial P(p,\phi)}{\partial x} = \frac{\alpha}{\alpha_d}\left(-\frac{\partial(p\phi_\eta)}{\partial x} + \frac{\partial(p\phi_x)}{\partial \eta}\right) \tag{3.15}$$

$$\frac{\partial P(p,\phi)}{\partial y} = \frac{\alpha}{\alpha_d}\left(-\frac{\partial(p\phi_\eta)}{\partial y} + \frac{\partial(p\phi_y)}{\partial \eta}\right) \tag{3.16}$$

$$\frac{\partial P(p,\mu)}{\partial \eta} = -\frac{g}{m}\left(\frac{\alpha}{\alpha_d} p_\eta - \mu\right) \tag{3.17}$$

The right-hand-side terms F_U, F_V, F_W, F_Θ, and F_{Q_m} represent forcing terms arising from model physics, turbulent mixing, spherical projections, the earth's rotation, and moist physics, and are described in detail in NCAR's WRF tutorial manual (Skamarock *et al*. 2008).

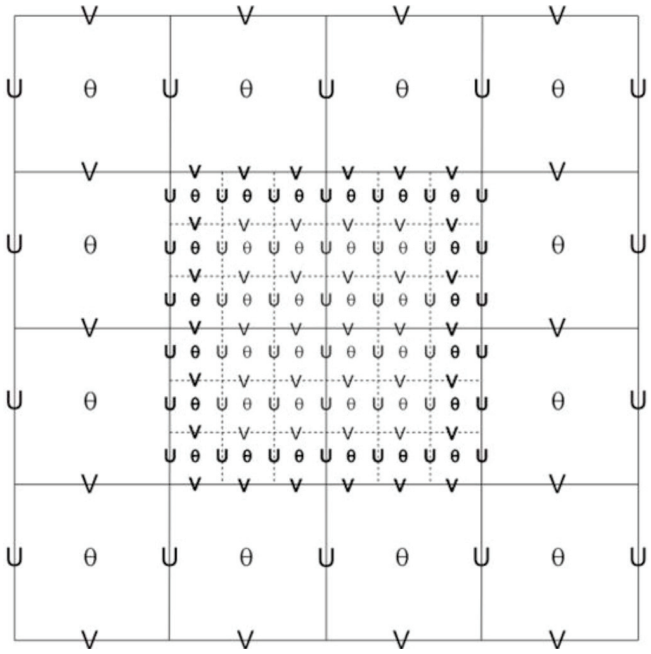

Fig. 3.2 Arakawa-C grid staggering for a portion of a parent domain and an imbedded nest domain with a 3:1 grid size ratio (Skamarock et al. 2008)

3.2.3 Physics options of WRF

The WRF physical options fall into several categories, each containing several choices. The physics categories are (1) microphysics, (2) cumulus parameterization, (3) planetary boundary layer (PBL), (4) land-surface model and (5) atmospheric radiation.

(1) Microphysics

Microphysics includes explicitly resolved water vapor, cloud and precipitation processes. In the version 3 of the Advanced Research WRF (ARW), microphysics is carried out at the end of the time-step as an adjustment process, and so does not provide tendencies. **Table 3.1** shows a summary of the microphysics options, and for each scheme, the number of moisture variables, and whether ice-phase and mixed-phase processes are listed (Skamarock *et al*. 2008). Mixed-phase processes are those that result from the interaction of ice and water particles such as riming that produces graupel or hail. As a general rule, for grid sizes less than 10 km, where updrafts may be resolved, mixed-phase schemes should be used, particularly in convective or icing situations. For coarser grids the added expense of these schemes is not worth it because riming is not likely to be well resolved.

The Kessler scheme (Klessler 1969) is a simple warm cloud scheme that includes water vapor, cloud water and rain. In Purdue Lin scheme (Chen and Sun 2002), six classes of hydrometeors are included: water vapor, cloud water, rain, cloud ice, snow and graupel. This is a relatively sophisticated microphysics scheme in WRF, and it is most suitable for use in research studies. The WRF single-moment 3-class (WSM3) scheme (Hong *et al*. 2004) predicts three categories of hydrometers: vapor, cloud water/ice, and rain/snow, which is a so-called simple-ice scheme. This scheme is computationally

efficient for the inclusion of ice processes, but lacks super-cooled water and gradual melting rates. The WSM5 scheme is similar to the WSM3 simple ice scheme. However, vapor, rain, snow, cloud ice, and cloud water are held in five different arrays. The details can be found in Hong *et al*. (2004) and Hong and Lim (2006). This scheme is efficient in intermediate grids between the mesoscale and cloud resolving grids. The WSM6 scheme extends the WSM5 scheme to include graupel and its associated processes. A more detailed description of the WSM6 scheme including the production terms and the computational procedure is given in Hong and Lim (2006). A new method for representing mixing-phase particle fall speeds for the snow and graupel particles by assigning a single fall speed to both sedimentation and accretion processes is introduced (Dudhia *et al*. 2008). The Eta grid-scale cloud and precipitation (GCP) scheme predicts changes in water vapor and condensate in the forms of cloud water, rain, cloud ice, and precipitation ice (snow/graupel/sleet).

Table 3.1 Microphysics options

Scheme	Number of variables	Ice-phase processes	Mixed-phase processes
Kessler	3	N	N
Purdue Lin	6	Y	Y
WSM3	3	Y	N
WSM5	5	Y	N
WSM6	6	Y	Y
Eta GCP	2	Y	Y
Thompson	7	Y	Y
Goddard	6	Y	Y
Morrison 2-Moment	10	Y	Y

Data source: Skamarock *et al*. 2008.

A new bulk microphysical parameterization (BMP), Thompson *et al*. scheme (Thompson *et al*. 2004), has been developed for the use with WRF. The Goddard cumulus ensemble models (Tao and Simpson 1993) one-moment bulk microphysical schemes are mainly based on Lin *et al*. (1983) with additional processes from Rutledge and Hobbs (1984). The Morrison *et al*. (2009) scheme is based on the two-moment bulk microphysics scheme of Morrison *et al*. (2005) and Morrison and Pinto (2006). The scheme has been extensively tested and compared with both idealized and real case studies covering a wide range of conditions.

In this study, the WSM6 graupel scheme is used. Of the three WSM schemes, the WSM6 scheme is the most suitable for cloud-resolving grids, considering the efficiency and theoretical backgrounds.

(2) Cumulus parameterizations

Cumulus parameterizations are theoretically only valid for coarser grid sizes, e.g., greater than 10 km, where they are necessary to properly release latent heat on a realistic time scale in the convective columns. While the assumptions about the convective eddies being entirely sub-grid-scale break down for finer grid sizes, sometimes these schemes have been found to be useful in triggering convection in 5~10 km grid applications. Generally, they should not be used when the model can resolve the convective eddies itself (e.g., less than 5 km). **Table 3.2** summarizes the basic characteristics of the available cumulus parameterization options in the WRF.

The modified version of the Kain-Fritsch scheme (Kain 2004) utilizes a simple cloud model with moist updrafts and downdrafts, including the effects of detrainment, entrainment, and relatively simple microphysics. The Betts-Miller-Janjic (BMJ) scheme

(Janjic 1994; Janjic 2000) has been optimized over years of operational application at NCEP. Recently, attempts have been made to refine the scheme for higher horizontal resolutions, primarily through modifications of the triggering mechanism. Grell and Devenyi (2002) introduced an ensemble cumulus scheme in which effectively multiple cumulus schemes and variants are run within each grid box and then the results are averaged to give the feedback to the model. The Grell-3 scheme was first introduced in version 3.0, so is new and not yet well tested in many situations.

In this study, the Betts-Miller-Janjic cumulus parameterization is used, because it has been refined for higher horizontal resolutions and has been optimized on the operational application.

Table 3.2 Cumulus parameterization options

Scheme	Cloud detrainment	Type of scheme	Closure
Kain-Fritsch	Y	Mass flux	CAPE removal
Betts-Miller-Janjic	N	Adjustment	Sounding adjustment
Grell-Devenyi	Y	Mass flux	Various
Grell-3	Y	Mass flux	Various

※CAPE: convective available potential energy.

Data source: Skamarock *et al*. 2008.

(3) Planetary boundary layer

The planetary boundary layer (PBL) is responsible for vertical sub-grid-scale fluxes due to eddy transports in the whole atmospheric column, not just the boundary layer. The PBL schemes determine the flux profiles within the well-mixed boundary layer and the stable layer, and thus provide atmospheric tendencies of temperature, moisture (including clouds), and horizontal momentum in the entire atmospheric column. **Table**

3.3 summarizes the basic features of the PBL schemes in WRF.

In this study, the Mellor-Yamada-Janjic PBL scheme is used. This parameterization of turbulence in the PBL represents a nonsingular implementation of the Mellor-Yamada level 2.5 turbulence closure model (Mellor and Yamada 1982) through the full range of atmospheric turbulence regimes.

Table 3.3 Planetary boundary layer options

Scheme	Unstable PBL mixing	Entrainment treatment	PBL top
Medium Range Forecast Model (MRF)	K profile + countergradient term	part of PBL mixing	from critical bulk R_i
Yonsei University (YSU)	K profile + countergradient term	explicit term	from buoyancy profile
Mellor-Yamada-Janjic (MYJ)	K from prognostic TKE	part of PBL mixing	from TKE
Asymmetrical Convective Model version 2 (ACM2)	Transilient mixing up, local K down	part of PBL mixing	from critical bulk R_i

※TKE: turbulent kinetic energy.

Data source: Skamarock *et al*. 2008.

(4) Land-surface model

The land-surface models (LSMs) use atmospheric information from the surface layer scheme, radiative forcing from the radiation scheme, and precipitation forcing from the microphysics and convective schemes, together with internal information on the land's state variables and land-surface properties, to provide heat and moisture

fluxes over land points and sea-ice points. The LSM provides no tendencies, but does update the land's state variables which include the ground (skin) temperature, soil temperature profile, soil moisture profile, snow cover, and possibly canopy properties. **Table 3.4** summarizes the basic features of the land-surface treatments in WRF.

In this study, the Noah LSM (Chen and Duddhia 2001) is used. The scheme has the benefit of being consistent with the time-dependent soil fields provided in the analysis datasets. This provides sensible and latent heat fluxes to the boundary-layer scheme.

Table 3.4 Land surface options

Scheme	Vegetation processes	Soil variables (layers)	Snow scheme
5-layer	N	Temperature (5)	none
Noah	Y	Temperature, Water+Ice, Water (4)	1-layer fractional
Rapid update cycle (RUC)	Y	Temperature, Ice, Water+Ice (6)	Multi-layer
Pleim-Xiu	Y	Temperature, Moisture (2)	Input only

Data source: Skamarock *et al*. 2008.

(5) Atmospheric radiation

The radiation schemes provide atmospheric heating due to radiative flux divergence and surface downward long wave and short wave radiation for the ground heat budget. Within the atmosphere, the radiation responds to model-predicted cloud and water vapor distributions, as well as specified carbon dioxide, ozone, and (optionally) traces gas concentrations. All the radiation schemes in WRF currently are column (one-dimensional) schemes, so each column is treated independently, and the

fluxes correspond to those in infinite horizontally uniform planes, which is a good approximation if the vertical thickness of the model layers is much less than the horizontal grid length. This assumption would become less accurate at high horizontal resolution. **Table 3.5** summarizes the basic features of the radiation schemes in the WRF.

Long wave radiation includes infrared or thermal radiation absorbed and emitted by gases and surfaces. Upward long wave radiative flux from the ground is determined by the surface emissivity that in turn depends upon land-use type, as well as the ground (skin) temperature. The rapid radiative transfer model (RRTM) long wave scheme is based on Mlawer *et al*. (1997) and is a spectral-band scheme using the correlated-k method. Eta geophysical fluid dynamics laboratory (GFDL) long wave radiation scheme follows the simplified exchange method of Fels and Schwarzkopf (1975) and Schwarzkopf and Fels (1991), with calculation over spectral bands associated with carbon dioxide, water vapor, and ozone. The community atmosphere model version 3.0 (CAM3) is for climate simulations. It is documented fully by Collins *et al*. (2004).

In this study, the RRTM long wave radiation scheme is used. It uses pre-set tables to accurately represent long wave processes due to water vapor, ozone and CO_2, as well as accounting for cloud optical depth.

Short wave radiation includes visible and surrounding wavelengths that make up the solar spectrum. Hence, the only source is the sun, but processes include absorption, reflection, and scattering in the atmosphere and at surfaces. For short wave radiation, the upward flux is the reflection due to surface albedo. Short wave calculations are made using a daylight-mean cosine solar zenith angle over the time interval in the Eta GFDL short wave radiation scheme (Lacis and Hansen 1974). The Dudhia short wave

radiation scheme is based on Dudhia (1989) and is taken from MM5. As described in Chou and Suarez (1994), the Goddard short wave radiation scheme has a total of 11 spectral bands and considers diffuse and direct solar radiation components in a two-stream approach that accounts for scattered and reflected components. The CAM3 short wave radiation scheme is especially suited for regional climate simulations by having an ozone distribution that varies during the simulation according to monthly zonal-mean climatological data.

In this study, the Dudhia short wave radiation scheme is used, because it is a simple downward integration of solar flux, accounting for clear-air scattering, water vapor absorption, and cloud albedo and absorption. In the version 3, the scheme has an option to account for terrain slope and shadowing effects on the surface solar flux.

Table 3.5 Radiation options

Scheme	Long wave/Short wave	Spectral bands	CO_2, O_3, clouds
RRTM LW	LW	16	CO_2, O_3, clouds
GFDL LW	LW	14	CO_2, O_3, clouds
CAM3 LW	LW	2	CO_2, O_3, clouds
GFDL SW	SW	12	CO_2, O_3, clouds
Dudhia SW	SW	1	clouds
Goddard SW	SW	11	CO_2, O_3, clouds
CAM3 SW	SW	19	CO_2, O_3, clouds

Data source: Skamarock *et al*. 2008.

3.2.4 Computational conditions of WRF

The computational domains with WRF are set as shown in **Fig. 3.3**. The resolutions of domains D01, D02 and D03 are 18 km, 6 km and 2 km, respectively, and they are nested in two-way. The all 61 observation sites are in the domain D03.

The computational settings of weather forecasting with WRF are summarized in **Table 3.6**. The Japan Meteorological Agency (JMA) Global Analysis data for the Global Spectral Model for Japan Area (GSM-JP, Japan Meteorological Business Support Center, 2015) (0.2°×0.25°and 3-hour time interval, 72-hour ahead), the analysis data of Global Forecast System (GFS) (0.5°× 0.5°and 3-hour time interval, 72-hour ahead) from the National Centers for Environmental Prediction (NCEP, 2015), and the Operational Sea Surface Temperature and Sea Ice Analysis (OSTIA) (0.05°× 0.05° and daily) at National Centre for Ocean Forecasting (2015) are used as the initial and the boundary conditions for the model simulation. Specifications of three kinds of objective analysis data used for the input data are described in **Table 3.7**.

The target period of this analysis is from July 2013 to June 2014.

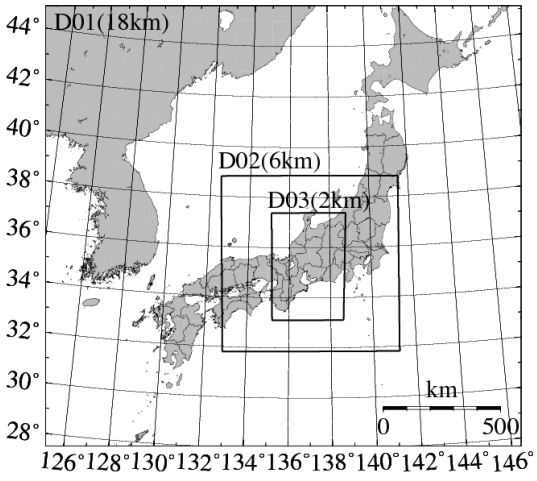

Fig. 3.3 Computational domains of the meteorological model WRF

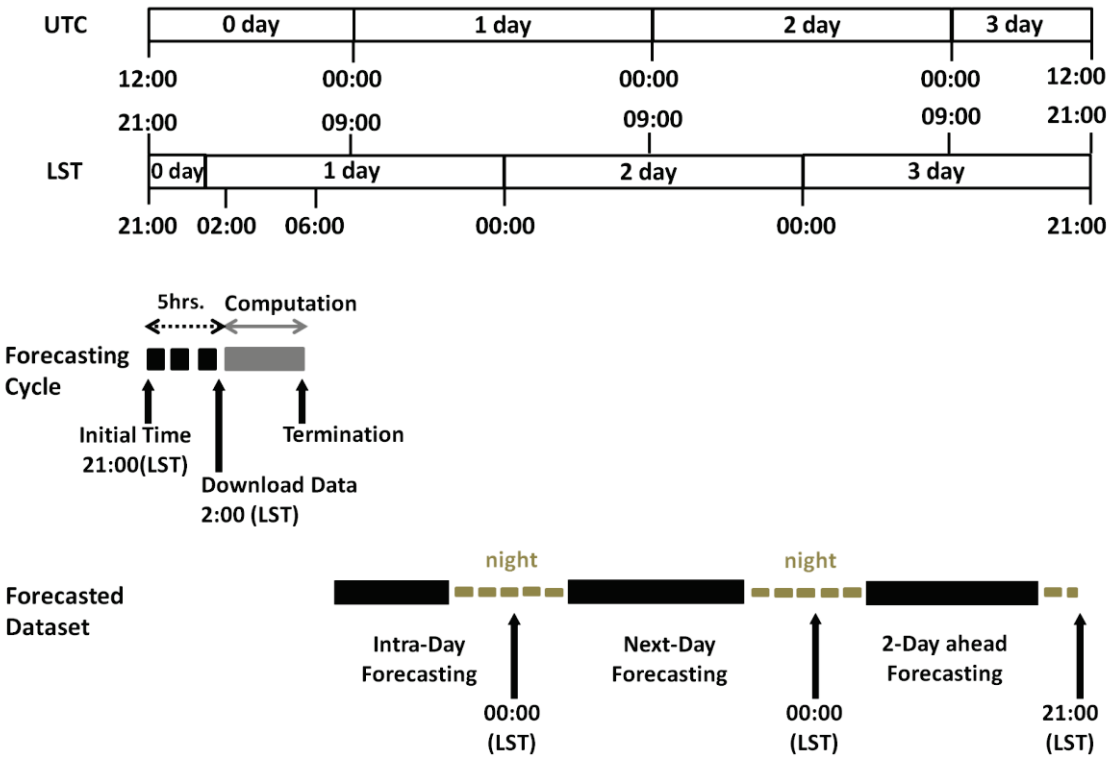

Fig. 3.4 Solar irradiance forecasting cycle using WRF

Fig. 3.5 Appearance of parallelized computer used for the WRF simulation

Table 3.6 Computational condition for the weather and the solar irradiance forecasting with WRF

Period	Start: 12:00 UTC (21:00 LST) 72-hour forecasting in Computation
Input data	JMA GSM-JP (3-hourly, 0.2°×0.25°) NCEP GFS (3-hourly, 0.5°×0.5°) OSTIA (daily, 0.05°×0.05°)
Nesting	2-way nesting
Domain	Domain 01, D01 (18 km, 120×110 grids) Domain 02, D02 (6 km, 130×130 grids) Domain 03, D03 (2 km, 160×229 grids)
Vertical layer	50 levels (surface to 100 hPa)
Physical options	Dudhia short wave radiation scheme RRTM long wave radiation scheme WSM 6-class graupel scheme Betts-Miller-Janjic cumulus parameterization (Domain 01 and Domain 02 only) Noah land surface model Mellor-Yamada-Janjic PBL parameterization
FDDA option	Disable

Table 3.7 Description of input data used in the WRF model

Name	Developed organization	Usage	Grid spatial resolution	Vertical levels
GSM-JP	JMA	Initial and boundary data of weather elements	～20×25 km	60-level (surface to 0.1 hPa)
GFS	NCEP	Initial and boundary data of land surface model (LSM)	～50×50 km	26-level (surface to 10 hPa)
OSTIA	Met Office	Sea surface temperature (SST)	～5×5 km	-

3.2.5 Solar irradiance forecasting system

Figure 3.4 shows the solar irradiance forecasting cycle using WRF. The computation of forecasting is performed once a day. The initial valid time of the forecasting is 21:00 LST (Local Standard Time). The time difference of the LST in Japan is 9 hours from Universal Coordinated Time (UTC), and the initial time is therefore 12:00 UTC. This cycle gets the meteorological data from the meteorological agencies, and starts computation by using them as the initial and boundary conditions of the forecasting. The horizon time of the computation is 72 hours, and the forecasting contains the solar irradiance in three daytimes. The data computed in the meteorological agencies are downloaded, and the weather and the solar irradiance are computed with WRF. The WRF computation is terminated at the next morning of the initial valid time of the forecasted data in the Local Standard Time. Therefore, a termination day of forecasting computation is called as an operation day. The forecasted results are divided in the time horizon into three days: intra-day, next-day and 2-day ahead forecasting. They are analyzed separately in the following sections. **Figure 3.5** shows the appearance of parallelized computer used for the WRF simulation.

3.3 Results and discussion

The forecasted solar irradiance computed with WRF is compared with the observed data, and the verification of the forecasting is discussed in this section. As explained before, the global horizontal irradiance (GHI) averaged in 61 sites in **Fig. 2.3** and with 30-minute interval is used for the verification. The data in night time are rejected for the verification.

The statistical indices used to evaluate the forecasting accuracy are mean bias

(Bias), relative mean bias (rBias), root mean square error (RMSE), relative root mean square error (rRMSE) and correlation coefficient (CORR). They are defined as follows:

$$Bias = \frac{1}{N}\sum_{i=1}^{N}(GHI_{forecasted,i} - GHI_{observed,i}) \tag{3.18}$$

$$rBias = \frac{Bias}{\overline{GHI}_{observed}} = \frac{\frac{1}{N}\sum_{i=1}^{N}(GHI_{forecasted,i} - GHI_{observed,i})}{\overline{GHI}_{observed}} \tag{3.19}$$

$$RMSE = \sqrt{\frac{1}{N}\sum_{i=1}^{N}(GHI_{forecasted,i} - GHI_{observed,i})^2} \tag{3.20}$$

$$rRMSE = \frac{RMSE}{\overline{GHI}_{observed}} = \frac{\sqrt{\frac{1}{N}\sum_{i=1}^{N}(GHI_{forecasted,i} - GHI_{observed,i})^2}}{\overline{GHI}_{observed}} \tag{3.21}$$

$$CORR = \frac{\sum_{i=1}^{N}(GHI_{observed,i} - \overline{GHI}_{observed})(GHI_{forecasted,i} - \overline{GHI}_{forecasted})}{\sqrt{\sum_{i=1}^{N}(GHI_{observed,i} - \overline{GHI}_{observed})^2}\sqrt{\sum_{i=1}^{N}(GHI_{forecasted,i} - \overline{GHI}_{forecasted})^2}} \tag{3.22}$$

Where N is the number of data, $GHI_{forecasted,i}$ and $GHI_{observed,i}$ represent the i^{th} forecasted and observed GHI, respectively, $\bar{}$ indicates its mean value.

Figure 3.6 (a) to **(c)** show correlation charts of the observed and the forecasted solar irradiances (GHIs) with WRF for the intra-day, next-day and 2-day ahead forecasting from July 1st, 2013 to June 30th, 2014. The chart of the persistent model is also shown in **Fig. 3.6 (e)**. The model applies the observation data in the previous day as solar irradiances of the intra-day forecasting. The model is useful as the reference of the numerical prediction model. The statistical indices, i.e. Bias, rBias, RMSE, rRMSE and

CORR, for each forecasting are summarized in **Table 3.3**. Besides, the ensemble mean in **Fig. 3.6 (d)** and **Table 3.3** are for the later discussion in the chapter 5.

The RMSEs and CORRs of the WRF forecasting results are better than those obtained by the persistent model. This shows the validity of the forecasting with WRF. The Bias of the persistent model is theoretically zero, and much smaller than the other forecasts.

Biases of the intra-day, next-day and 2-day ahead forecasting are 49.7 W/m^2, 51.4 W/m^2 and 50.8 W/m^2, respectively. From these results, the solar irradiance forecasting with WRF has a notable positive bias, which means that WRF overestimates the solar irradiance on the whole. According to Shimada *et al*. (2012), the positive bias in the irradiance forecasting might be the effect of atmospheric turbidity, which is not taken into account in the WRF model, and the actual atmosphere contains more cloud cover than the simulated results.

The aerosol optical depth (AOD) is a measure of the atmospheric turbidity. Aerosol Optical Depth (AOD) is the measure of aerosols (e.g., urban haze, smoke particles, desert dust, sea salt), which is a dimensionless parameter, distributed within a column of air from the instrument (earth's surface) to the top of the atmosphere. In particular, the value at 500nm wavelength is used as an index representing the atmospheric turbidity. The AOD is derived from direct and diffuse intensity measured with a sky radiometer, which is a sensitive solar radiometer for the routine automated measurement of direct and scattered solar radiation at multiple wavelengths (Aoki *et al*. 2013). The appearance of the sky radiometer installed at Gifu University (136.7˚E, 35.5˚N) is shown in **Fig. 3.7**.

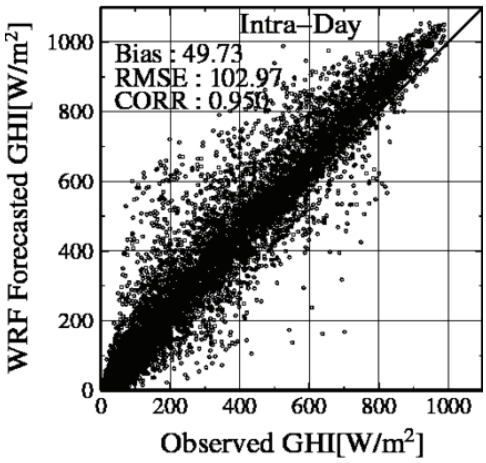

(a) Intra-Day Forecasting

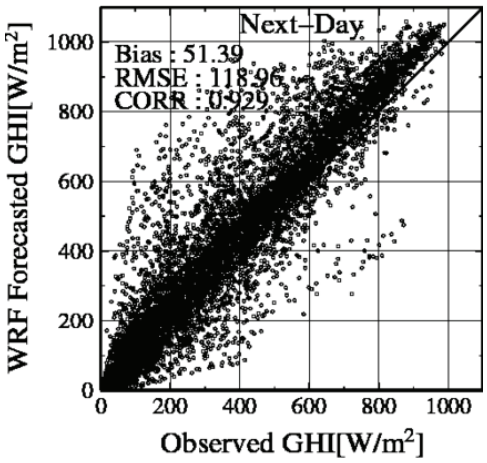

(b) Next-Day Forecasting

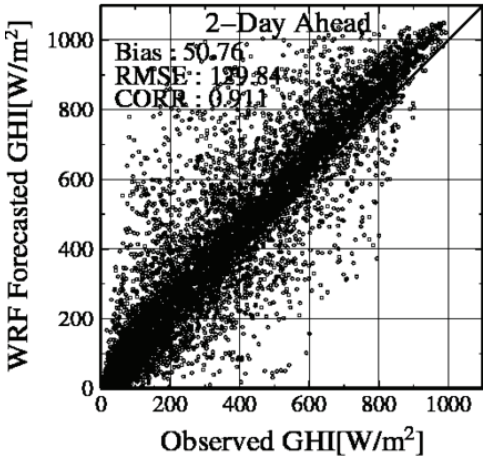

(c) 2-Day Ahead Forecasting

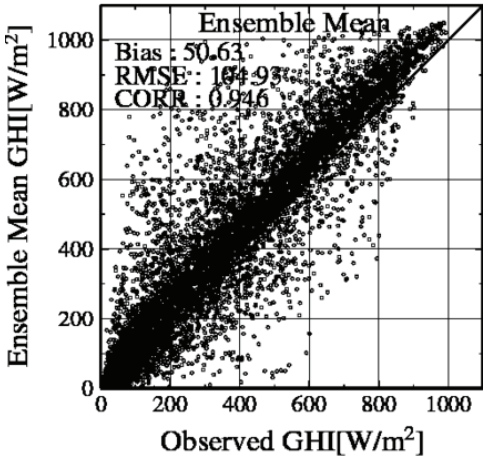

(d) Ensemble Mean

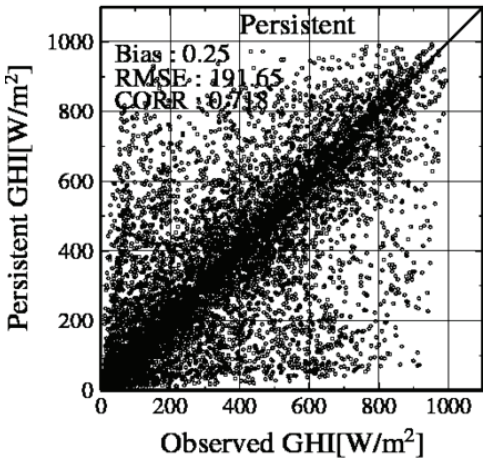

(e) Persistent

Fig. 3.6 Correlation charts of the intra-day, next-day, 2-day ahead forecasted solar irradiances, their ensemble mean and the persistent model with the observed data (61 observation-point average, from July 1st, 2013 to June 30th, 2014)

Fig. 3.7 Appearance of sky radiometer at Gifu University (136.7˚E, 35.5˚N) (Shimada et al. 2012)

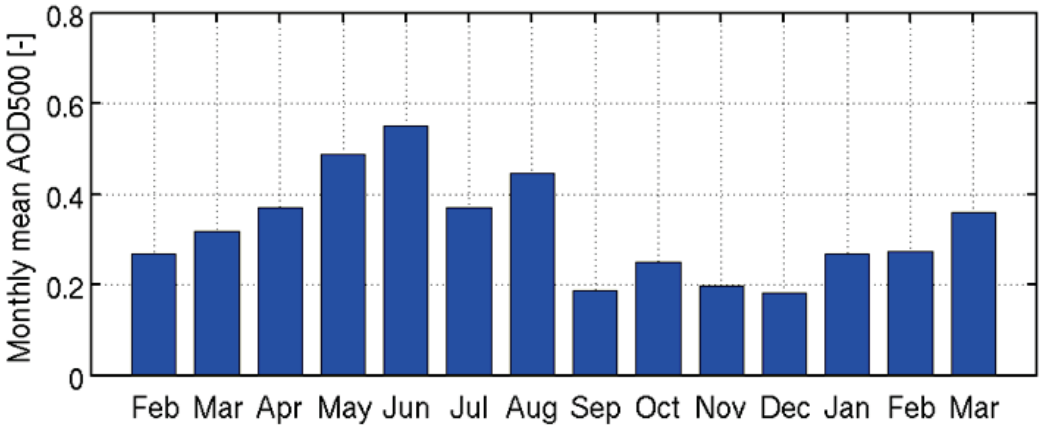

Fig. 3.8 Monthly mean aerosol optical depth (AOD) at 500nm obtained from skyradiometer measurements at Gifu University for February 2011 to March 2012 (Shimada et al. 2012)

Figure 3.8 shows the monthly mean aerosol optical depth (AOD) at 500nm obtained from sky radiometer measurements at Gifu University for February 2011 to March 2012. It is clear that the AOD has a tendency of increase in summer and has a tendency of decrease in winter as shown in **Fig. 3.8**, and the value of AOD on June 2011, which is maximum value during the observation period, is about 0.55. The Dudhia short wave radiation scheme, where the AOD representing the atmospheric turbidity over Boulder is about 0.1 according to Zamora *et al*. (2003), is used in the WRF model. The performance of the Dudhia scheme in simulating solar irradiance implies that the largest errors in the forecasted solar irradiance are found when aerosol scattering and absorption in the atmosphere exceeds the climatological value used in the WRF model. Consequently, the positive bias problem in the solar irradiance forecasting with WRF is presumably due to the atmospheric turbidity, whose value used in the radiation scheme of the WRF model is different from the actual conditions of the atmosphere in the central Japan.

The RMSE of the intra-day forecasting is 102.9 W/m^2, and it has the smallest value among these three forecasts. In contrast, the correlation coefficient (CORR) of the intra-day forecasting is 0.950, and it is the largest among them. From these statistical errors, it is found that the intra-day forecasting is the most accurate, and the forecasting error becomes larger as the forecasting time horizon becomes longer.

Table 3.3 Statistical error indices (Bias, RMSE and CORR) for the GHI forecasting of the intra-day forecasting, next-day forecasting, 2-day ahead forecasting, their ensemble mean and the persistent model (from July 1st, 2013 to June 30th, 2014)

Forecasting Method	Bias [W/m^2] (relative Bias)	RMSE [W/m^2] (relative RMSE)	CORR [-]
Intra-Day Forecasting	49.7 (28.8%)	102.9 (59.6%)	0.950
Next-Day Forecasting	51.4 (29.7%)	118.9 (68.9%)	0.929
2-Day Ahead Forecasting	50.8 (29.4%)	129.8 (75.2%)	0.911
Ensemble Mean	50.6 (29.3%)	104.9 (60.7%)	0.946
Persistent	0.3 (0.15%)	191.7 (110.9%)	0.718

3.4 Summary

The meteorological model WRF is used to produce 72-hour ahead solar irradiance forecasting covering the central region of Japan with a horizontal resolution of 2 km. The forecasting accuracy is evaluated with the on-situ observation data using different statistical error indices during the period from July 2013 to June 2014. The results are analyzed respectively for the intra-day, next-day and 2-day ahead forecasting with WRF.

Accuracy evaluation gives a RMSE of 102.9 W/m^2 (rRMSE: 59.6%) and correlation coefficient (CORR) of 0.950 for the intra-day forecasting, and a RMSE of 118.9 W/m^2 (68.9%) and CORR of 0.929 for the next-day forecasting, and a RMSE of 129.8 W/m^2 (75.2%) and CORR of 0.911 for the 2-day ahead forecasting. And the persistent model

has a RMSE of 191.7 W/m^2 (110.9%) and CORR of 0.718. Compared to the persistent model as a reference, the WRF model appears to be a viable method, which has enough accuracy, for the solar irradiance forecasting for respective forecast day.

Moreover, in terms of Bias, the WRF has a Bias of 49.7 W/m^2 for the intra-day forecasting, and a Bias of 51.4 W/m^2 for the next-day forecasting, and a Bias of 50.8 W/m^2 for the 2-day ahead forecasting. This result indicates that WRF-simulated GHI is found to have a notable positive bias in comparison with observation on the whole. One reason of the positive bias in the solar irradiance forecasting could be explained by the effect of atmospheric turbidity. The aerosol optical depth (AOD) value as its measure, used in the radiation scheme of the WRF model, is less than the actual one of the atmosphere conditions in the central Japan. It is considered as another reason of the positive bias that the actual atmosphere contains more cloud cover than the WRF-simulated results. Further investigations of improving the solar irradiance forecasting are required for more efficient use in evaluating the solar PV power generation.

Chapter 4 Increasing the accuracy of solar irradiance forecasting by applying Kalman Filter

4.1 Introduction

A comparison of the on-situ observations and the solar Global Horizontal Irradiance (GHI) simulated by WRF in the previous chapter has shown that the WRF-simulated GHIs include not only large root-mean-square-errors (RMSEs) but also positive biases.

Various post-processing approaches, like Model Output Statistics (MOS) (Lorenz *et al*. 2009; Rincón *et al*. 2011; Lorenz and Heinemann 2012; Verzijlbergh *et al*. 2015) and Kalman Filter, are frequently used in meteorology for adjusting the forecasting results obtained by Numerical Weather Prediction (NWP) models. Homleid (1995) describes a Kaman Filter model for estimating diurnal corrections of temperature forecasts. DE Carvalho *et al*. (2011) develops a Kalman Filter to correct the errors in mean temperature estimated by the PRECIS model, which is a system of regional climate prediction developed by the Hadley Centre in Endland (PRECIS 2001). Delle Monache *et al*. (2008) estimates systematic errors in surface ozone forecasts. Galanis *et al*. (2006), Cassola and Burlando (2012) apply the Kalman Filtering procedure to bias removal in wind speed forecasts. Pelland *et al*. (2013), Diagne *et al*. (2014) and Shimada *et al*. (2013) apply the Kalman Filter to bias removal in solar irradiance forecasts. Traditionally, MOS is mostly based on linear regression methods to create correction functions. The theory of the Kalman Filter (Kalman 1960) provides equations to modify recursively the estimations with observations.

In this work, the Kalman Filter is employed as a post-processing method to correct the systematic error of the forecasting for the solar irradiance. This chapter presents an

attempt at the improvement of the forecasting accuracy by using the bias-correction method.

4.2 Kalman Filter

Kalman Filter is designed to efficiently extract a signal from noisy data which contains statistical noise and other inaccuracies, and is therefore expected to show a more accurate performance with the training data (Diagne *et al*. 2014). This method is commonly used to correct systematic errors of the meteorological forecasting, and has been also adopted as one of the creation methods of the weather forecast guidances, e.g. precipitation amount, probability of precipitation and temperature, in the Japan Meteorological Agency (Kunitsugu 1997).

In general, the value at arbitrary time k in time series data would be affected in some way from the observed values at the time before the time k. Kalman Filter keeps track of the previous information as the system state, and updates it with the observation. Kalman Filter usually consists of two equations, the state equation and the observation equation.

$$x_k = Ax_{k-1} + w_k \tag{4.1}$$

$$z_k = Hx_k + v_k \tag{4.2}$$

Kalman Filter assumes that the state at time k is evolved from the previous state at time $k-1$ according to the state equation, Eq. (4.1). In this equation, x_k is a state variable, A is a state transition matrix and w_k is a state transition noise. The observation data z_k is evaluated from the state variable x_k according to the

observation equation, Eq. (4.2). H is a state-to-observation matrix and v_k is the noise in the observation data. In Kalman Filter, the noise is assumed to play an important role; both noises w_k and v_k are Gaussian zero mean white noises.

Figure 4.1 shows the computational procedure of Kalman Filter algorithm (Kim 2011). First, the initial values of the estimated state variable $\hat{x}_0$ and the error covariance matrix P_0, which is an internal variable, are set. The first step is for the prediction of system state and error covariance. The two variables $\hat{x}_k^-$ and P_k^-, which will be used throughout the step 2 through 4, are computed in this step. Here the superscript $^-$ denotes predicted value. In the step 2, Kalman gain K_k is being computed. The variable P_k^- computed in the previous step is used. H and R are the values preseted outside Kalman Filter. In the step 3, the system state estimation is computed from an observation given as input. The variable $\hat{x}_k^-$ is the one computed in the step 1. In the step 4, the error covariance is computed. The error covariance is a measure indicating how accurate the estimation is.

All the variables used in the algorithm are summarized in the **Table 4.1**. Categorizing the variables according to their usage helps overall understanding or implementation of the algorithm. The variables in 'System model' category, shown as A, H, Q, R, are not computed in Kalman Filter. These are the values preseted by the user according to the characteristics of the system and the purpose of Kalman Filter. In this table, all the variables except those categorized as 'System model' could not be changed arbitrarily by the user because these are computed by the algorithm. In other words, the four variables of the system model are the design factors for the performance of the Kalman Filter.

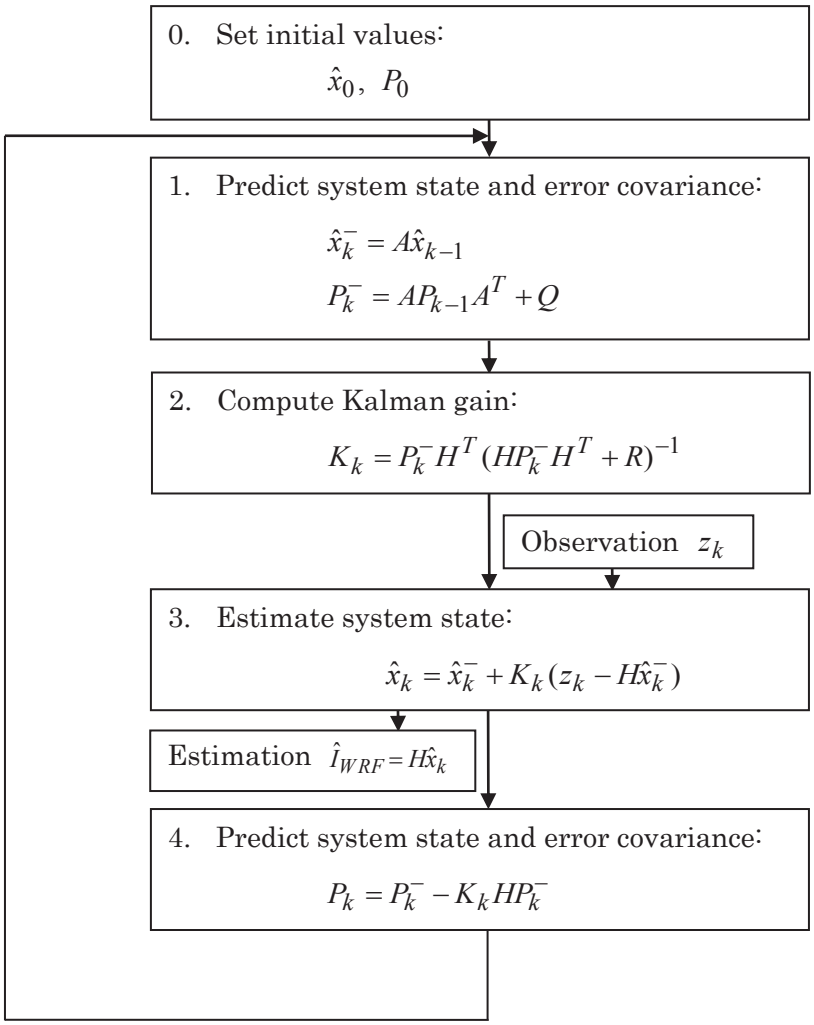

Fig. 4.1 Algorithm of Kalman Filter

In this study, the author applies Kalman Filter to correct the bias of the forecasted solar irradiance which corresponds to the system error of the forecasting. Kalman Filter is a mathematical method which can predict the future bias using a linear relationship between the present forecasting error and the estimated previous bias (Delle Monache *et al*. 2008; Shimada *et al*. 2013). After the current bias is estimated, it's removed from the solar irradiance forecasted with WRF to improve the forecasting.

Table 4.1 Classification of variables in the Kalman Filter algorithm, depending on their usage

Category	Variable	Description
External input	z_k	Observation at k time
Final output	$\hat{x}_k$	Estimated state variable at k time
System model	A	State transition matrix
	H	State-to-observation matrix
	Q	Error covariance of system state variable
	R	Error covariance of observation
For internal computation	$\hat{x}_k^-$	Predicted state variable at k time
	P_k^-	Predicted error covariance matrix of system state variable at k time
	P_k	Error covariance matrix of system state variable at k time
	K_k	Kalman gain at k time

4.2.1 Univariate Kalman Filter

The author formulates the univariate linear Kalman Filter in this section. Suppose that the estimated solar irradiance $\hat{I}_{WRF}$ with this univariate Kalman Filter is evaluated from the irradiance I_{WRF} only simulated with WRF with the following equation;

$$\hat{I}_{WRF} = aI_{WRF} + b \tag{4.3}$$

Where a and b are correction coefficients which change gradually in time. From this assumption, the state variable can be defined as $x_k = (a \quad b)^T$, and the state and observation equations, which correspond to Eqs. (4.1) and (4.2), can be derived as

follows;

$$x_k = Ax_{k-1} + w_k = \begin{pmatrix} 1 & 0 \\ 0 & 1 \end{pmatrix} \begin{pmatrix} a \\ b \end{pmatrix}_{k-1} + w_k \tag{4.4}$$

$$z_k = Hx_k + v_k = \begin{pmatrix} I_{WRF} & 1 \end{pmatrix} \begin{pmatrix} a \\ b \end{pmatrix}_k + v_k \tag{4.5}$$

Here the superscript T denotes a transposed matrix. The observation data z_k is $z_k = \hat{I}_{WRF}$.

The state transition noise w_k and the observation noise v_k in Eqs. (4.4) and (4.5), or their corresponding covariance matrices Q and R in **Fig. 4.1** are important parameters for the performance of the Kalman Filter. In this study, in order to detect the appropriate values, the author has conducted several WRF simulations with various matrices Q and R. **Figure 4.2** shows the root-mean-square error, RMSE, of the solar irradiance intra-day forecasting under various determinants of matrices Q and R. The appropriate ratio between the determinants Q and R which minimizes the forecasting RMSE can be found from this figure. Consequently, this work employ $1 \times 10^0 \begin{pmatrix} 1 & 0 \\ 0 & 1 \end{pmatrix}$ and $1 \times 10^{1\,1.5}$ for the covariance matrices Q and R, respectively, to minimize the forecasting error.

Figure 4.3 shows the time series of the coefficients a and b of the correction equation Eq. (4.3), which are the system state variables of the univariate Kalman Filter. The coefficient b increases in time, but its magnitude is negligible compared with the solar irradiance whose order is about 100 or 1,000 W/m^2. The coefficient a changes seasonally. Both coefficients change in time in the filter, and work to adjust the solar irradiance forecasted with WRF.

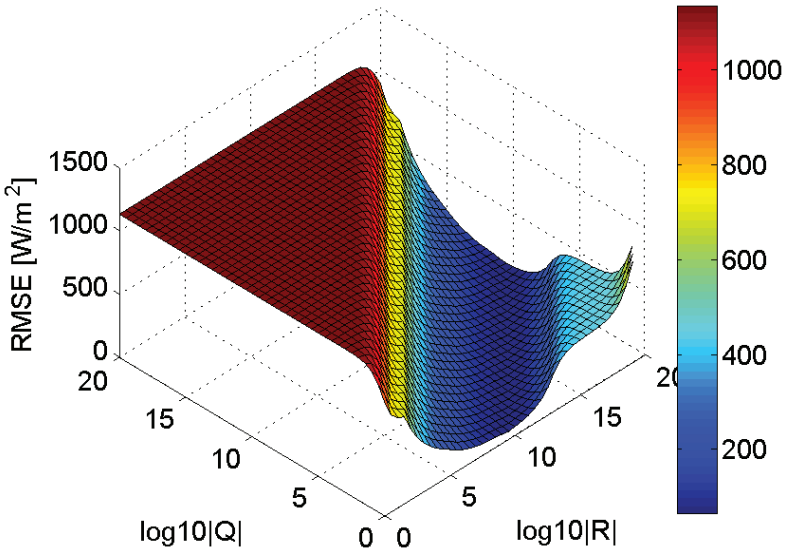

Fig. 4.2 Root mean square error (RMSE) of the intra-day forecasting of the solar irradiance under the various determinants of covariance matrices Q and R

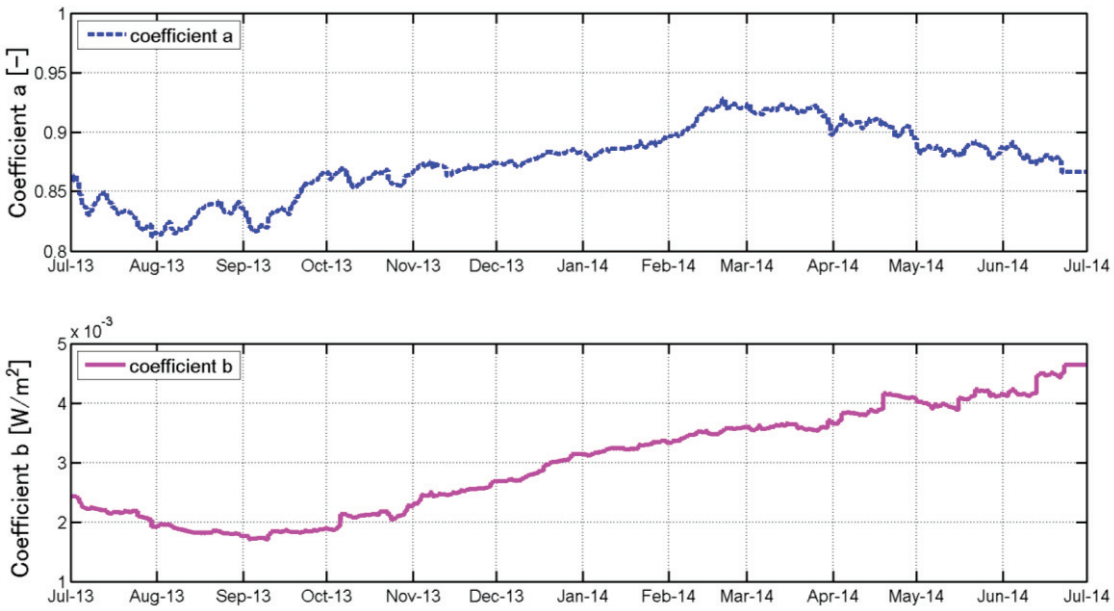

Fig. 4.3 Time series of correction coefficients obtained from the univariate Kalman Filter in the intra-day forecasting during July 2013 and July 2014

4.2.2 Multivariate Kalman Filter

Multivariate linear Kalman Filter is formulated in this section. Suppose that the estimated solar irradiance $\hat{I}_{WRF}$ with this multivariate Kalman Filter is evaluated from multiple weather elements simulated with WRF with the following equation;

$$\hat{I}_{WRF} = a_1 I_{WRF} + a_2 I_0 + a_3 RHH + a_4 RHM + a_5 RHL + a_6 PW + a_7 \tag{4.6}$$

Where a_1, a_2, a_3, a_4, a_5, a_6 and a_7 are correction coefficients which change gradually in time. From this assumption, the state variable can be defined as $x_k = (a_1 \quad a_2 \quad a_3 \quad a_4 \quad a_5 \quad a_6 \quad a_7)^T$, and the state and observation equations, which correspond to Eqs. (4.1) and (4.2), can be derived as follows;

$$x_k = Ax_{k-1} + w_k = \begin{pmatrix} 1 & 0 & 0 & 0 & 0 & 0 & 0 \\ 0 & 1 & 0 & 0 & 0 & 0 & 0 \\ 0 & 0 & 1 & 0 & 0 & 0 & 0 \\ 0 & 0 & 0 & 1 & 0 & 0 & 0 \\ 0 & 0 & 0 & 0 & 1 & 0 & 0 \\ 0 & 0 & 0 & 0 & 0 & 1 & 0 \\ 0 & 0 & 0 & 0 & 0 & 0 & 1 \end{pmatrix} \begin{pmatrix} a_1 \\ a_2 \\ a_3 \\ a_4 \\ a_5 \\ a_6 \\ a_7 \end{pmatrix}_{k-1} + w_k \tag{4.7}$$

$$z_k = Hx_k + v_k = \begin{pmatrix} I_{WRF} & I_0 & RHH & RHM & RHL & PW & 1 \end{pmatrix} \begin{pmatrix} a_1 \\ a_2 \\ a_3 \\ a_4 \\ a_5 \\ a_6 \\ a_7 \end{pmatrix}_k + v_k \tag{4.8}$$

Where the superscript T denotes a transposed matrix. The observation data z_k is $z_k = \hat{I}_{WRF}$. $\hat{I}_{WRF}$ is the WRF-simulated GHIs after applying the multivariate linear

Kalman Filter (WRF-mvKF), $\hat{x}_k$ is a system state variable represented in the form of the vector, H is a transformation matrix, I_{WRF} is the WRF-simulated GHIs (WRF), I_0 is solar irradiance GHI outside the earth's atmosphere, RHH is the maximum value of the WRF-simulated relative humidity at the upper atmosphere (400~50hPa), RHM is the maximum value of the WRF-simulated relative humidity at the middle atmosphere (800~400hPa), RHL is the maximum value of the WRF-simulated relative humidity at the lower atmosphere (surface~800hPa), PW is the WRF-simulated precipitable water. These variables are selected from the meteorological parameters obtained from the atmospheric radiation scheme in the WRF simulation.

Except that corrective factors vary with time, the basic concept of multivariate Kalman Filter is the same as the multivariate linear regression analysis. In order to avoid the problem of multicollinearity, Principal Component Analysis (PCA) is employed to remove the correlations among variables.

PCA is a mathematical procedure that uses an orthogonal transformation to convert a set of computational values of possibly correlated variables into a set of values of linearly uncorrelated variables called principal component (PC). In a first step, in view of the difference of size among variables, meteorological data are normalized by the equation (4.9).

$$X = \frac{x - \bar{x}}{\sigma} \tag{4.9}$$

Where σ is standard deviation of each variable (x), $\bar{x}$ is mean of each variable. Mean is 0, and variance is 1 after normalizing for each variable.

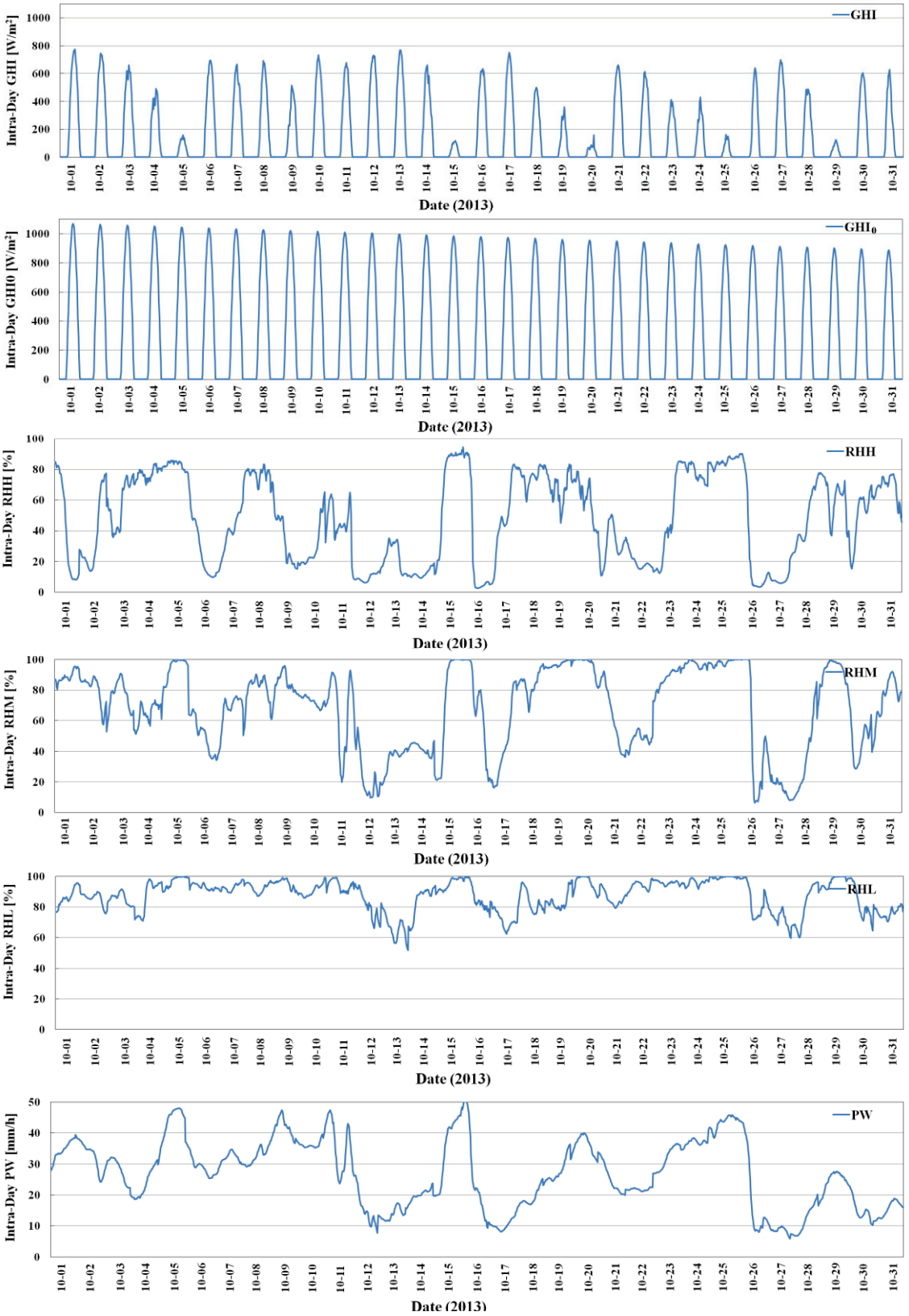

Fig. 4.4 Time series of multiple weather elements simulated with WRF for the intra-day forecasting during Oct 1st to 31st, 2013

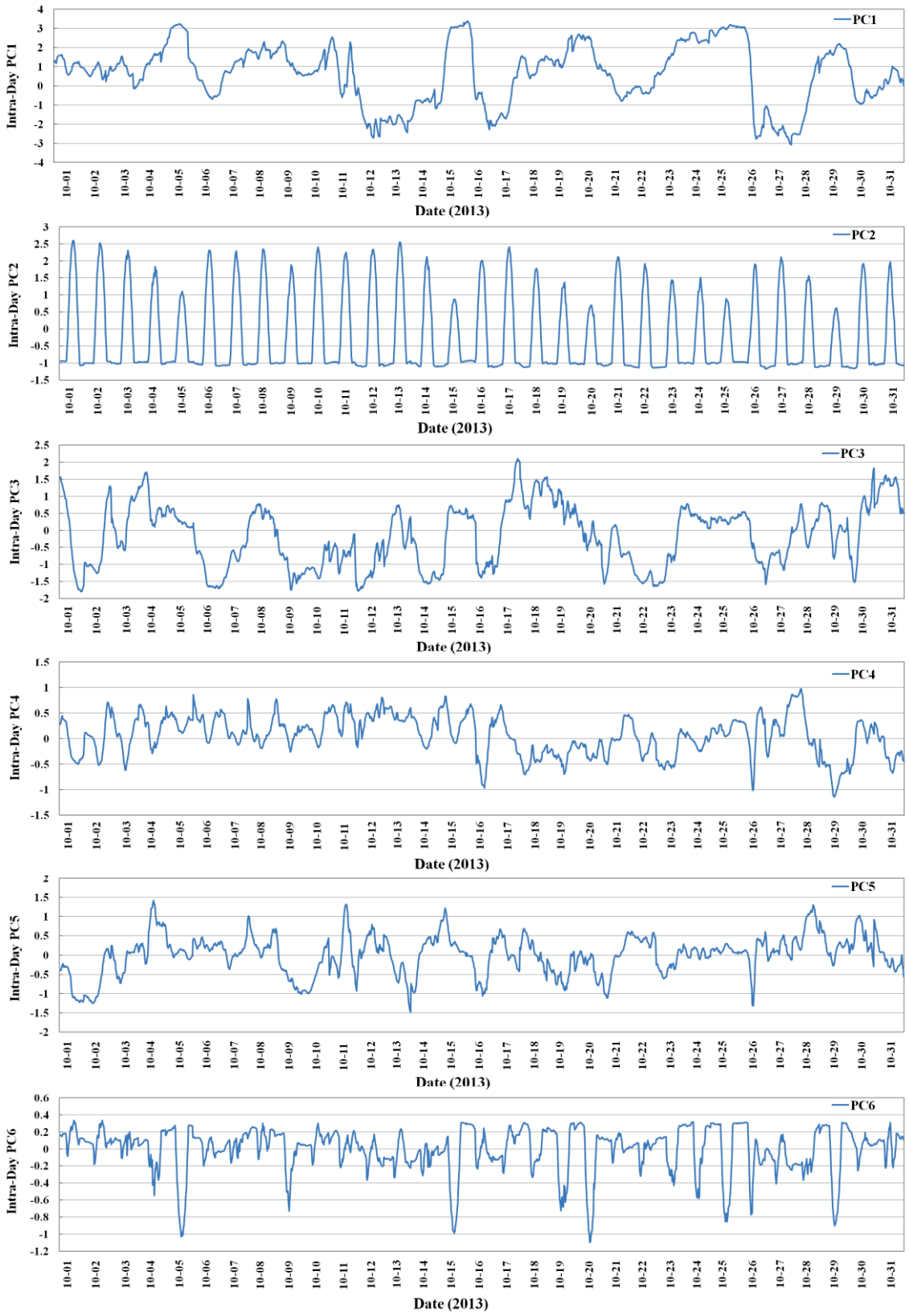

Fig. 4.5 Time series of multiple principal components (PC) obtained from Principal Component Analysis (PCA) for the intra-day forecasting during Oct 1st to 31st, 2013

In this study, principal components are computed using the covariance method. First, find the covariance matrix (Correlation matrix). Next, find the eigenvectors and eigenvalues of the correlation matrix. Finally, obtain the weight coefficient of each principal component (PC). **Table 4.2** shows combination coefficient of respective principal component (PC). **Table 4.3** shows the contribution ratio of respective principal component to the solar irradiance forecasting. **Figure 4.4** shows time series of multiple weather elements simulated with WRF, and **Fig. 4.5** shows the ones of multiple principal components obtained from WRF outputs and principal component analysis for the intra-day forecasting during the period from Oct 1st to 31st, 2013.

Table 4.2 Combination coefficient of respective principal component (PC)

Variable	No.1-PC [-]	No.2-PC [-]	No.3-PC [-]	No.4-PC [-]	No.5-PC [-]	No.6-PC [-]
I_{WRF}	-0.068	0.702	-0.034	-0.010	0.011	0.708
I_0	0.044	0.702	-0.006	-0.139	0.068	-0.694
RHH	0.438	0.026	0.769	0.190	0.421	0.050
RHM	0.540	-0.018	0.147	-0.595	-0.571	0.077
RHL	0.496	-0.070	-0.554	-0.258	0.608	0.077
PW	0.513	0.097	-0.280	0.724	-0.350	-0.046

Table 4.3 Proportion and weight value for respective principal component (PC)

Principal component	Weight [-]	Proportion [%]
No.1-PC	2.613	43.55
No.2-PC	1.949	32.48
No.3-PC	0.739	12.32
No.4-PC	0.390	6.50
No.5-PC	0.254	4.23
No.6-PC	0.055	0.92
Total	6	100

Usually, the strength of the linear association between two variables X and Y is quantified by the correlation coefficient, denoted by r. The variables X and Y can be written as datasets x_i and y_i, for $i = 1, 2, \cdots, N$. The mathematical formula for computing r is given by

$$r = \frac{\sum_{i=1}^{N}(x_i - \bar{x})(y_i - \bar{y})}{\sqrt{\sum_{i=1}^{N}(x_i - \bar{x})^2} \cdot \sqrt{\sum_{i=1}^{N}(y_i - \bar{y})^2}} \tag{4.10}$$

Where N is the number of pairs of data, $\bar{x}$ and $\bar{y}$ are the mean values of X and Y. The value of r is such that $-1 \le r \le 1$. The + and – sign is used for positive linear correlation and negative linear correlation, respectively.

Since the formula for calculating the correlation coefficient standardizes the variables, changes in scale or units of measurement will not affect its value. For this reason, the correlation coefficient is often useful in determining the strength of the

association between two variables. A correlation greater than 0.8 is generally described as strong, whereas a correlation less than 0.5 is generally described as weak.

Correlation coefficients of series with different weather elements simulated by WRF during the period from July 2013 to June 2014 are shown in **Table 4.4**, and the ones with different principal components are shown in **Table 4.5**. The collinearity of multiple weather elements related to the atmosphere radiation becomes even clearer at some level (**Table 4.4**); for example, there is a strong association between I_{WRF} and I_0, and there is a moderate association between RHH and RHM. It should be noted that the respective principal components are completing uncorrelated (**Table 4.5**). Based on the above, the PCA works well in terms of overcoming the multicollinearity problem among multiple variables.

Table 4.4 Correlation coefficients of series with different weather elements simulated by WRF during the period from July 2013 to June 2014

Variable	I_{WRF}	I_0	*RHH*	*RHM*	*RHL*	*PW*
I_{WRF}	1.000	0.926	-0.059	-0.121	-0.163	0.045
I_0	0.926	1.000	0.077	0.055	-0.015	0.149
RHH	-0.059	0.077	1.000	0.597	0.296	0.450
RHM	-0.121	0.055	0.597	1.000	0.615	0.573
RHL	-0.163	-0.015	0.296	0.615	1.000	0.640
PW	0.045	0.149	0.450	0.573	0.640	1.000

Table 4.5 Correlation coefficients of series with different principal components (PC) during the period from July 2013 to June 2014

Variable	No.1-PC	No.2-PC	No.3-PC	No.4-PC	No.5-PC	No.6-PC
No.1-PC	1.000	-0.000	-0.000	0.000	-0.000	0.000
No.2-PC	-0.000	1.000	-0.000	0.000	-0.000	0.000
No.3-PC	-0.000	-0.000	1.000	0.000	-0.000	0.000
No.4-PC	0.000	0.000	0.000	1.000	0.000	-0.000
No.5-PC	-0.000	-0.000	-0.000	0.000	1.000	0.000
No.6-PC	0.000	0.000	0.000	-0.000	0.000	1.000

4.3 Solar irradiance forecasting with Kalman Filter

As described in Chapter 3, the WRF computes 72-hour ahead forecasting for the solar irradiance GHI. In this section, the solar GHI is computed by WRF with the Kalman Filter as a post-processing method, and is compared with the observed data. As explained before, the global horizontal irradiance (GHI) averaged in 61 sites in **Fig. 2.3** and with 30-minute interval is used for the verification. The data in night time are rejected for the verification. The Kalman Filter is applied to the 61 observation-point averaged irradiance GHI.

Figure 4.6 shows correlation charts between the observed and the forecasted solar irradiance GHI with WRF and univariate Kalman Filter (WRF-KF), and **Fig. 4.7** shows the ones between the observed and the forecasted GHI with WRF and multivariate Kalman Filter (WRF-mvKF). The intra-day, next-day and 2-day ahead forecasting are analyzed separately. It is detected that better agreements between the observed and the

forecasted irradiance GHI with WRF and Kalman Filters could be achieved in a way in these figures. In addition, the ensemble mean forecasting with WRF and Kalman Filters (**Fig. 4.6 (d)** and **Fig. 4.7 (d)**) are for the later discussion in the chapter 6.

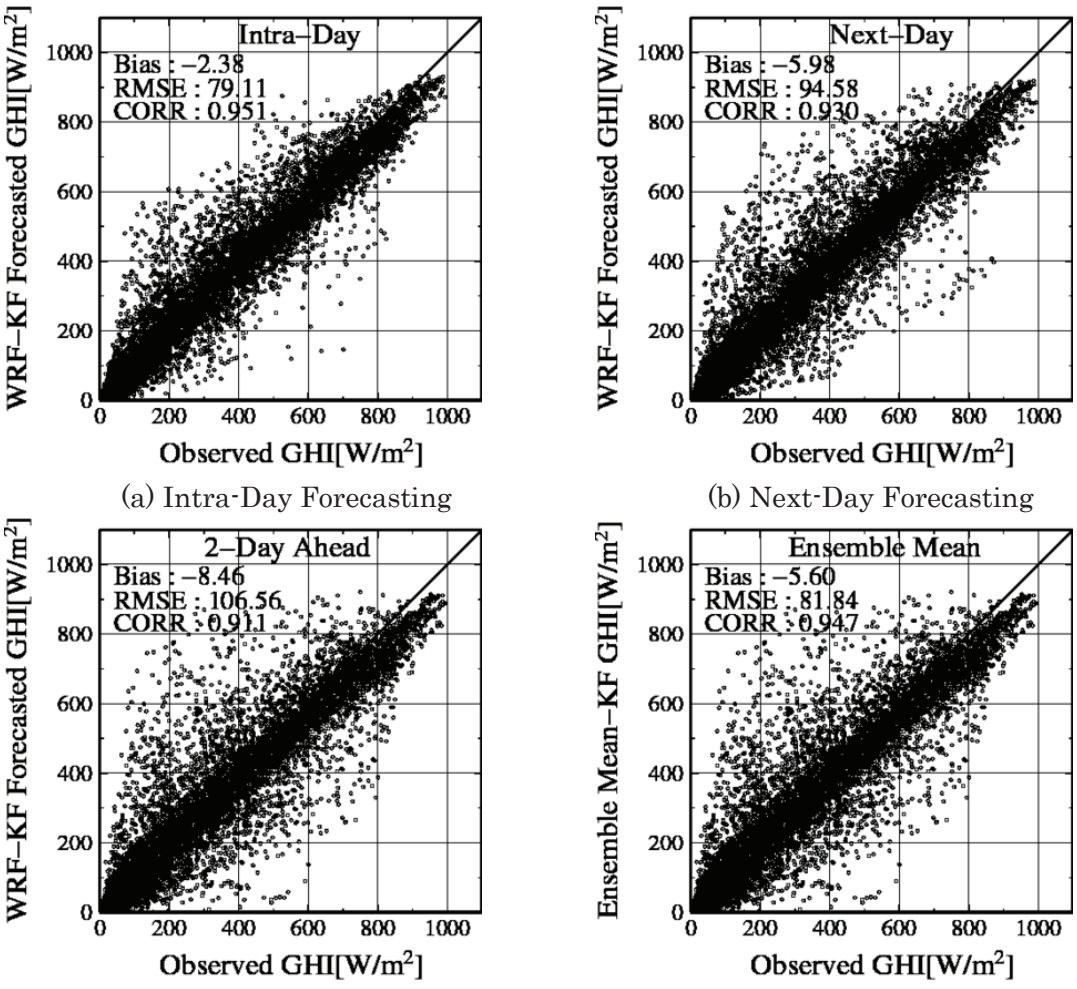

(a) Intra-Day Forecasting

(b) Next-Day Forecasting

(c) 2-Day Ahead Forecasting

(d) Ensemble Mean-KF

Fig. 4.6 Correlation charts of the intra-day, next-day, 2-day ahead forecasted solar irradiances, and their ensemble mean with WRF and univariate Kalman Filter (WRF-KF) with the observed data (61 observation-point average, from July 1st, 2013 to June 30th, 2014)

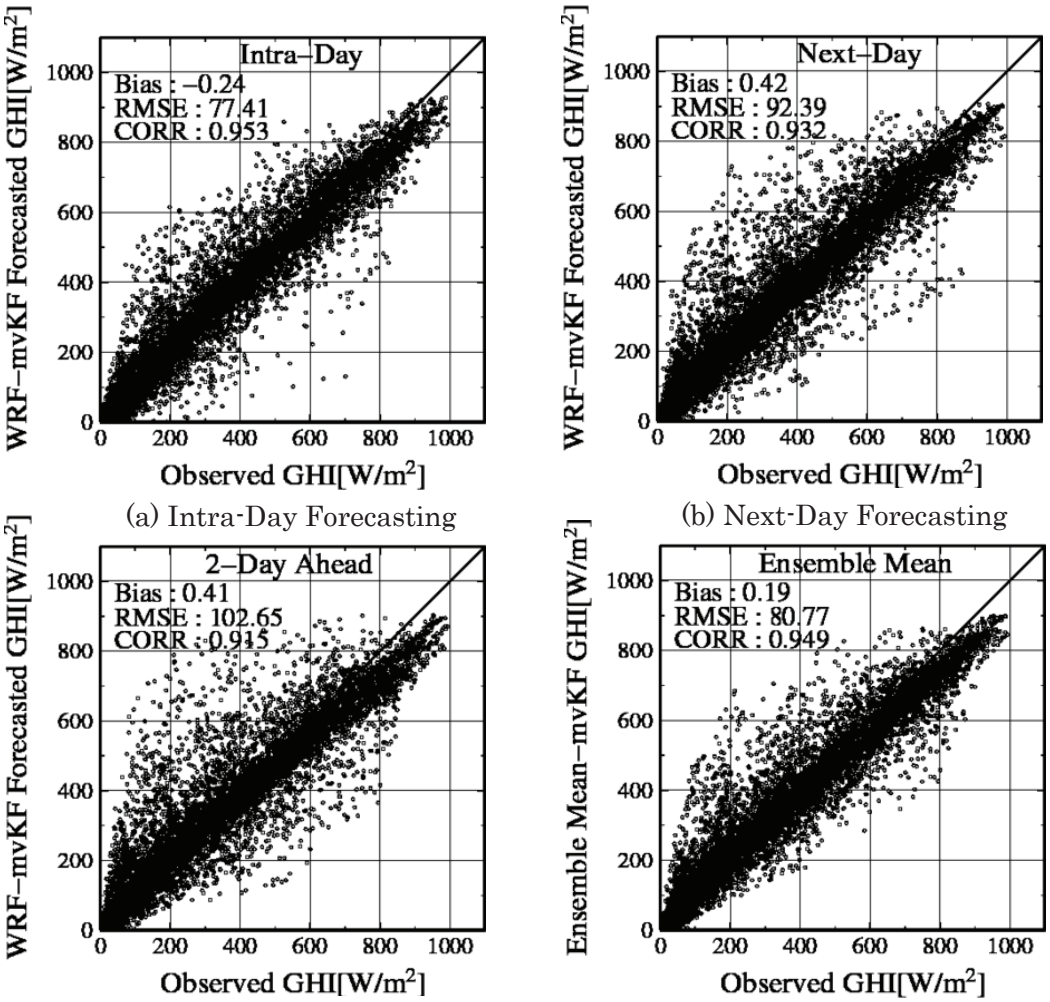

(a) Intra-Day Forecasting (b) Next-Day Forecasting

(c) 2-Day Ahead Forecasting (d) Ensemble Mean-mvKF

Fig. 4.7 Correlation charts of the intra-day, next-day, 2-day ahead forecasted solar irradiances, and their ensemble mean with WRF and multivariate Kalman Filter (WRF-mvKF) with the observed data (61 observation-point average, from July 1st, 2013 to June 30th, 2014)

An overall evaluation of the forecast accuracy (i.e. statistical error indices) for different forecasting approaches in dependence on the forecast horizon is given in **Table 4.6**. The results are grouped according to the forecast day. Results for the first forecast day (i.e. intra-day) integrate forecast horizons up to 24 h, and the second forecast day (i.e. next-day) integrates forecast horizons from 25 to 48 h, and the third forecast day

(i.e. 2-day ahead) includes forecast horizons from 49 to 72 h. The evaluation was performed during the period from July 1st, 2013 to June 30th, 2014. Moreover, for respective forecast horizon, all approaches show a significant improvement in comparison to the persistent model, which is described in the section 3.3.

Because of the application of Kalman Fitler, the positive biases of WRF-simulated GHI for respective forecast day are almost corrected on the whole. For the forecasting method WRF-KF, the Biases of the intra-day, next-day and 2-day ahead forecasting are -2.38 W/m², -5.98 W/m² and -8.46 W/m² respectively, and for the forecasting method WRF-mvKF, their Biases are -0.24 W/m², 0.42 W/m² and 0.41 W/m² separately.

Meanwhile, compared to the forecasting method WRF, the RMSEs of the intra-day, next-day and 2-day ahead forecasting for WRF-KF are improved around 23.2%, 20.5% and 17.9% respectively, and the ones with WRF-mvKF are around 24.8%, 22.3% and 20.9% respectively. Furthermore, their corresponding correlation coefficients (CORRs) are slightly increased as well.

Consequently, the results of accuracy evaluation indicate that WRF-mvKF gave better results for solar irradiance GHI forecasting, compared to WRF-KF. From the aspect of the relative values of statistical error indices, the rBias corrects to -0.14%, the rRMSE amounts to 44.8%. Also, the correlation coefficient (CORR) increases from 0.950 of WRF forecasting to 0.953 for the intra-day forecasting using WRF-mvKF. For next-day forecasting, the rBias of WRF-mvKF decreases to 0.24%, the rRMSE decreases to 53.5% and the CORR increases from 0.929 to 0.932. For 2-day ahead forecasting, the rBias of WRF-mvKF decreases to 0.23%, the rRMSE increases to 59.4%, and the CORR increases from 0.911 to 0.915.

Table 4.6 Statistical error indices (Bias, RMSE and CORR) for the GHI forecasting of the intra-day forecasting, next-day forecasting, 2-day ahead forecasting, their ensemble mean, and the persistent model (from July 1st, 2013 to June 30th, 2014). WRF is the forecasted result with WRF only, and WRF-KF is with WRF and univariate Kalman Filter, and WRF-mvKF is with WRF and multivariate Kalman Filter.

Forecasting Method		Bias [W/m^2] (relative Bias)	RMSE [W/m^2] (relative RMSE)	CORR [-]
Intra-Day Forecasting	WRF	49.73 (28.79%)	102.97 (59.60%)	0.950
	WRF-KF	-2.38 (-1.38%)	79.11 (45.79%)	0.951
	WRF-mvKF	-0.24 (-0.14%)	77.41 (44.81%)	0.953
Next-Day Forecasting	WRF	51.39 (29.75%)	118.96 (68.85%)	0.929
	WRF-KF	-5.98 (-3.46%)	94.58 (54.74%)	0.930
	WRF-mvKF	0.42 (0.24%)	92.39 (53.48%)	0.932
2-Day Ahead Forecasting	WRF	50.76 (29.38%)	129.84 (75.15%)	0.911
	WRF-KF	-8.46 (-4.89%)	106.56 (61.68%)	0.911
	WRF-mvKF	0.41 (0.23%)	102.65 (59.42%)	0.915
Ensemble Mean	WRF	50.63 (29.30%)	104.93 (60.74%)	0.946
	WRF-KF	-5.60 (-3.24%)	81.84 (47.41%)	0.947
	WRF-mvKF	0.26 (0.16%)	80.83 (46.82%)	0.949
Persistent		0.3 (0.15%)	191.7 (110.9%)	0.718

It should be noted that the post-processing method Kalman Filters used in this study are exclusively based on statistical properties of the forecasting errors and do not use the physical properties of solar irradiance.

4.4 Summary

It has been shown that there are systematic deviations (i.e. bias) between the forecasted values by the meteorological model WRF and the observed values. Accordingly, the post-processing approach Kalman Filter is employed for correcting the WRF forecasting. One advantage of the Kalman Filter as compared to traditional statistical method is that the correction is continuously updated with the latest observation. Another advantage is its simplicity.

The solar irradiance forecasting for 72 hours ahead is discussed with WRF and Kalman Filter during the period from July 2013 to June 2014, and the accuracy is verified with the on-situ observation data. The results are analyzed separately for the univariate Kalman Filter and the multivariate Kalman Filter. In the linear combinations of the forecasted variables of the latter, principal component analysis (PCA) is applied to overcome the multicollinearity among multiple variables. As a consequence, both applications of Kalman Filter are significantly effective in improving the accuracy of the forecasted solar irradiance GHI from WRF model. Meanwhile, the forecasting accuracy becomes lower as the forecasting time horizon becomes longer.

More precisely, the WRF-KF has an overall Bias of -2.38 W/m² (rBias: -1.38%) for the intra-day forecasting, increasing to -8.46 W/m² (-4.89%) for the 2-day ahead forecasting, and the WRF-mvKF has an overall Bias of -0.24 W/m² (rBias: -0.14%) for

the intra-day forecasting, increasing to 0.41 W/m^2 (0.23%) for the 2-day ahead forecasting. These results indicate that the positive biases of WRF-simulated GHI for respective forecast day are almost corrected.

The WRF-KF has an overall RMSE of 79.11 W/m^2 (rRMSE: 45.8%) for the intra-day forecasting, increasing to 106.6 W/m^2 (61.7%) for the 2-day ahead forecasting, and the WRF-mvKF has an overall RMSE of 77.4 W/m^2 (rRMSE: 44.8%) for the intra-day forecasting, increasing to 102.7 (59.4%) W/m^2 for the 2-day ahead forecasting. In comparison with WRF, both Kalman Filters lower the RMSEs and its relative values for respective forecast day, indicating the improvement of WRF forecasting.

Furthermore, correlation coefficients (CORRs) of both Kalman Filters for respective forecast day are also slightly increased as compared to the ones with WRF.

Chapter 5 Ensemble forecasting of solar irradiance using WRF

5.1 Introduction

Since the forecasting error of solar irradiance will have a relatively large influence in the projection of PV power generation (Lorenz *et al*. 2009), the information on the forecasting reliability is of great importance. It is known that a forecast is an estimate of the future state of the atmosphere. It is created by estimating the current state of the atmosphere using observations, and then calculating how this state will evolve in time using a numerical weather prediction model. As the atmosphere is a chaotic system, very small errors in its initial state can lead to large errors in the forecast. In order to estimate the forecasting reliability of solar irradiance, which is about the coverage rate of the prediction interval, ensemble forecasting is introduced. This chapter aims to evaluate the prediction interval of solar irradiance forecasting.

In the chapter 3, the solar irradiance forecasted with the meteorological model WRF shows the positive bias, e.g. 49.7 W/m^2 for the intra-day forecasting, in comparison with the observation data, but its accuracy is acceptable for the forecasting. The author will keep on employing the WRF model for the ensemble forecasting of the solar irradiance.

5.2 Methodology

5.2.1 Ensemble forecasting method

Ensemble forecasting method is used for quantifying uncertainties in weather prediction. Each computed result operated under the ensemble forecasting methods is called a member. The ensemble forecasting methods are categorized with the groups of

the members, e.g. members computed with different models, or members with different initial conditions. Hoffman and Kalnay (1983) suggests that, compared with Monte Carlo Forecasting (MCF) (Leith 1974; Seidman 1981) which is one of the common ensemble methods, the Lagged Averaged Forecast (LAF) method has an advantage to increase the ensemble member amount. In this study, the LAF method is employed to the ensemble forecasting of the solar irradiance. Each LAF ensemble member is computed with different initial conditions with different initial time. All the forecasting results in an ensemble are similar, indicating that the forecasting can be more confident, whereas they are different, indicating that uncertainty of forecasting must be taken more account of.

5.2.2 Ensemble forecasting system of solar irradiance

The diagram of the operation cycle of the solar irradiance (Global Horizontal Irradiance, GHI) ensemble forecasting is shown in **Fig. 5.1**. Let us call a member $M_{i,j}$ as the computed result in the operation day i, and the forecasting day horizon j. Therefore, the members of $j=0,\ 1$ and 2 correspond to the results of the intra-day, next-day and 2-day ahead forecasting, respectively from the operation day. As depicted in the figure, the solar irradiance of the intra-day forecasting in the operation day i is forecasted with three members; the intra-day forecasting computed in the operation day i, $M_{i,0}$, the next-day forecasting computed in the previous day $i-1$, $M_{i-1,1}$, and the 2-day ahead forecasting computed in the day before the previous day $i-2$, $M_{i-2,2}$. The number of the members for the next-day forecasting of the latest computation (i.e., the computation in the operation day i) is two as revealed in **Fig. 5.1**, and is only one for the 2-day ahead forecasting.

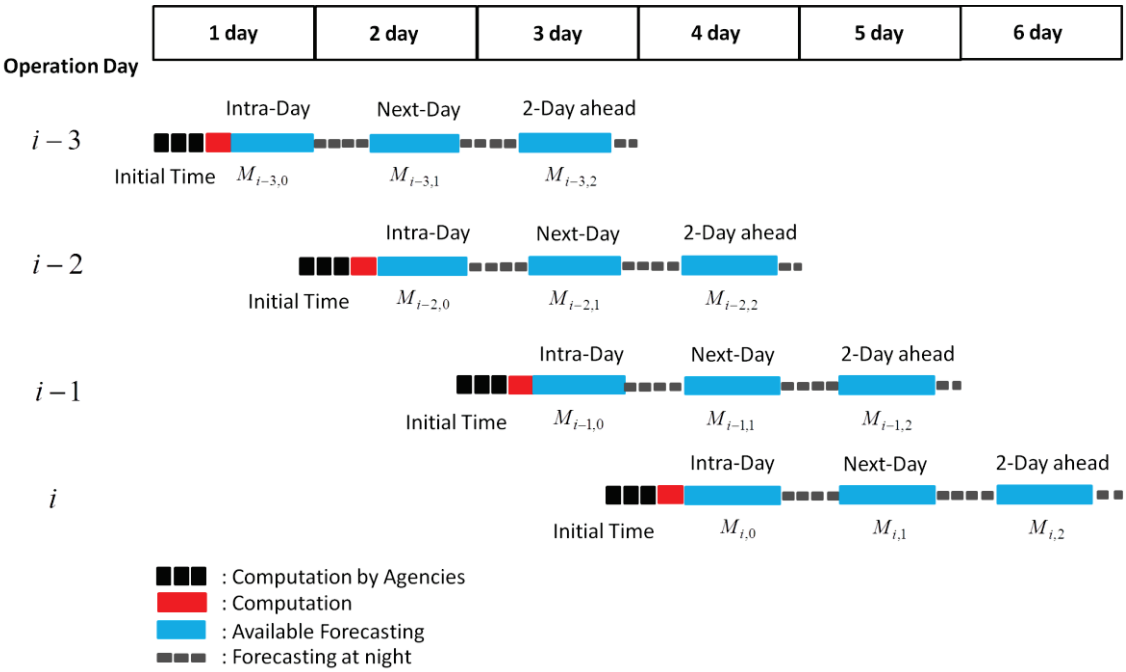

Fig. 5.1 Operation cycles of solar irradiance (GHI) ensemble forecasting using WRF.

$M_{i,j}$ is an ensemble member of $j-$day ahead forecasting in the operation day i.

5.2.3 Ensemble mean of solar irradiance forecasting

The accuracy of the solar irradiance forecasting computed with WRF has been discussed already in the section 3.3. The discussion is taken up again here for the ensemble forecasting method. The correlation charts of the intra-day, next-day and 2-day ahead forecasting, which are corresponding to the ensemble members $M_{i,0}$, $M_{i,1}$ and $M_{i,2}$, are shown as **Fig. 3.6 (a)** to **(c)**. The chart of ensemble mean is added in **Fig. 3.6 (d)**. The ensemble mean is calculated as an average of the members for the same target day, e.g. the three members $M_{i,0}$, $M_{i-1,1}$, $M_{i-2,2}$ for the intra-day forecasting in the operation day i. The statistical indices of the forecasting error including the ensemble mean are already indicated in **Table 3.3**. The error indices of the ensemble mean are better than the ones of the next-day and 2-day ahead forecasting as indicated

in the table, however the ones of the intra-day forecasting are better than the ensemble mean.

Usually the ensemble mean is employed as the forecasted value in the ensemble forecasting methods. However the intra-day forecasting $M_{i,0}$ is applied as the forecasted value, because the accuracy of the intra-day forecasting is the highest in **Fig. 3.6** and **Table 3.3**.

5.2.4 Ensemble spread and coverage rate

Figure 5.2 shows an example of the forecasted solar irradiance (Global Horizontal Irradiance, GHI) computed in one day. The computed results in the figure contain the intra-day, next-day and 2-day ahead forecasting. The ensemble spread is also indicated in the figure. The spread is defined as the standard deviation of the ensemble members, and is calculated with the following equation.

$$Spread_{i,j} = \sqrt{\frac{1}{N-j} \sum_{k=0}^{N-j-1} (GHI_{i-k,j+k} - \overline{GHI})^2} \tag{5.1}$$

Where j is the target day horizon, and $j = 0$, 1 and 2 correspond to the intra-day, next-day and 2-day ahead forecasting in the operation day i, respectively. $GHI_{i-k,j+k}$ is the forecasted solar irradiance, Global Horizontal Irradiance (GHI) of the member $M_{i-k,j+k}$. N is the number of forecasted days in one operation, and it is 3 in this study. $N-j$ corresponds to the number of ensemble members. $\overline{GHI}$ is the averaged GHI of the target members. When the variation among the members is large, the spread becomes also large, and the reliability of the forecasting may be low.

Therefore the spread may be used as the parameter of unreliability of forecasting.

The number of ensemble members of the intra-day, next-day and 2-day ahead forecasting in **Fig. 5.2** is 3, 2 and 1, respectively. The spread of the 2-day ahead forecasting is always zero because the number of its ensemble members is only 1.

In this study, three days forecasting, i.e. the intra-day, next-day, 2-day ahead forecasting, is performed. Here the author focuses on the intra-day forecasting, because the number of its ensemble members is 3 and more than others. **Figure 5.3** shows the relationship between the spread of the intra-day forecasting and its forecasting error from the observation during the period from Sep 1st to Nov 30th, 2013. The upper and lower bounds of the forecasting error interval with the coverage rates 50%, 80%, 90% and 95% are also drawn with lines in the figure. These lines are evaluated with every 10 W/m^2 in the spread, and also evaluated positive and negative errors separately. Occurrence frequency of the forecasting error within the spread interval of interest is defined as coverage rate in this study. The plotted data converge symmetrically around the horizontal line $x = 30$ W/m^2, and the forecasting error diverges widely as the spread becomes large as shown with the bound lines of the intervals.

The bound lines of the forecasting error interval are not smooth, because the number of ensemble members are limited, only 3, and the spread may contain random error. It causes the limitation of the computational environment in this work. Increasing of ensemble members may contribute for the improvement of the interval estimation.

The distribution of the plots and the bound lines of the member $M_{i,0}$, which is the computed results with the meteorological model WRF, deflects to the positive side, because WRF has the tendency to overestimate the solar irradiance as explained before.

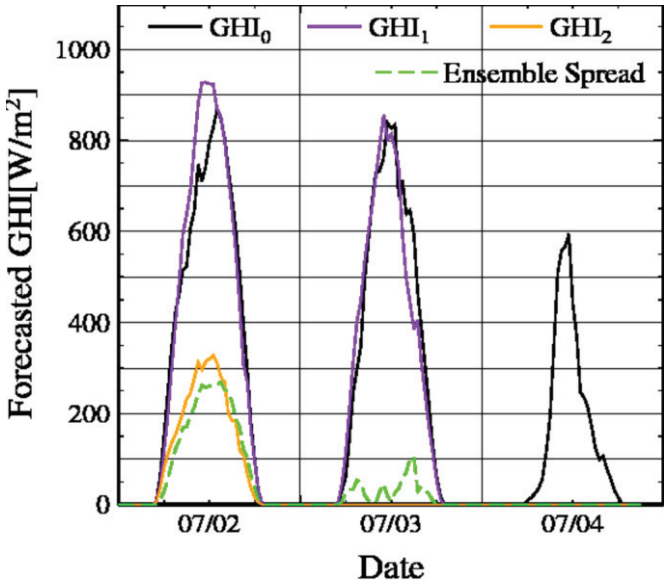

Fig. 5.2 An example of ensemble forecasting result of the solar irradiance (GHI) with WRF (Forecasted at July 2nd, 2013)

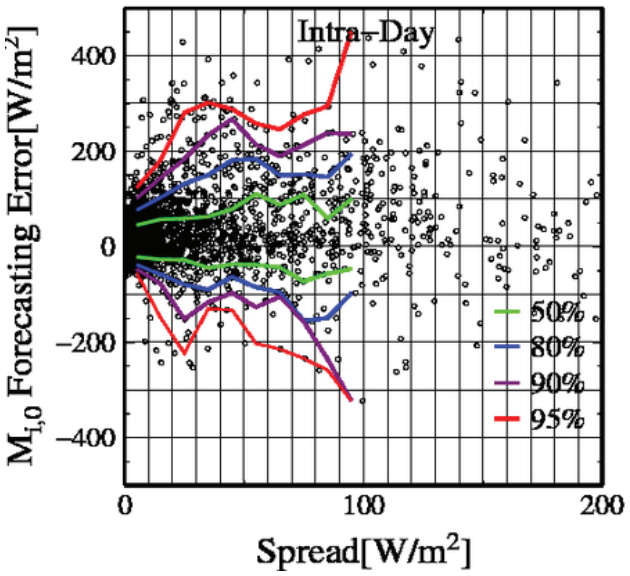

Fig. 5.3 Relationship of the ensemble spread of GHI and its forecasting error for the intra-day forecasting $M_{i,0}$ (61 observation-point average, from Sep 1st to Nov 30th, 2013)

5.2.5 Size of prediction interval of solar irradiance forecasting

Figure 5.4 shows schematic diagram of the size of the prediction interval of solar irradiance GHI. The area A_{Total} between the upper and the lower bound of prediction interval is defined as the size. Here gives a simple introduction about its calculation method. By splitting the region of the prediction interval up into small sub-regions, whose areas could be approximated by rectangles, the size of the prediction interval could be calculated as a limit of sums of rectangle areas. The size A_{Total} of the prediction interval of solar irradiance GHI is defined with Eq. (5.2).

$$A_{Total} \approx \frac{1}{2}[Upper(a) - Lower(a)]\Delta t + \sum_{i=1}^{2(b-a)-1}[Upper(a+i\Delta t) - Lower(a+i\Delta t)]\Delta t + \frac{1}{2}[Upper(b) - Lower(b)]\Delta t \tag{5.2}$$

Where $Upper(t)$ and $Lower(t)$ denote solar irradiance GHI of the upper bound and lower bound of prediction interval at t time, respectively, $a + i\Delta t$ is the $(i-1)^{th}$ time of valid sunshine time zone $[a,\ b]$ in a day. a is the time of sunrise, and b is the time of sunset every day. Since GHI values used for the verification are obtained by calculating mean values in 61 observation sites and with 30-minute interval, the time interval $\Delta t = 30\,\text{min}\ (\text{i.e.},\ 0.5\,\text{h})$.

Period average size (S_{Ave}) of the prediction interval of solar irradiance GHI is defined as follows:

$$S_{Ave} = \frac{\sum_{i=1}^{N_{Day}} A_{Total,i}}{\Delta T \times N_{Day}}, \quad \Delta T = b - a \tag{5.3}$$

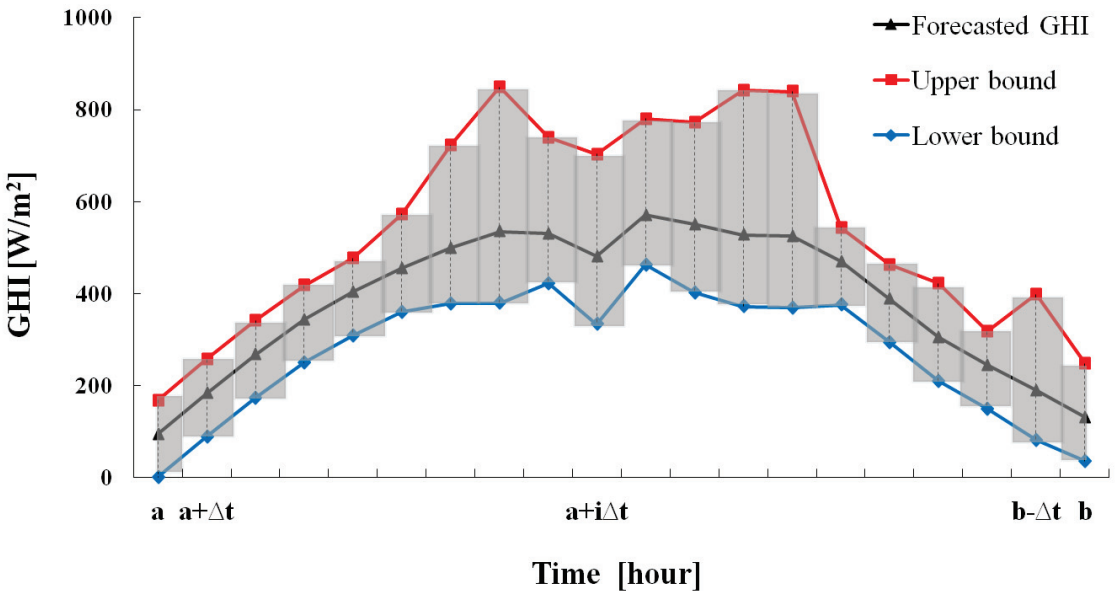

Fig. 5.4 Schematic diagram of the total size of the prediction interval of solar irradiance GHI. The black line with triangle shows the forecasted value; the red line with square represents the upper bound of the prediction interval; the blue line with diamond gives the lower bound of the prediction interval.

Where N_{Day} is the number of days during the verification period, $A_{Total,i}$ is the total size of the prediction interval of solar irradiance GHI on the i^{th} day.

5.2.6 Empirical coverage rate of prediction interval of solar irradiance forecasting

To take into consideration reliability of forecasted solar irradiance GHI, the empirical coverage rate of observed GHI within prediction interval is discussed in this section. The empirical coverage rate is expressed in the following Eq. (5.4).

$$\text{Empirical coverage rate} = \frac{n_{Actual}}{n_{Total}} \times 100 \ [\%] \tag{5.4}$$

Where n_{Actual} is the actual number of observation data fallen within the prediction interval, n_{Total} is the total number of data in the valid sunshine time zone.

5.3 Results and discussion

The ensemble forecasting of solar irradiance is performed every day, and the solar irradiance and its prediction interval are forecasted. The intra-day forecasting $M_{i,0}$ are connected and indicated as the time series from Dec 1st to 10th, 2013 in **Fig. 5.5**. More details that the results with WRF for ten days from 1st to 10th each month are given in the **Appendix Figure A.1** to **A.9**. The forecasted solar irradiance and the observed data are plotted with black solid lines and red dots respectively in the figure. The irradiance is forecasted larger than the observation because of the overestimation of WRF as explained before. The ensemble spread of the member $M_{i,0}$ is also indicated with a green dashed line in **Fig. 5.5 (a)**. The value of the spread changes in time; for example, the spread in Dec 6th is large, and the one in Dec 3rd is almost zero. As the ensemble spread becomes smaller, the forecasted solar irradiance (GHI) comes closer to the observed one.

The upper and lower bounds of the prediction interval are indicated with two blue dashed lines in **Fig. 5.5 (b) to (e)**. Their coverage rates are 50%, 80%, 90% and 95%, respectively. To evaluate the bounds of the intervals, the upper and lower bounds of the prediction interval in **Fig. 5.3** are evaluated from the given coverage rate and the spread in **Fig. 5.5 (a)** first. And they are plotted around the forecasted irradiance as the prediction interval. In this study, coverage rate of the prediction interval is called as nominal coverage rate. The size of the interval is small when the spread is small, like

Dec 3rd in the figure, and the interval size is large when the spread is large, like on Dec 6th.

When the nominal coverage rate is 50%, many observation data are out of the prediction interval as shown in **Fig. 5.5 (b)**, but most of observation data lie in the interval when the probability is increased to 95% in **Fig. 5.5 (e)**.

Figure 5.6 shows daily and 10-days mean sizes of prediction interval of the ensemble forecasting for the intra-day solar GHI forecasting $M_{i,0}$ for ten days from Dec 1st to 10th, 2013. Nominal coverage rates 50%, 80%, 90% and 95% are discussed respectively. As indicated in this figure, it is clear that the interval size becomes large as the nominal coverage rate becomes large.

Figure 5.7 shows correlation charts between daily and 10-days mean empirical coverage rates and the corresponding nominal coverage rates of the ensemble forecasting for the intra-day solar irradiance forecasting $M_{i,0}$ during the period from Dec 1st to 10th, 2013. As depicted in this figure, the daily empirical coverage rates are on the whole smaller than the corresponding nominal coverage rates, except on Dec 4th and Dec 10th. It could be probably due to the overestimation of the solar irradiance computed with WRF. Besides, for 10 days mean, the reductions of the empirical rates from the nominal rates 50%, 80%, 90% and 95% are about 0.31, 0.29, 0.26 and 0.21 of the nominal rates respectively, and not so large. These results indicate that the ensemble forecasting of the solar irradiance with the prediction interval works well.

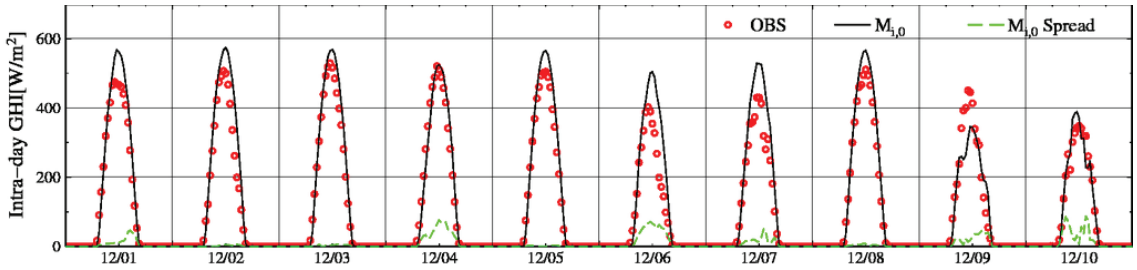

(a) $M_{i,0}$ and Spread

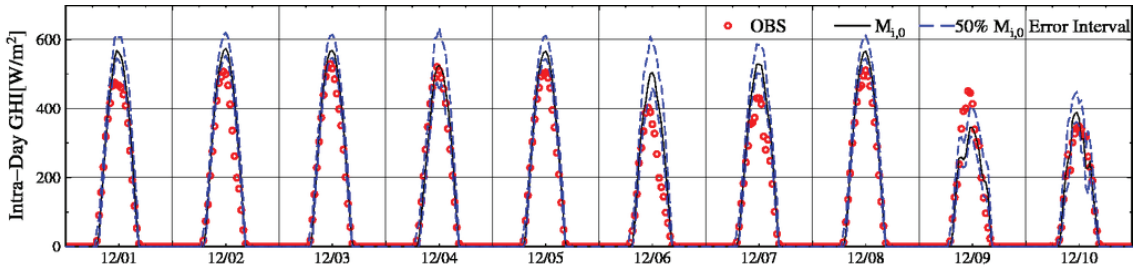

(b) $M_{i,0}$ and 50% prediction interval

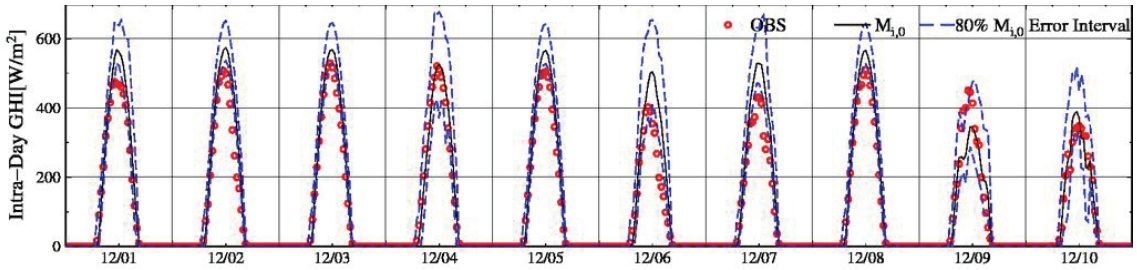

(c) $M_{i,0}$ and 80% prediction interval

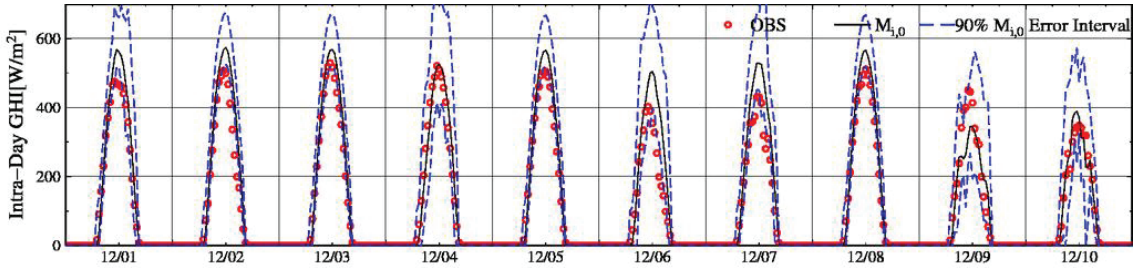

(d) $M_{i,0}$ and 90% prediction interval

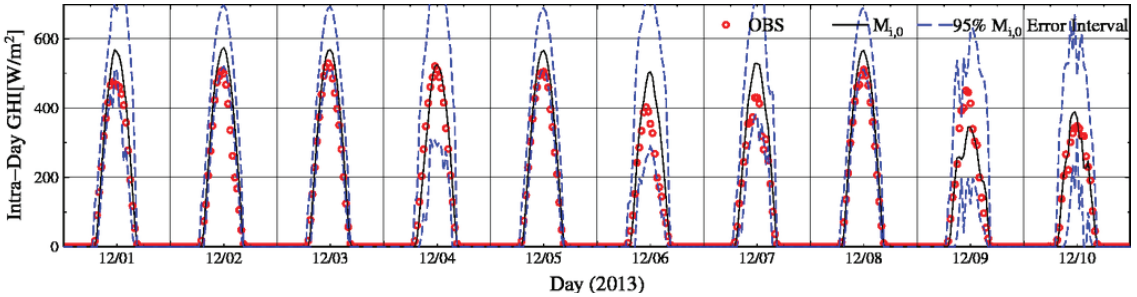

(e) $M_{i,0}$ and 95% prediction interval

Fig. 5.5 Time series of observed and forecasted solar irradiance (GHI) and its 50%, 80%, 90%, 95% prediction interval for the intra-day forecasting $M_{i,0}$ (61 observation-point average, from Dec 1st to 10th, 2013)

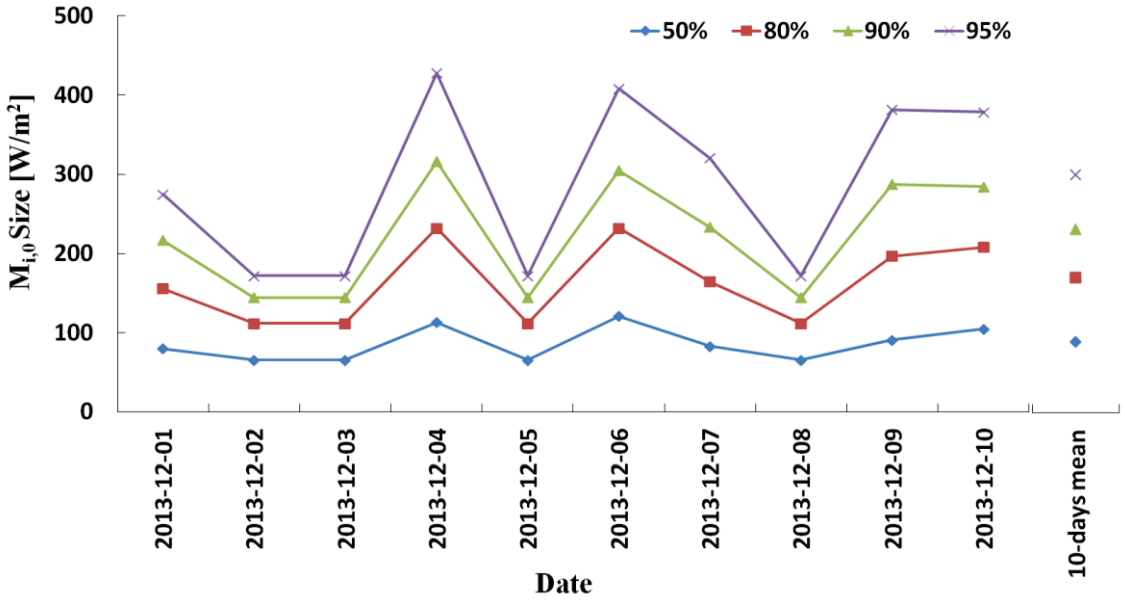

Fig. 5.6 Daily and 10-days mean sizes of prediction interval of the ensemble forecasting for the intra-day solar irradiance (GHI) forecasting $M_{i,0}$ with WRF (from Dec 1st to 10th, 2013)

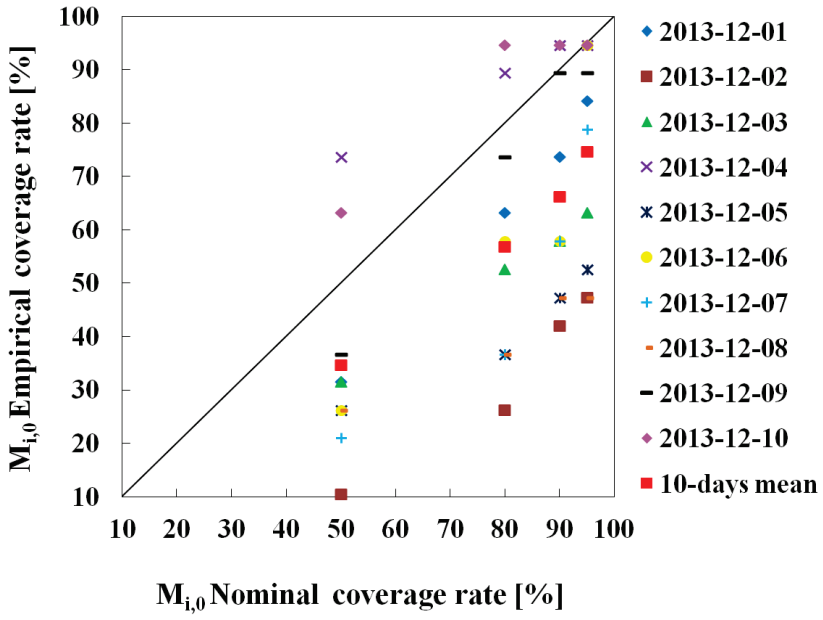

Fig. 5.7 Correlation chart between daily and 10-days mean empirical coverage rates and nominal coverage rates of the prediction interval of the ensemble forecasting for the intra-day solar irradiance (GHI) forecasting $M_{i,0}$ with WRF (from Dec 1st to 10th, 2013)

5.4 Summary

In order to gain an insight into the forecasting reliability of solar irradiance, the solar irradiance GHI ensemble forecasting system for 72-hour ahead forecasting is performed with the meteorological model WRF. One of the ensemble methods, the Lagged Averaged Forecast (LAF) method is employed here and the several forecasting results operated with different initial time are used as the ensemble members. The spread of the ensemble forecasting is calculated as a parameter corresponding to the unreliability of the forecasting, and the relation of the spread and the forecasting error is discussed to evaluate the prediction interval. The solar irradiance and its prediction interval are forecasted with the ensemble method. The size of the prediction interval changes as the reliability of the forecasting in the ensemble forecasting varies. The empirical coverage rates of the prediction interval are a little lower than the corresponding nominal ones in this ensemble. It might be considered by the effect of overestimation of the WRF computation.

Chapter 6 Increasing the accuracy of ensemble forecasting of solar irradiance by applying Kalman Filter

6.1 Introduction

In the chapter 3, the accuracy of solar GHI forecasting with WRF was discussed, and in the chapter 4, the accuracy of WRF-simulated GHI forecasting after applying the Kalman Filter was discussed. Compared with the statistical error indices (Bias, RMSE, CORR) from different forecasting methods summarized in **Table 4.8**, the magnitudes of biases are reduced evidently by applying the Kalman Filters as the post processor of the forecasting; for example, the bias of the intra-day forecasting $M_{i,0}$ changes from 49.7 W/m^2 to -2.4 W/m^2 with the univariate Kalman Filter. The biases of the forecasting with WRF and Kalman Filters are almost negligible compared with the averaged intensity of the solar irradiance. By the application of the Kalman Filters, not only the Biases but also the RMSEs reduce, and CORRs increase as shown in **Table 4.8**. The effect of the Kalman Filters to the forecasting accuracy is explained with the improvement of these error indices.

In addition, the time series of the correction coefficient a of the univariate Kalman Filter is illustrated in **Fig. 4.3**. The value of the coefficient is about 0.88 and less than one. This Kalman Filter reduces the intensity of the solar irradiance forecasted with WRF with the value of the coefficient, and corrects the overestimation of the WRF computation. Consequently, the accuracy of WRF-simulated solar GHI forecasting has been improved.

However, the empirical coverage rates of prediction interval of solar GHI

forecasting with WRF only are smaller than the corresponding nominal coverage rates in the previous chapter. The reductions of empirical coverage rates from the nominal ones are about 0.3 of the nominal coverage rates. Therefore, in order to recover the reductions of the empirical coverage rates, the solar GHI ensemble forecasting with WRF and Kalman Filter is investigated in this chapter.

6.2 Ensemble forecasting of solar irradiance with Kalman Filter

Daily ensemble forecasting of the solar irradiance is conducted with the meteorological model WRF, as in the previous chapter, except the adaptation of Kalman Filter as the post processor of the WRF. The detail process of the ensemble forecasting has been explained in the section 5.2.2.

6.2.1 Solar irradiance for ensemble forecasting with univariate Kalman Filter

In the chapter 5, the ensemble mean is calculated as an average of the members for the same target day, e.g. the three members, $M_{i,0}$, $M_{i-1,1}$, $M_{i-2,2}$ for the intra-day forecasting in the operation day i. The label "$M_{i,j}$" indicate the forecasted irradiance with WRF only in the chapter 5. In this section, the author indicates the WRF-simulated result adjusted with univariate Kalman Filter with "$M_{i,j}-KF$".

The accuracy of the forecasted solar irradiance has been discussed in the previous chapter, and the results are shown in **Fig. 4.6** and **Table 4.6**. The statistical error indices of the intra-day forecasting are better than the ones of the other forecasting including the ensemble mean. Usually the ensemble mean "Ensemble Mean$-KF$" is employed as the forecasted value in the ensemble forecasting methods. However the intra-day forecasting with WRF and univariate Kalman Filter "$M_{i,0}-KF$" is applied as the

forecasted value in this chapter, because the accuracy of the intra-day forecasting is the highest among them in this figure and this table.

Figure 6.1 shows the relationship between the spread of the intra-day forecasting with WRF and univariate Kalman Filter and its forecasting error from the observation during the period from Sep 1st to Nov 30th, 2013. The upper and lower bounds of the forecasting error interval with the coverage rates 50%, 80%, 90% and 95% are also drawn with lines in this figure. These lines are evaluated within every 10 W/m^2 in the spread, and also evaluated positive and negative errors separately. The plotted data converge around the origin of the graph, and the forecasting error diverges widely as the spread becomes large as indicated with the bound lines of the intervals.

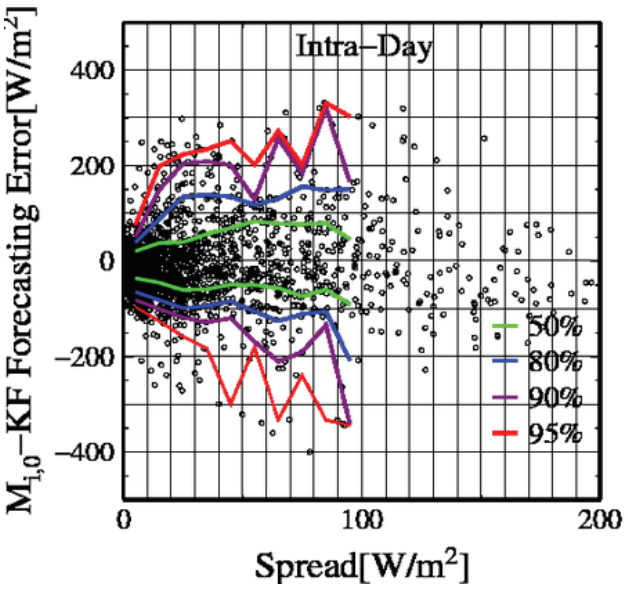

Fig. 6.1 Relationship of the ensemble spread of the solar irradiance (GHI) and its forecasting error for the intra-day forecasting with WRF and univariate Kalman Filter $M_{i,0} - KF$ (61 observation-point average, from Sep 1st to Nov 30th, 2013)

The bound lines of the forecasting error interval aren't smooth, because the number of ensemble members are limited, only 3, and the spread may contain random error. It causes the limitation of the computational environment in this work. Increasing of ensemble members may contribute for the improvement of the interval estimation.

The plots and the bound lines distribute almost symmetrically with respect to the horizontal axis. It's caused that the univariate Kalman Filter improves the overestimation of the WRF computation.

6.2.2 Solar irradiance for ensemble forecasting with multivariate Kalman Filter

The author indicates the forecasted solar irradiance adjusted with multivariate Kalman Filter with " $M_{i,j} - mvKF$ ". The intra-day forecasting with WRF and multivariate Kalman Filter "$M_{i,0} - mvKF$" is applied as the forecasted value in this chapter, because the accuracy of the intra-day forecasting is the highest.

Figure 6.2 shows the relationship between the spread of the intra-day forecasting with WRF and multivariate Kalman Filter and its forecasting error from the observation during the period from Sep 1st to Nov 30th, 2013. The plots and the bound lines, except the lines with the coverage rate 95%, distribute almost symmetrically with respect to the horizontal axis. It is also found that the multivariate Kalman Filter improves the overestimation of the WRF computation.

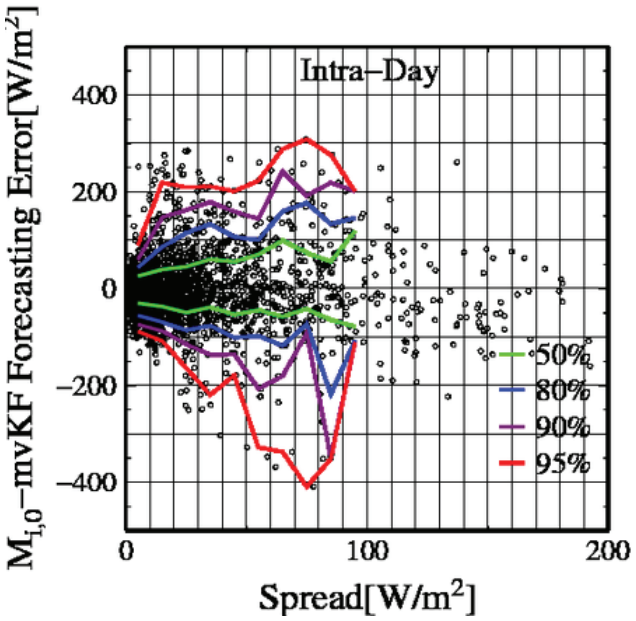

Fig. 6.2 Relationship of the ensemble spread of the solar irradiance (GHI) and its forecasting error for the intra-day forecasting with WRF and multivariate Kalman Filter $M_{i,0} - mvKF$ (61 observation-point average, from Sep 1st to Nov 30th, 2013)

6.3 Solar irradiance forecasting with prediction interval using Kalman Filter

In the previous chapter, the ensemble forecasting of solar irradiance with WRF is performed. In this section, the solar irradiance with WRF and Kalman Filter, and its prediction interval are discussed. **Figure 6.3** shows the solar irradiance GHI forecasted with WRF and univariate Kalman Filter, and **Fig. 6.4** shows the one with WRF and multivariate Kalman Filter. In these figures, the computed results of the intra-day forecasting $M_{i,0} - KF$ and $M_{i,0} - mvKF$ are connected and indicated as the time series from Dec 1st to 10th, 2013. The forecasted solar irradiance and the observed data are plotted with black solid lines and red dots respectively in these figures. As

mentioned in the chapter 5, the irradiance forecasted with WRF only is larger than the observed one in **Fig. 5.5** because of the overestimation of WRF. The forecasted irradiance with WRF and Kalman Filters seem well close to the observed one as shown in **Fig. 6.3** and **Fig. 6.4**.

The ensemble spread of the members $M_{i,0} - KF$ with WRF and univariate Kalman Filter, and $M_{i,0} - mvKF$ with WRF and multivariate Kalman Filter are also indicated with green dashed lines in **Fig. 6.3 (a)** and **Fig. 6.4 (a)**. The value of the spread changes in time; for example, the spread on Dec 6th is large, and the one on Dec 3rd is almost zero, in these figures.

The upper and lower bounds of the prediction interval are indicated with two blue dashed lines in **Fig. 6.3 (b) to (e)** and **Fig. 6.4 (b) to (e)**. Their nominal coverage rates are 50%, 80%, 90% and 95%, respectively. For better understanding of the forecasting reliability, the upper and lower bounds of the prediction interval in **Fig. 6.1** or **Fig. 6.2** are evaluated from the given nominal coverage rate and the spread in **Fig. 6.3 (a)** or **Fig. 6.4 (a)** first. And they are plotted around the forecasted irradiance as the prediction interval. The size of the interval is small when the spread is small, like Dec 3rd in these figures, and the interval size is large when the spread is large, like on Dec 6th. The nominal coverage rate becomes large proportionally to the interval size, as shown in these figures.

Table 6.1 summarizes daily sizes of the prediction interval of the ensemble forecasting for the intra-day solar GHI forecasting from different forecasting methods for ten days from Dec 1st to 10th, 2013. The data of the night time are rejected for the calculation of the size. As displayed in this table, the daily sizes become large as the

nominal coverage rates become large on the whole. The sizes of the ensemble forecasting with WRF and Kalman Filters are small compared with the one forecasted with WRF only.

Table 6.2 summarizes daily empirical coverage rates of the ensemble forecasting for the intra-day solar GHI forecasting from different forecasting methods for ten days from Dec 1st to 10th, 2013. They are the ratio of the number of the observation data lied in the prediction interval of the intra-day forecasting $M_{i,0}$ with WRF only, $M_{i,0}-KF$ with WRF and univariate Kalman Filter, and $M_{i,0}-mvKF$ with WRF and multivariate Kalman Filter. The data of the night time are rejected for the calculation of the rates. Overall, the daily empirical coverage rates become large as the nominal ones become large as found in this table. The daily empirical coverage rates of the forecasting with WRF only are smaller than the nominal ones, but the daily empirical ones of the forecasting with WRF and univariate Kalman Filter increase their values and close well to the nominal ones.

Figure 6.5 shows 10-days mean sizes of prediction interval of the ensemble forecasting for the intra-day solar irradiance forecasting $M_{i,0}$, $M_{i,0}-KF$ and $M_{i,0}-mvKF$ for ten days from Dec 1st to 10th, 2013. Regarding it as a whole, for individual forecasting method, the 10-days mean size will become large proportionally to the nominal coverage rate as found in this figure. Moreover, by the application of Kalman Filters to improve the solar irradiance forecasting, the interval sizes become small. For the multivariate Kalman Filter, the 10 days mean sizes of nominal coverage rates 50%, 80%, 90% and 95% are narrowed about 15.2%, 14.8%, 9.5% and 5.8% of the ones of solar GHI forecasting $M_{i,0}$, respectively.

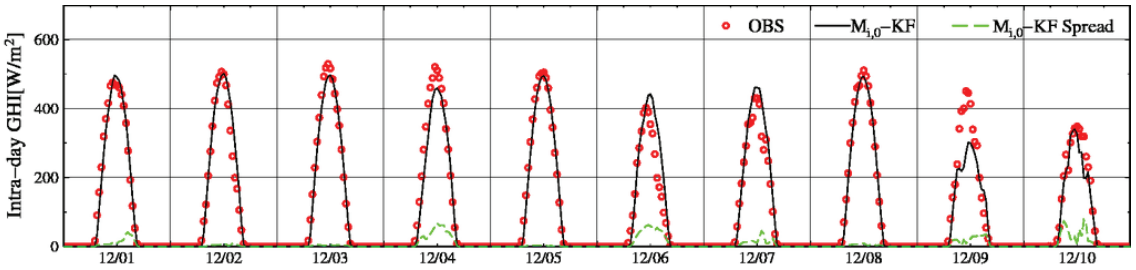

(a) $M_{i,0}-KF$ and Spread

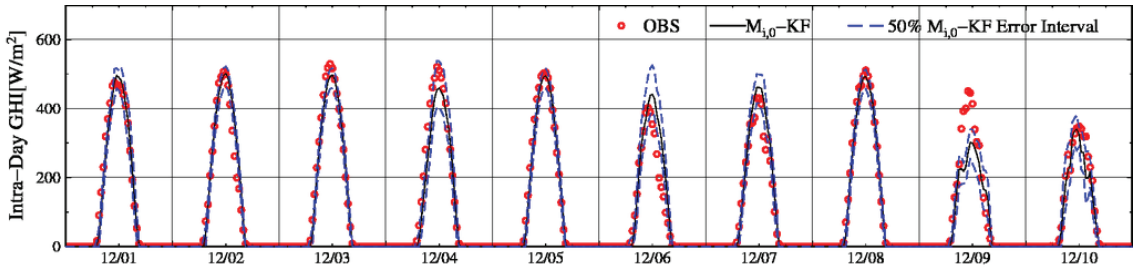

(b) $M_{i,0}-KF$ and 50% prediction interval

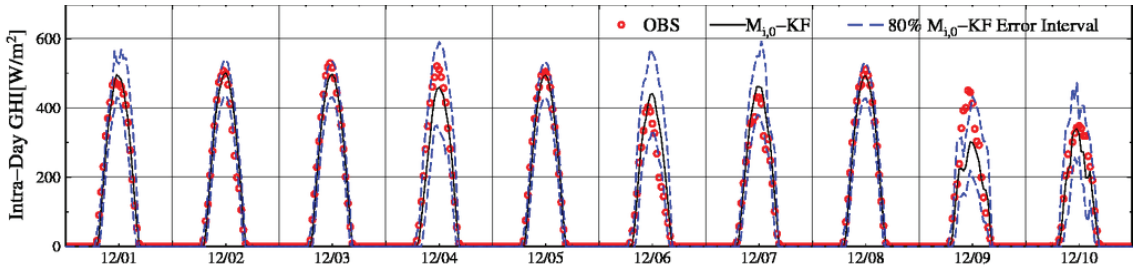

(c) $M_{i,0}-KF$ and 80% prediction interval

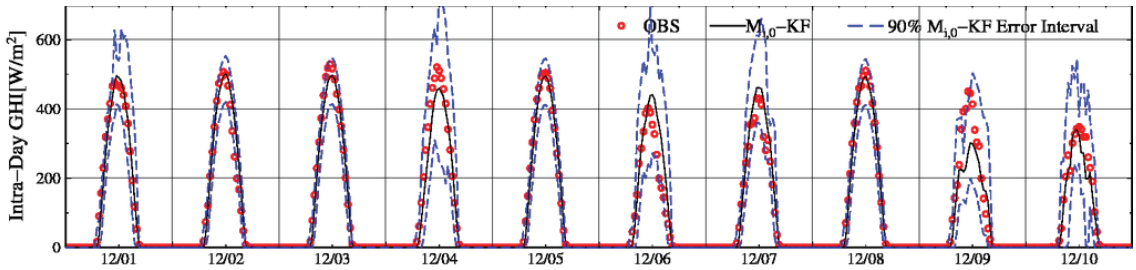

(d) $M_{i,0}-KF$ and 90% prediction interval

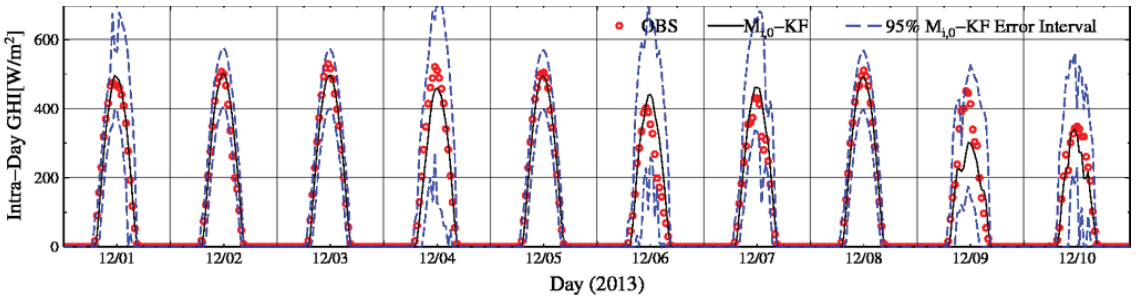

(e) $M_{i,0}-KF$ and 95% prediction interval

Fig. 6.3 Time series of observed and forecasted solar irradiance (GHI) and its 50%, 80%, 90%, 95% prediction interval for the intra-day forecasting $M_{i,0}-KF$ (61 observation-point average, from Dec 1st to 10th, 2013)

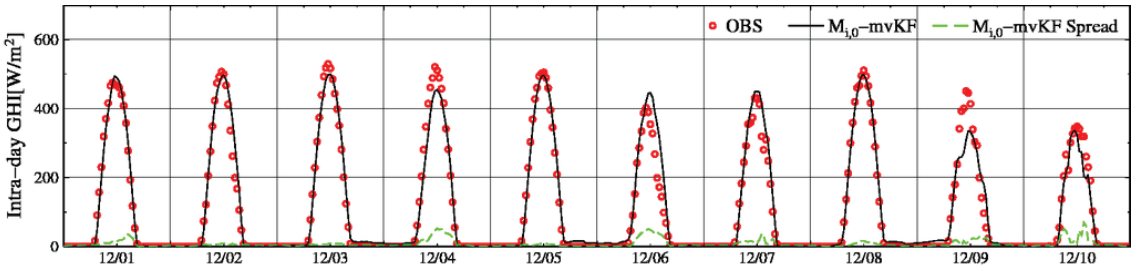

(a) $M_{i,0}-mvKF$ and Spread

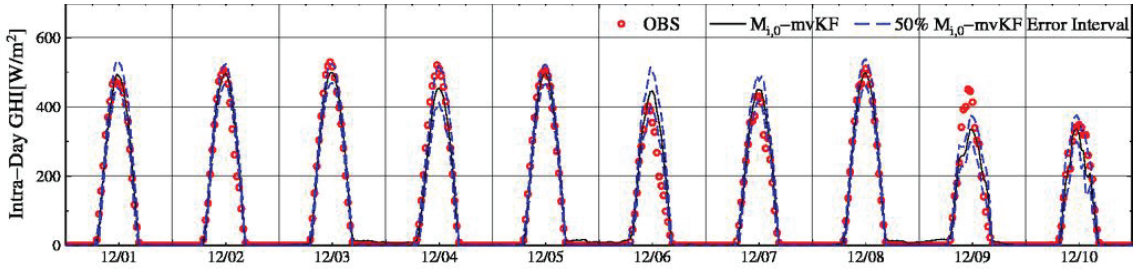

(b) $M_{i,0}-mvKF$ and 50% prediction interval

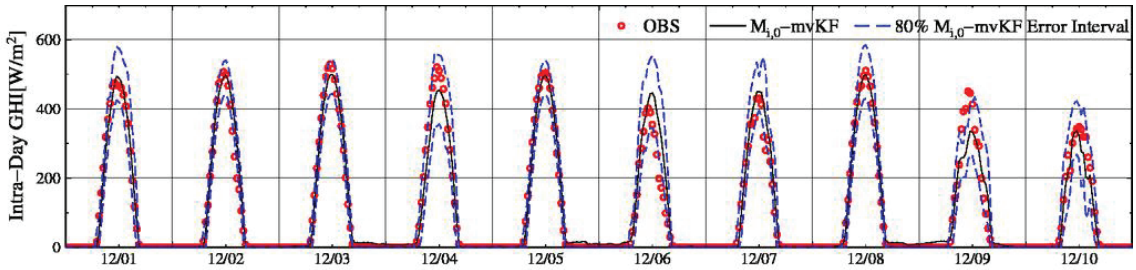

(c) $M_{i,0}-mvKF$ and 80% prediction interval

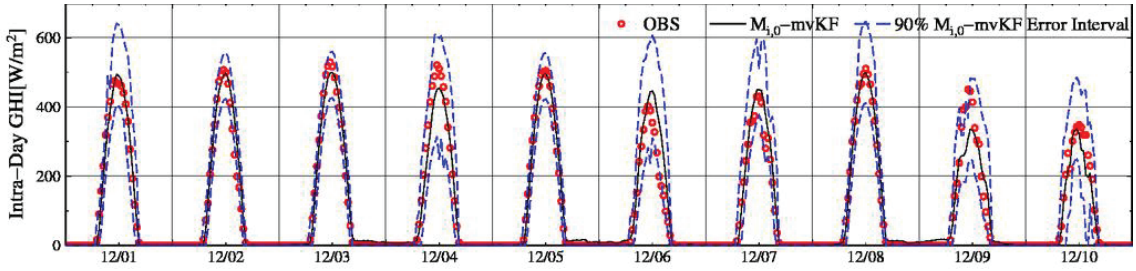

(d) $M_{i,0}-mvKF$ and 90% prediction interval

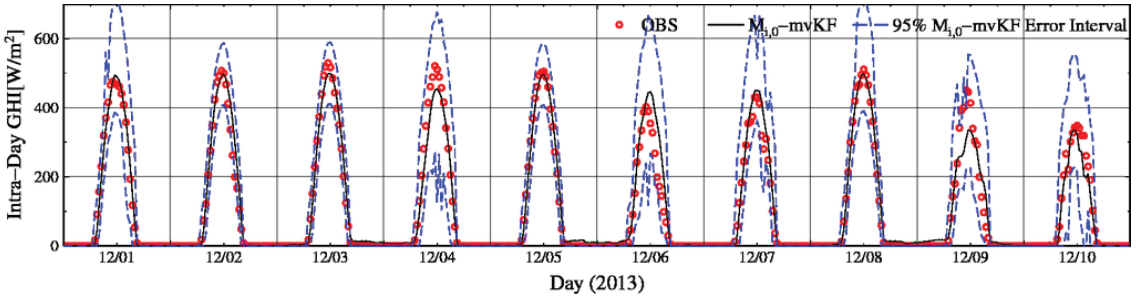

(e) $M_{i,0}-mvKF$ and 95% prediction interval

Fig. 6.4 Time series of observed and forecasted solar irradiance (GHI) and its 50%, 80%, 90%, 95% prediction interval for the intra-day forecasting $M_{i,0}-mvKF$ (61 observation-point average, from Dec 1st to 10th, 2013)

Table 6.1 Daily sizes of the prediction interval of the ensemble forecasting for the intra-day solar irradiance (GHI) forecasting. $M_{i,0}$ is a member forecasted with WRF only, and $M_{i,0}-KF$ is with WRF and univariate Kalman Filter, and $M_{i,0}-mvKF$ is with WRF and multivariate Kalman Filter (from Dec 1st to 10th, 2013)

Nominal coverage rate of prediction interval	Forecasting method	Size of prediction interval [W/m²]									
		12/01	12/02	12/03	12/04	12/05	12/06	12/07	12/08	12/09	12/10
50%	$M_{i,0}$	79.9	65.4	65.4	112.9	65.4	120.9	82.9	65.4	90.8	104.7
	$M_{i,0}-KF$	76.7	55.0	55.0	107.9	54.9	109.7	78.3	54.9	91.6	98.9
	$M_{i,0}-mvKF$	74.6	54.8	54.8	90.4	54.8	91.0	74.0	63.6	77.3	88.9
80%	$M_{i,0}$	155.6	111.8	111.8	231.9	111.8	232.1	164.5	111.7	196.7	208.0
	$M_{i,0}-KF$	147.2	99.6	99.6	212.2	99.5	196.9	155.8	99.4	188.4	190.6
	$M_{i,0}-mvKF$	149.6	95.9	96.0	179.5	95.9	179.6	148.4	120.6	156.9	171.4
90%	$M_{i,0}$	217.0	144.5	144.5	316.4	144.4	304.6	233.3	144.3	287.1	284.4
	$M_{i,0}-KF$	208.6	127.1	126.9	328.0	126.9	290.3	223.1	126.8	272.8	279.0
	$M_{i,0}-mvKF$	217.1	129.0	129.3	269.5	129.1	262.3	220.2	174.2	223.2	257.0
95%	$M_{i,0}$	274.8	171.9	171.9	427.6	171.8	408.2	320.7	171.8	381.3	378.4
	$M_{i,0}-KF$	266.8	163.5	163.3	431.1	163.3	398.9	288.6	163.2	328.8	338.1
	$M_{i,0}-mvKF$	295.4	171.1	172.1	371.1	171.6	354.9	301.2	238.0	302.5	334.1

Table 6.2 Daily empirical coverage rates of the prediction interval of the ensemble forecasting for the intra-day solar irradiance (GHI) forecasting. $M_{i,0}$ is a member forecasted with WRF only, and $M_{i,0}-KF$ is with WRF and univariate Kalman Filter, and $M_{i,0}-mvKF$ is with WRF and multivariate Kalman Filter (from Dec 1st to 10th, 2013)

Nominal coverage rate of prediction interval	Forecasting method	Empirical coverage rate of prediction interval [%]									
		12/01	12/02	12/03	12/04	12/05	12/06	12/07	12/08	12/09	12/10
50%	$M_{i,0}$	31.6	10.5	31.6	73.7	26.3	26.3	21.1	26.3	36.8	63.2
	$M_{i,0}-KF$	57.9	52.6	42.1	57.9	57.9	47.4	63.1	57.9	36.8	68.4
	$M_{i,0}-mvKF$	73.7	52.6	47.4	57.9	47.4	47.4	68.4	84.2	42.1	78.9
80%	$M_{i,0}$	63.2	26.3	52.6	89.5	36.8	57.9	36.8	36.8	73.7	94.7
	$M_{i,0}-KF$	73.7	78.9	78.9	89.5	84.2	68.4	84.2	89.5	63.1	94.7
	$M_{i,0}-mvKF$	84.2	73.7	94.7	89.5	94.7	63.2	84.2	94.7	63.2	94.7
90%	$M_{i,0}$	73.7	42.1	57.9	94.7	47.4	57.9	57.9	47.4	89.5	94.7
	$M_{i,0}-KF$	84.2	78.9	94.7	94.7	94.7	89.5	94.7	94.7	78.9	94.7
	$M_{i,0}-mvKF$	94.7	78.9	94.7	94.7	94.7	84.2	94.7	94.7	78.9	94.7
95%	$M_{i,0}$	84.2	47.4	63.2	94.7	52.6	94.7	78.9	47.4	89.5	94.7
	$M_{i,0}-KF$	94.7	84.2	94.7	94.7	94.7	94.7	94.7	94.7	89.5	94.7
	$M_{i,0}-mvKF$	94.7	84.2	94.7	94.7	94.7	94.7	94.7	94.7	84.2	94.7

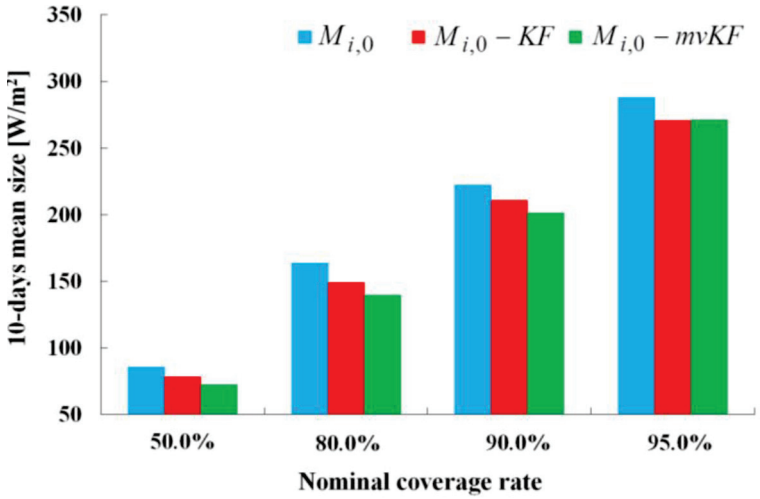

Fig. 6.5 10-days mean sizes of prediction interval for the intra-day solar irradiance (GHI) forecasting $M_{i,0}$ with WRF only, and $M_{i,0} - KF$ with WRF and univariate Kalman Filter, and $M_{i,0} - mvKF$ with WRF and multivariate Kalman Filter (for ten days from Dec 1st to 10th, 2013)

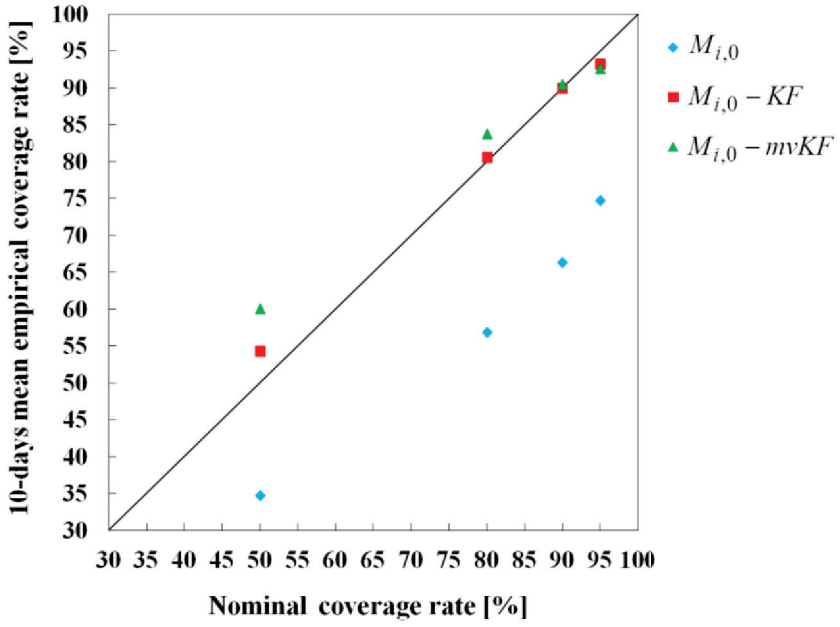

Fig. 6.6 Correlation chart between 10-days mean empirical coverage rates and nominal coverage rates of the prediction interval of the ensemble forecasting for the intra-day solar irradiance (GHI) forecasting $M_{i,0}$ with WRF only, and $M_{i,0} - KF$ with WRF and univariate Kalman Filter, and $M_{i,0} - mvKF$ with WRF and multivariate Kalman Filter (for ten days from Dec 1st to 10th, 2013)

Figure 6.6 shows correlation charts between10-days mean empirical coverage rates and the corresponding nominal coverage rates of the ensemble forecasting for the intra-day solar irradiance forecasting $M_{i,0}$, $M_{i,0}-KF$ and $M_{i,0}-mvKF$ for ten days from Dec 1st to 10th, 2013. As shown in this figure, the 10-days mean empirical coverage rates will become large proportionally to the nominal one on the whole. With respect to the reductions of 10-days mean empirical rates from the nominal ones, $M_{i,0}$ forecasting with WRF only is the largest, and $M_{i,0}-KF$ forecasting with WRF and univariate Kalman Filter is the smallest. For nominal coverage rates 50%, the reduction ranges from 0.31 to -0.08. For nominal coverage rate 80%, the reduction ranges from 0.29 to -0.006. For nominal coverage rate 90%, the reduction ranges from 0.26 to 0.001. For nominal coverage rate 95%, the reduction ranges from 0.21 to 0.02. These results suggest that the 10-days mean empirical coverage rates of $M_{i,0}-KF$ forecasting could well approach the nominal ones.

Furthermore, monthly prediction interval sizes and monthly empirical coverage rates of the ensemble forecasting for the intra-day solar irradiance forecasting from different forecasting methods during the period from October 2013 to June 2014 are listed in **Tables 6.3** and **6.4**.

Figure 6.7 shows period average sizes of prediction interval of the ensemble forecasting for the intra-day solar irradiance forecasting $M_{i,0}$, $M_{i,0}-KF$ and $M_{i,0}-mvKF$ during the period from October 2013 to June 2014. In terms of single forecasting method, the period average size will become large as the nominal coverage rate becomes large as showed in this figure. Through applying the Kalman Filter to the ensemble forecasting, the interval sizes become small. Because of the use of

multivariate Kalman Filter, the period average sizes of nominal coverage rates 50%, 80%, 90% and 95% are narrowed about 16.8%, 13.2%, 10.9% and 5.7% of the ones of solar GHI forecasting $M_{i,0}$, respectively.

Figure 6.8 shows correlation charts between period average empirical coverage rates and the corresponding nominal coverage rates of the ensemble forecasting for the intra-day solar irradiance forecasting $M_{i,0}$, $M_{i,0}-KF$ and $M_{i,0}-mvKF$ during the period from October 2013 to June 2014. Overall, the period average empirical coverage rate will become large proportionally to the nominal one as depicted in **Fig. 6.8**. Besides, for these two Kalman Filters, distinct differences are not found. However, it should be noted that the period average empirical coverage rates of the forecasting with WRF and multivariate Kalman Filter could well approach the nominal ones.In terms of the reductions of period average empirical rates from the nominal ones, $M_{i,0}$ forecasting with WRF only is the largest, and $M_{i,0}-mvKF$ forecasting with WRF and multivariate Kalman Filter is the smallest. For nominal coverage rates 50%, the reduction ranges from 0.10 to -0.02. For nominal coverage rate 80%, the reduction ranges from 0.21 to 0.03. For nominal coverage rate 90%, the reduction ranges from 0.20 to 0.04. For nominal coverage rate 95%, the reduction ranges from 0.19 to 0.03.

Consequently, the multivariate Kalman Filter is employed into the solar irradiance forecasting to improve the WRF computation. By applying it to the ensemble forecasting, the sizes of the prediction interval become small, and the empirical coverage rates increase and approach the nominal ones. This result indicates that the improvement of the forecasting gives a better estimation of the prediction interval.

Table 6.3 Monthly prediction interval sizes of the ensemble forecasting for the intra-day solar irradiance (GHI) forecasting. $M_{i,0}$ is a member forecasted with WRF only, and $M_{i,0}-KF$ is with WRF and univariate Kalman Filter, and $M_{i,0}-mvKF$ is with WRF and multivariate Kalman Filter (from October 2013 to June 2014)

Nominal coverage rate of prediction interval	Forecasting method	Size of prediction interval [W/m²]								
		Oct-13	Nov-13	Dec-13	Jan-14	Feb-14	Mar-14	Apr-14	May-14	Jun-14
50%	$M_{i,0}$	125.8	95.5	84.3	84.1	82.4	82.0	104.2	101.3	116.4
	$M_{i,0}-KF$	103.0	80.2	77.0	73.4	70.6	73.9	97.5	90.1	103.6
	$M_{i,0}-mvKF$	101.7	80.2	64.9	66.1	64.5	70.4	90.1	89.7	101.5
80%	$M_{i,0}$	256.8	181.7	162.1	156.3	140.4	146.7	163.2	172.7	197.3
	$M_{i,0}-KF$	221.7	161.6	148.5	141.5	125.1	130.2	161.2	162.6	183.4
	$M_{i,0}-mvKF$	194.8	155.9	138.5	129.2	118.2	129.8	152.3	164.8	185.1
90%	$M_{i,0}$	324.3	256.1	222.3	216.8	179.0	174.0	210.2	224.0	256.8
	$M_{i,0}-KF$	307.4	220.2	207.3	194.0	167.5	159.9	206.2	218.8	240.9
	$M_{i,0}-mvKF$	271.4	218.3	197.7	182.0	160.2	160.5	199.4	201.8	247.2
95%	$M_{i,0}$	364.4	323.2	284.4	282.6	214.1	207.4	244.1	296.4	293.1
	$M_{i,0}-KF$	373.3	281.7	263.7	250.9	218.7	195.2	242.4	288.9	287.9
	$M_{i,0}-mvKF$	345.2	287.9	263.9	254.6	213.1	193.0	239.8	276.3	294.1

Table 6.4 Monthly empirical coverage rates of the prediction interval of the ensemble forecasting for the intra-day solar irradiance (GHI) forecasting. $M_{i,0}$ is a member forecasted with WRF only, and $M_{i,0}-KF$ is with WRF and univariate Kalman Filter, and $M_{i,0}-mvKF$ is with WRF and multivariate Kalman Filter (from October 2013 to June 2014)

Nominal coverage rate of prediction interval	Forecasting method	Empirical coverage rate of prediction interval [%]								
		Oct-13	Nov-13	Dec-13	Jan-14	Feb-14	Mar-14	Apr-14	May-14	Jun-14
50%	$M_{i,0}$	50.1	47.2	48.7	50.3	52.5	36.7	43.6	32.1	42.0
	$M_{i,0}-KF$	41.3	49.7	59.9	43.6	43.7	49.1	53.8	48.9	53.4
	$M_{i,0}-mvKF$	45.0	55.7	65.5	55.4	43.7	45.9	51.0	45.3	50.5
80%	$M_{i,0}$	67.9	63.2	69.8	74.5	68.7	59.5	58.8	50.3	57.5
	$M_{i,0}-KF$	76.0	76.7	85.1	80.5	69.2	74.3	76.2	77.4	77.3
	$M_{i,0}-mvKF$	75.1	81.2	89.1	84.2	73.8	73.8	72.6	72.6	78.9
90%	$M_{i,0}$	71.6	75.8	77.9	83.6	79.4	69.3	64.5	58.9	68.0
	$M_{i,0}-KF$	86.9	88.3	93.5	90.6	84.4	83.2	83.8	90.1	87.7
	$M_{i,0}-mvKF$	86.8	89.5	94.4	91.8	84.7	82.5	82.2	81.2	88.1
95%	$M_{i,0}$	67.0	80.0	84.9	88.5	83.0	79.1	66.8	70.1	69.2
	$M_{i,0}-KF$	93.1	93.7	94.9	97.3	89.5	87.2	86.8	95.0	91.6
	$M_{i,0}-mvKF$	93.2	93.0	95.2	96.3	90.5	86.7	86.4	90.4	93.5

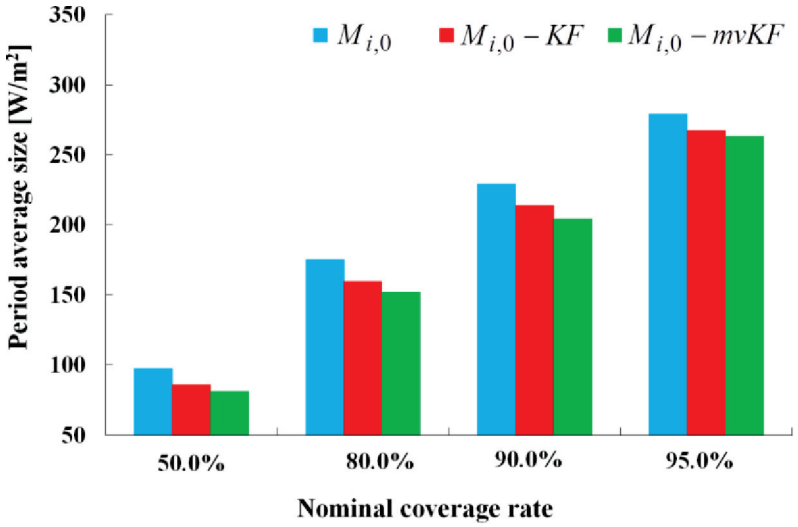

Fig. 6.7 Period average sizes of prediction interval for the intra-day solar irradiance (GHI) forecasting $M_{i,0}$ with WRF only, and $M_{i,0}-KF$ with WRF and univariate Kalman Filter, and $M_{i,0}-mvKF$ with WRF and multivariate Kalman Filter (from October 2013 to June 2014)

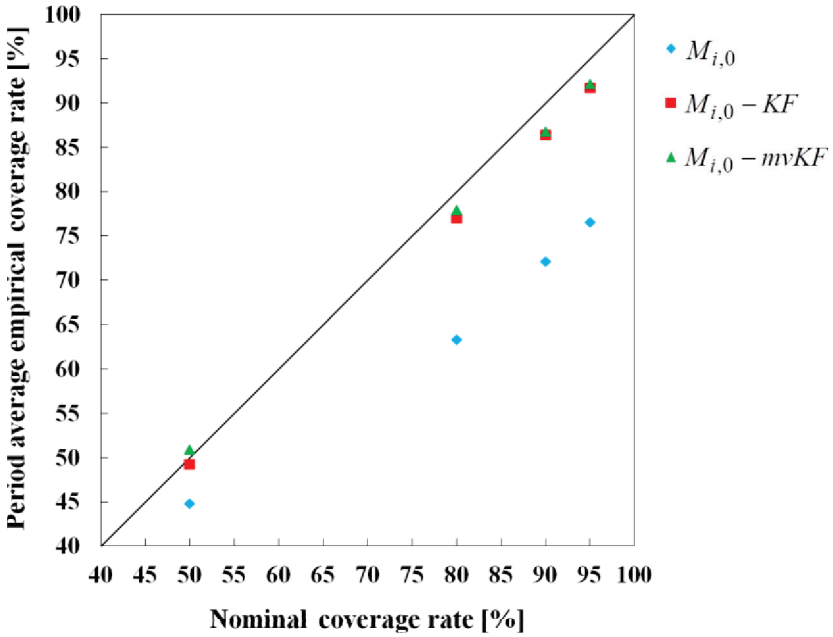

Fig. 6.8 Correlation chart between period average empirical coverage rates and nominal coverage rates of the prediction interval of the ensemble forecasting for the intra-day solar irradiance (GHI) forecasting $M_{i,0}$ with WRF only, and $M_{i,0}-KF$ with WRF and univariate Kalman Filter, and $M_{i,0}-mvKF$ with WRF and multivariate Kalman Filter (from October 2013 to June 2014)

6.4 Summary

In this chapter, for the purpose of increasing the forecasting accuracy of the prediction interval, Kalman Filter bias correction methods were applied to the solar irradiance GHI ensemble forecasting system for 72-hour ahead forecasting with the meteorological model WRF. The forecasting results with the univariate Kalman Filter and multivariate Kalman Filter were investigated separately. As a result, through the application of Kalman Filters as the post processor of the forecasting, the sizes of the prediction intervals reduce, and the empirical coverage rates increase and approach well to the nominal coverage rates. Based on the results obtained from this study, it could be concluded that the improvement by applying the Kalman Filters is not only for the forecasting itself, but also for the prediction interval estimation in the ensemble forecasting.

Chapter 7　Conclusion

Solar irradiance is the most important meteorological factor that affects solar power production. The reliable forecasting information of solar irradiance is urgently required by the grid operators for better management of the electrical power balance between demand and generation. Probabilistic forecasting of solar irradiance using the mesoscale meteorological model WRF (Weather Research and Forecasting) model was investigated in this thesis. To achieve this purpose, the thesis was carried out by four parts for investigation of : (1) solar irradiance forecasting by applying a meteorological model, (2) increasing the accuracy of solar irradiance forecasting by applying Kalman Filter, (3) ensemble forecasting of solar irradiance using WRF, and (4) increasing the accuracy of ensemble forecasting of solar irradiance by applying Kalman Filter. General conclusions obtained in each chapter are summarized as follows.

In Chapter 1, the background and objective of this dissertation were stated.

In Chapter 2, the on-situ observations in the central region of Japan were illustrated. The observations analyzed in this chapter are able to be used not only for the verification of the accuracy and characteristics of solar irradiance simulated by WRF, but also for the examination of solar irradiance forecasting reliability in the following chapters in this study.

In Chapter 3, firstly, a description of the WRF model, in particular about its governing equations and physical options, was stated. Secondly, the accuracy and characteristics of solar irradiance (Global Horizontal Irradiance, GHI) simulated by WRF were examined using on-situ observations in the central Japan. The WRF simulation on a 2km resolution grid was performed, and thus the solar irradiance GHI

forecasting for 72-hour ahead forecasting was obtained. In order to verify its forecasting accuracy, the three statistical indices of bias, root mean square error (RMSE) and correlation coefficient (CORR) were calculated. As a result, the intra-day solar GHI forecasting simulated by WRF was found to have a notable positive bias of more than +29% of the observed solar GHI and a RMSE of 60%. The positive bias in the WRF solar GHI is likely caused by the effect of atmospheric turbidity, which is not taken into account in the WRF model, and the actual atmosphere contains more cloud cover than the simulated results. Moreover, the persistent model was introduced for reference. The RMSE and CORR of the WRF forecasting result was better than that obtained by the persistent model. This indicated the validity of the forecasting with WRF.

In Chapter 4, in order to increase the accuracy of WRF-simulated GHI forecasting, statistical post-processing approaches Kalman Filters were applied. The results indicated that the use of Kalman Filters was a reasonable methodology to improve the accuracy. The accuracy of the WRF-simulated GHI for the intra-day forecasting after applying univariate linear Kalman Filter was finally reduced to have a bias of -2.4 W/m^2 and RMSE of 79.1 W/m^2. Due to the application of multivariate linear Kalman Filter, the bias on average of WRF-simulated GHI for the intra-day forecasting is removed around 99.5%, and RMSE is improved around 25%. Furthermore, the CORR with WRF and Kalman Filter was also slightly increased compared to the one with WRF only.

In Chapter 5, in order to gain an insight into the forecasting reliability of solar irradiance, ensemble forecasting method was applied for assessing the prediction interval of the solar irradiance forecasting. The Lagged Averaged Forecast (LAF) method was employed to create the ensemble member in this analysis. The spread of the ensemble forecasting was calculated as a parameter corresponding to the

unreliability of the forecasting, and the relation of the spread and the forecasting error was discussed to evaluate the prediction interval. As a result, the size of the prediction interval changes as the reliability of the forecasting in the ensemble forecasting varies. The empirical coverage rates of the prediction interval are a little lower than the corresponding nominal ones in this ensemble.

In Chapter 6, the effect of the improvement to the forecasting of the prediction interval was also investigated with ensemble forecasting and Kalman Filter. The prediction interval was evaluated from the relationship between the ensemble spread and the forecasting error. The forecasting results with the univariate linear Kalman Filter and multivariate linear Kalman Filter were investigated separately. As a result, the sizes of prediction interval with Kalman Filters were narrower than that of forecasting without Kalman Filter. Also, the empirical coverage rates of observed GHI within prediction interval with the use of Kalman Filter close well to the nominal rates of prediction interval.

The findings of this study may provide some important and valuable information for the prediction of photovoltaic system generation. However, relevant investigations on how to use the prediction interval forecasted results of solar irradiance are still needed.

REFERENCES

1) Aoki, K., Takemura, T., Kawamoto, K., and Hayasaka, T. (2013). Aerosol climatology over Japan site measured by ground-based sky radiometer. In American Institute of Physics Conference Proceedings, 1531, 284-287.

2) BP. (2015) : BP statistical review of world energy June 2015. http://www.bp.com/content/dam/bp/pdf/energy-economics/statistical-review-2015/bp-statistical-review-of-world-energy-2015-full-report.pdf

3) Brier, G. W. (1950). Verification of forecasts expressed in terms of probability. Monthly weather review, 78(1), 1-3.

4) Brooks, H. E., and Doswell III, C. A. (1996). A comparison of measures-oriented and distributions-oriented approaches to forecast verification. Weather and forecasting, 11(3), 288-303.

5) Cassola, F., and Burlando, M. (2012). Wind speed and wind energy forecast through Kalman filtering of Numerical Weather Prediction model output. Applied Energy, 99, 154-166.

6) Chen, F., and Dudhia, J. (2001). Coupling an advanced land surface-hydrology model with the Penn State-NCAR MM5 modeling system. Part I: Model implementation and sensitivity. Monthly Weather Review, 129(4), 569-585.

7) Chen, S. H., and Sun, W. Y. (2002). A one-dimensional time dependent cloud model. Journal of the Meteorological Society of Japan, 80(1), 99-118.

8) Chou, M. D., and Suarez, M. J. (1994). An efficient thermal infrared radiation parameterization for use in general circulation models. NASA Tech. Memo, 104606(3), 85.

9) Collins, W. D., Rasch, P. J., Boville, B. A., Hack, J. J., McCaa, J. R., Williamson, D. L., Kiehl, J. T., Briegleb, B., Bitz, C., Lin, S. J., Zhang, M., and Dai, Y. (2004). Description of the NCAR community atmosphere model (CAM 3.0). NCAR Tech. Note NCAR/TN-464+ STR, 226.

10) DE Carvalho, J. R. P., Assad, E. D., and Pinto, H. S. (2011). Kalman filter and correction of the temperatures estimated by PRECIS model. Atmospheric Research, 102(1), 218-226.

11) Delle Monache, L., Wilczak, J., Mckeen, S., Grell, G., Pagowski, M., Peckham, S., Stull, R., and Mcqueen, J. (2008). A Kalman - filter bias correction method applied to deterministic, ensemble averaged and probabilistic forecasts of surface ozone. Tellus B, 60(2), 238-249.

12) Diagne, M., David, M., Boland, J., Schmutz, N., and Lauret, P. (2014). Post-processing of solar irradiance forecasts from WRF model at Reunion Island. Solar Energy, 105, 99-108.

13) Diagne, M., David, M., Lauret, P., Boland, J., and Schmutz, N. (2013). Review of solar irradiance forecasting methods and a proposition for small-scale insular grids. Renewable and Sustainable Energy Reviews, 27, 65-76.

14) Diaz, D., Souto, J. A., Rodriguez, A., Saavedra, S., and Casares, J. J. (2012). An ensemble-in-time forecast of solar irradiance. Proceedings of the International Conferece on Renewable Energies and Power Quality, Santiago de Compostela.

15) Donlon, C. J., Martin, M., Stark, J., Roberts-Jones, J., Fiedler, E., & Wimmer, W. (2012). The operational sea surface temperature and sea ice analysis (OSTIA) system. Remote Sensing of Environment, 116, 140-158.

16) Dudhia, J. (1989). Numerical study of convection observed during the winter

monsoon experiment using a mesoscale two-dimensional model. Journal of the Atmospheric Sciences, 46(20), 3077-3107.

17) Dudhia, J., Hong, S. Y., and Lim, K. S. (2008). A new method for representing mixed-phase particle fall speeds in bulk microphysics parameterizations. Journal of the Meteorological Society of Japan, 86, 33-44.

18) EKO INSTRUMENTS CO., LTD. Pyranometers -Instruction Manual Version 9. http://eko-eu.com/files/PyranometerManual20150306V9.pdf

19) Fels, S. B., and Schwarzkopf, M. D. (1975). The simplified exchange approximation: A new method for radiative transfer calculations. Journal of the Atmospheric Sciences, 32(7), 1475-1488.

20) Furukawa, T., and Sakai, S. (2004). Ensemble forecasting —New medium and long-term forecast and use—. Tokyo University Press. (in Japanese)

21) Galanis, G., Louka, P., Katsafados, P., Pytharoulis, I., and Kallos, G. (2006). Applications of Kalman filters based on non-linear functions to numerical weather predictions. In Annales Geophysicae, 24(10), 2451-2460. Copernicus GmbH.

22) Grell, G. A., and Dévényi, D. (2002). A generalized approach to parameterizing convection combining ensemble and data assimilation techniques. Geophysical Research Letters, 29(14), 38-1.

23) Hair, J. F., Black, W. C., Babin, B. J., Anderson, R. E., and Tatham, R. L. (2006). Multivariate data analysis (Vol. 6). Upper Saddle River, NJ: Pearson Prentice Hall.

24) Haltiner, G. J., and Williams, R. T. (1980). Numerical prediction and dynamic meteorology (Vol. 2). New York: Wiley.

25) Hashimoto, J., and Kobayashi, T. (2011). Solar Spectral Irradiance Model for Forecast of Photovoltaic Power Generation. Japanese Journal of multiphase flow,

25(3), 229-236.

26) Heinemann, D., Lorenz, E., and Girodo, M. (2006). Solar irradiance forecasting for the management of solar energy systems. Energy and Semiconductor Research Laboratory, Energy Meteorology Group, Oldenburg University.

27) Hoffman, R. N., and Kalnay, E. (1983). Lagged average forecasting, an alternative to Monte Carlo forecasting. Tellus A, 35(2), 100-118.

28) Homleid, M. (1995). Diurnal corrections of short-term surface temperature forecasts using the Kalman filter. Weather and Forecasting, 10(4), 689-707.

29) Hong, S. Y., Dudhia, J., and Chen, S. H. (2004). A revised approach to ice microphysical processes for the bulk parameterization of clouds and precipitation. Monthly Weather Review, 132(1), 103-120.

30) Hong, S. Y., and Lim, J. O. J. (2006). The WRF single-moment 6-class microphysics scheme (WSM6). Asia-Pacific Journal of Atmospheric Sciences, 42(2), 129-151.

31) International Energy Agency Photovoltaic Power Systems Programme. (2015) : http://www.iea-pvps.org/fileadmin/dam/public/report/technical/PVPS_report_-_A_Snapshot_of_Global_PV_-_1992-2014.pdf

32) Janjic, Z. I. (1994). The step-mountain eta coordinate model: Further developments of the convection, viscous sublayer, and turbulence closure schemes. Monthly Weather Review, 122(5), 927-945.

33) Janjic, Z. I. (2000). Comments on “Development and evaluation of a convection scheme for use in climate models”. Journal of the Atmospheric Sciences, 57(21), 3686-3686.

34) Japan Meteorological Business Support Center. (2015) : Global Numerical Prediction Model, GPV (GSM). (in Japanese)

http://www.jmbsc.or.jp/hp/online/f-online0a.html access 2015/07/20

35) Jensenius J.S., and Cotton G.F. (1981). The development and testing of automated solar energy forecasts based on the model output statistics (MOS) technique. Proceedings 1st Workshop on Terrestrial Solar Resource Forecasting and on the Use of Satellites for Terrestrial Solar Resource Assessment, Network, American Solar Energy Society.

36) Kain, J. S. (2004). The Kain-Fritsch convective parameterization: an update. Journal of Applied Meteorology, 43(1), 170-181.

37) Kalman, R. E. (1960). A new approach to linear filtering and prediction problems. Journal of Fluids Engineering, 82(1), 35-45.

38) Kessler, E. (1969). On the distribution and continuity of water substance in atmospheric circulations. Meteorological Monographs/American Meteorological Society, 32(10), 82-84.

39) Kim, P. (2011). Kalman filter for beginners with Matlab examples, [s.n.], pp.47-72.

40) Kunitsugu, M. (1997). Statistical guidance systems using Kalman Filter technique. Meteorological Society of Japan. (in Japanese)

41) Lacis, A. A., and Hansen, J. (1974). A parameterization for the absorption of solar radiation in the earth's atmosphere. Journal of the Atmospheric Sciences, 31(1), 118-133.

42) Lange, M., and Focken, U. (2006). Physical approach to short-term wind power prediction (pp. 1-208). Berlin: Springer.

43) Laprise, R. (1992). The Euler equations of motion with hydrostatic pressure as an independent variable. Monthly weather review, 120(1), 197-207.

44) Lara-Fanego, V., Ruiz-Arias, J. A., Pozo-Vázquez, D., Santos-Alamillos, F. J., and

Tovar-Pescador, J. (2012). Evaluation of the WRF model solar irradiance forecasts in Andalusia (southern Spain). Solar Energy, 86(8), 2200-2217.

45) Lin, Y. L., Farley, R. D., and Orville, H. D. (1983). Bulk parameterization of the snow field in a cloud model. Journal of Climate and Applied Meteorology, 22(6), 1065-1092.

46) Liu, Y., Shimada, S., Yoshino, J., Kobayashi, T., Furuta, K., and Miwa, Y. (2014). Solar irradiance forecasting using the WRF model and Kalman filter. Grand Renewable Energy 2014 International Conference and Exhibition, 4p.

47) Liu, Y., Shimada, S., Yoshino, J., and Kobayashi, T. (2015). Ensemble forecasting of solar irradiance by applying a mesoscale meteorological model, Solar Energy, Elsevier. (submitted)

48) Lorenz, E., Hurka, J., Heinemann, D., and Beyer, H. G. (2009). Irradiance Forecasting for the Power Prediction of Grid-Connected photovoltaic Systems. IEEE Journal of Selected Topics in Applied Earth and Observations and Remote Sensing, 2(1), 2-10.

49) Lorenz, E., and Heinemann, D. (2012). Prediction of Solar Irradiance and Photovoltaic Power. Comprehensive Renewable Energy. Elsevier, Oxford, 239-292.

50) Lorenz, E., Remund, J., Müller, S. C., Traunmüller, W., Steinmaurer, G., D. G., J.A. Ruiz-Arias, V.L. Fanego, Ramirez L., Remo M.G., Kurz C., Pomares L.M., and Guerrero C.G. (2009). Benchmarking of different approaches to forecast solar irradiance. In Proceedings of the 24th European Photovoltaic and Solar Energy Conference and Exhibition, 4199-4208.

51) Mellor, G. L., and Yamada, T. (1982). Development of a turbulence closure model for geophysical fluid problems. Reviews of geophysics and space physics, 20(4),

851-875.

52) Ministry of Economy, Trade and Industry. (2015) : http://www.enecho.meti.go.jp/about/whitepaper/2015pdf/whitepaper2015pdf_3_3.pdf (in Japanese)

53) Mlawer, E. J., Taubman, S. J., Brown, P. D., Iacono, M. J., and Clough, S. A. (1997). Radiative transfer for inhomogeneous atmospheres: RRTM, a validated correlated - k model for the long wave. Journal of Geophysical Research: Atmospheres, 102(D14), 16663-16682.

54) Molteni, F., Buizza, R., Palmer, T. N., and Petroliagis, T. (1996). The ECMWF ensemble prediction system: Methodology and validation. Quarterly Journal of the Royal Meteorological Society, 122(529), 73-119.

55) Morrison, H., Curry, J. A., and Khvorostyanov, V. I. (2005). A new double-moment microphysics parameterization for application in cloud and climate models. Part I: Description. Journal of the Atmospheric Sciences, 62(6), 1665-1677.

56) Morrison, H., and Pinto, J. O. (2006). Intercomparison of bulk cloud microphysics schemes in mesoscale simulations of springtime Arctic mixed-phase stratiform clouds. Monthly weather review, 134(7), 1880-1900.

57) Morrison, H., Thompson, G., and Tatarskii, V. (2009). Impact of cloud microphysics on the development of trailing stratiform precipitation in a simulated squall line: Comparison of one-and two-moment schemes. Monthly Weather Review, 137(3), 991-1007.

58) National Centers for Environmental Prediction. (2015) : Global Forecast System. http://www.nco.ncep.noaa.gov/pmb/products/gfs/ access 2015/07/20

59) National Centre for Ocean Forecasting. (2015) : OSTIA Sea Surface Temperatures

and Sea Ice.
http://www.ncof.co.uk/OSTIA-Daily-Sea-Surface-Temperature-and-Sea-Ice.html access 2015/07/20

60) Oozeki, T., Kato, T., and Ogimoto, K. (2011). Current status of output forecasting for Photovoltaic systems. The papers of Technical Meeting on Metabolism Society and Environmental Systems, IEE Japan, MES-11-004, 19-24. (in Japanese)

61) Palmer, T. N., Barkmeijer, J., Buizza, R., Klinker, E., and Richardson, D. (2000). The future of the ensemble prediction, ECMWF Newsletter, 88, 2-8.

62) Pelland, S., Galanis, G., and Kallos, G. (2013). Solar and photovoltaic forecasting through post-processing of the Global Environmental Multiscale numerical weather prediction model. Progress in Photovoltaics: Research and Applications, 21(3), 284-296.

63) Perez, R., Kivalov, S., Schlemmer, J., Hemker, K., Renné, D., and Hoff, T. E. (2010). Validation of short and medium term operational solar radiation forecasts in the US, Solar Energy, 84(12), 2161–2172.

64) Reikard, G. (2009). Predicting solar radiation at high resolutions: A comparison of time series forecasts. Solar Energy, 83(3), 342-349.

65) Richardson, D. S. (2000). Skill and relative economic value of the ECMWF ensemble prediction system. Quarterly Journal of the Royal Meteorological Society, 126(563), 649-667.

66) Rincón, A., Jorba, O., Baldasano, J. M., and Delle Monache, L. (2011). Assessment of short-term irradiance forecasting based on post-processing tools applied on WRF meteorological simulations. In State-of-the-Art Workshop, COST ES 1002, 1-9.

67) Rutledge, S. A., and Hobbs, P. V. (1984). The mesoscale and microscale structure

and organization of clouds and precipitation in midlatitude cyclones. XII: A diagnostic modeling study of precipitation development in narrow cold-frontal rainbands. Journal of the Atmospheric Sciences, 41(20), 2949-2972.

68) Sanders, F. (1967). The verification of probability forecasts. Journal of Applied Meteorology, 6(5), 756-761.

69) Schwarzkopf, M. D., and Fels, S. B. (1991). The simplified exchange method revisited: An accurate, rapid method for computation of infrared cooling rates and fluxes. Journal of Geophysical Research: Atmospheres (1984–2012), 96(D5), 9075-9096.

70) Seidman, A. N. (1981). Averaging techniques in long-range weather forecasting. Monthly Weather Review, 109(7), 1367-1379.

71) Shimada, S., Liu, Y., Xia, H., Yoshino, J., Kobayashi, T., Itagaki, A., Utsunomiya, T., and Hashimoto, J. (2012). Accuracy of solar irradiance simulation using the WRF-ARW model. Journal of Japan Solar Energy Society, 38(5), 41-48. (in Japanese)

72) Shimada, S., Liu, Y., Yoshimo, J., Kobayashi, T., Wazawa, Y. (2013). Solar irradiance forecasting using a mesoscale meteorological model. Part Ⅱ: Increasing the accuracy using the Kalman filte. Journal of Japan Solar Energy Society, 39(3), 61-67. (in Japanese)

73) Skamarock, W. C., Klemp, J. B., Dudhia, J., Gill, D. O., Barker, D. M., Wang, W., and Powers, J. G. (2008). A description of the advanced research WRF version 3. NCAR Technical Note NCAR/TN-475+STR, University Corporation for Atmospheric Research, 1-96.

74) Stensrud, D. J. (2007). Parameterization schemes: keys to understanding

numerical weather prediction models. Cambridge University Press.

75) Tao, W. K., and Simpson, J. (1993). The Goddard cumulus ensemble model. Part I: Model description. Terr. Atmos. Oceanic Sci, 4(1), 35-72.

76) Thompson, G., Rasmussen, R. M., and Manning, K. (2004). Explicit forecasts of winter precipitation using an improved bulk microphysics scheme. Part I: Description and sensitivity analysis. Monthly Weather Review, 132(2), 519-542.

77) Verzijlbergh, R. A., Heijnen, P. W., de Roode, S. R., Los, A., and Jonker, H. J. (2015). Improved model output statistics of numerical weather prediction based irradiance forecasts for solar power applications. Solar Energy, 118, 634-645.

78) Wei, M., Toth, Z., Wobus, R., and Zhu, Y. (2008). Initial perturbations based on the ensemble transform (ET) technique in the NCEP global operational forecast system. Tellus, 60(1), 62-79.

79) Wilks, D. S. (1990). Probabilistic quantitative precipitation forecasts derived from PoPs and conditional precipitation amount climatologies. Monthly Weather Review, 118(4), 874-882.

80) Yoshino, J., Tanaka, A., Fukao, K., Kobayashi, T., and Yasuda, T. (2006). Short-term wind power forecasts using a mesoscale meteorological model with the Kalman Filter. Wind Energy Utilization Symposium, 28, 176-179.

81) Zamora, R. J., Solomon, S., Dutton, E. G., Bao, J. W., Trainer, M., Portmann, R. W., White, A. B., Nelson, D. W., and McNider, R. T. (2003). Comparing MM5 radiative fluxes with observations gathered during the 1995 and 1999 Nashville southern oxidants studies. Journal of Geophysical Research: Atmospheres (1984–2012), 108(D2).

Appendix

Time series of observed and forecasted solar irradiance (Global Horizontal Irradiance, GHI) and its 50%, 80%, 90%, 95% prediction interval for the intra-day forecasting are shown in this section. GHI values are obtained by calculating mean values in 61 observation sites and with 30-minute interval. **Figure A.1** to **A.9** show the results with WRF only for ten days from 1st to 10th each month. **Figure B.1** to **B.9** show the results with WRF and univariate Kalman Filter for ten days from 1st to 10th each month. **Figure C.1** to **C.9** show the results with WRF and multivariate Kalman Filter for ten days from 1st to 10th each month. The period is from October 2013 to June 2014.

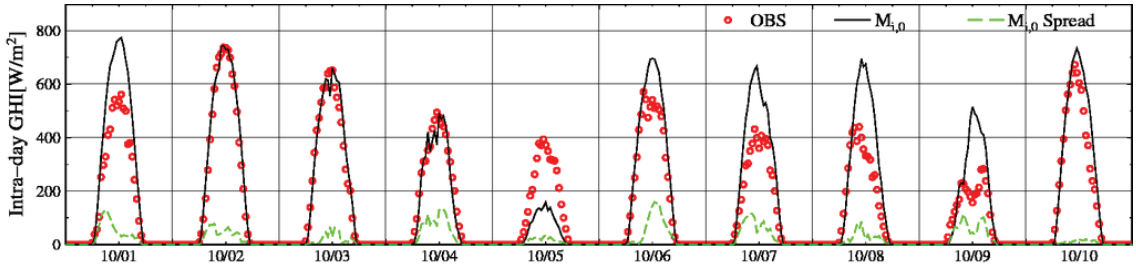

(a1) $M_{i,0}$ and Spread

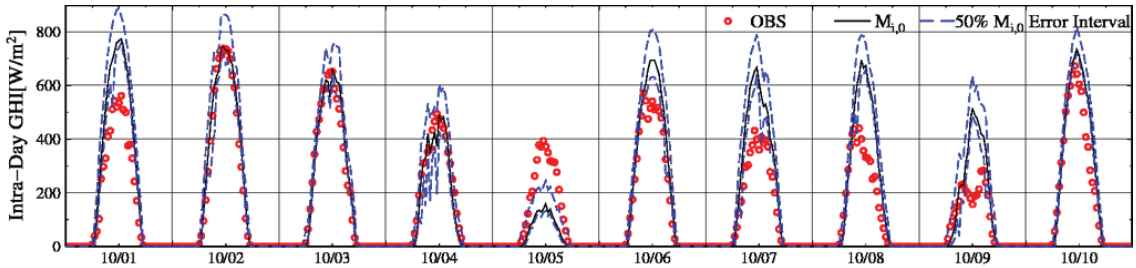

(b1) $M_{i,0}$ and 50% prediction interval

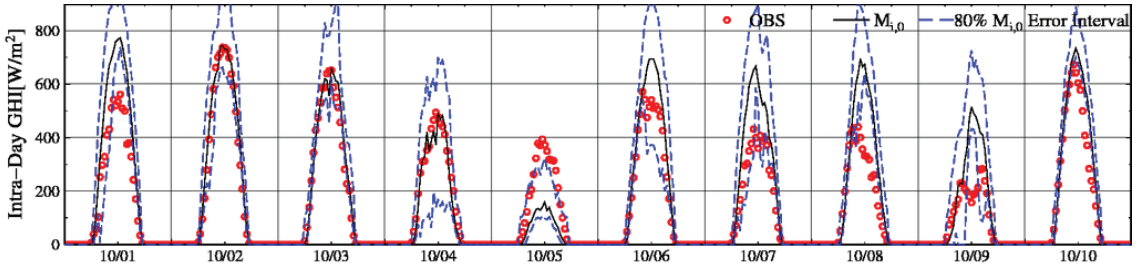

(c1) $M_{i,0}$ and 80% prediction interval

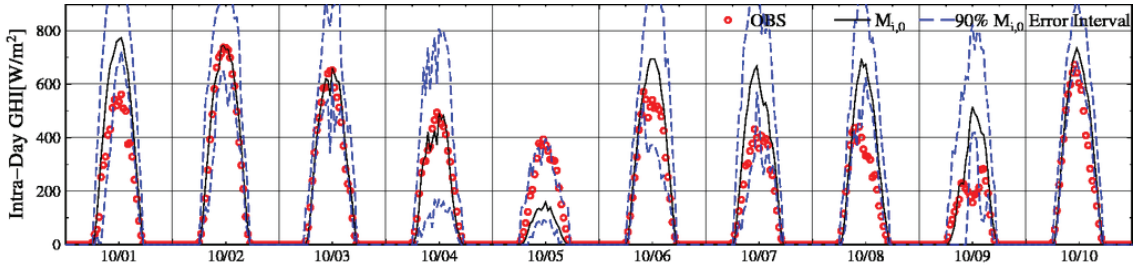

(d1) $M_{i,0}$ and 90% prediction interval

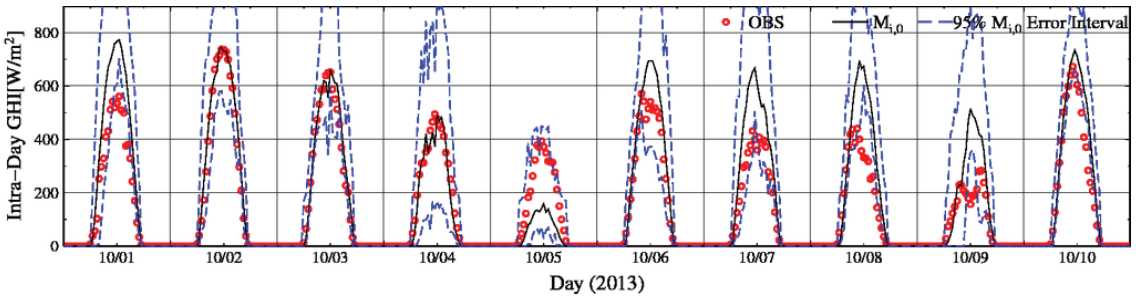

(e1) $M_{i,0}$ and 95% prediction interval

Fig. A.1 Time series of observed and forecasted solar irradiance (GHI) and its 50%, 80%, 90%, 95% prediction interval for the intra-day forecasting $M_{i,0}$ (61 observation-point average, from Oct 1st to 10th, 2013)

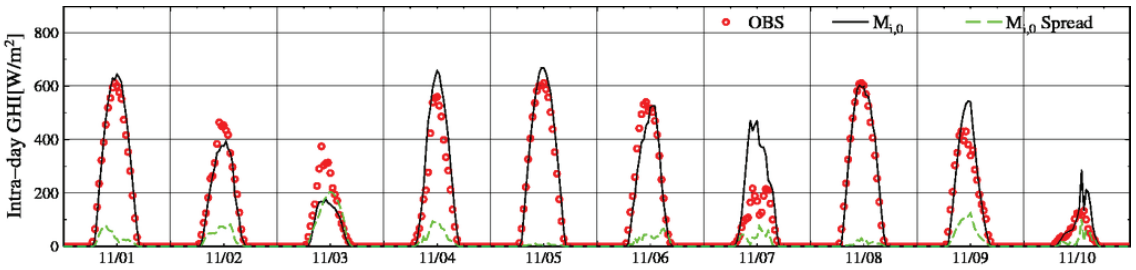

(a2) $M_{i,0}$ and Spread

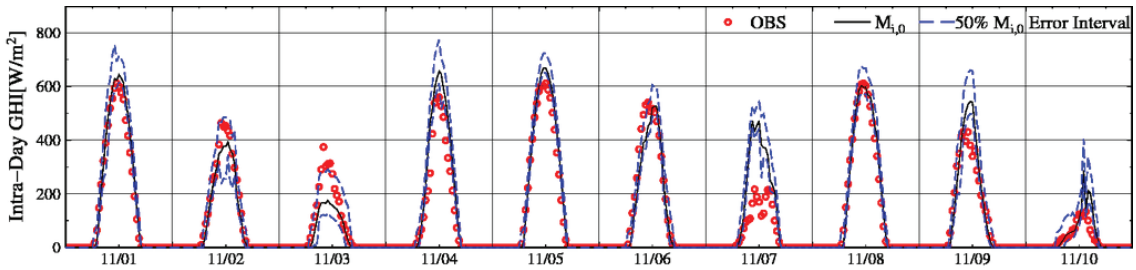

(b2) $M_{i,0}$ and 50% prediction interval

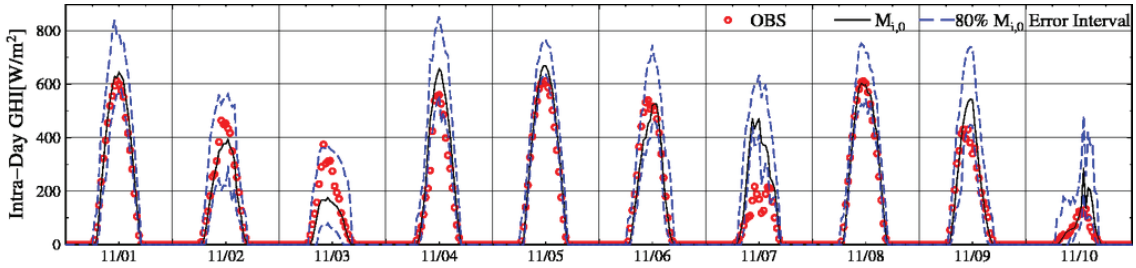

(c2) $M_{i,0}$ and 80% prediction interval

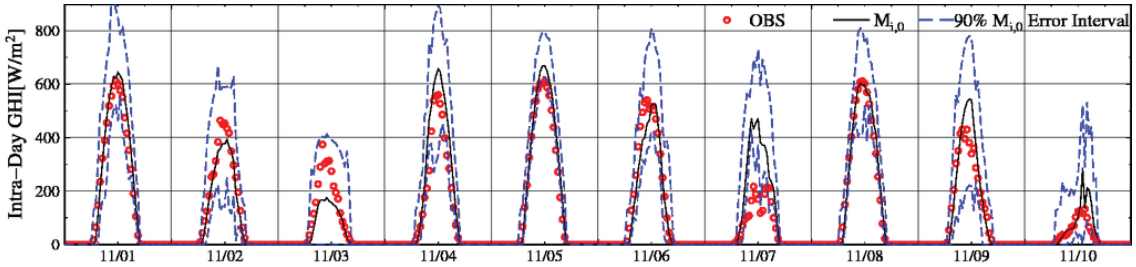

(d2) $M_{i,0}$ and 90% prediction interval

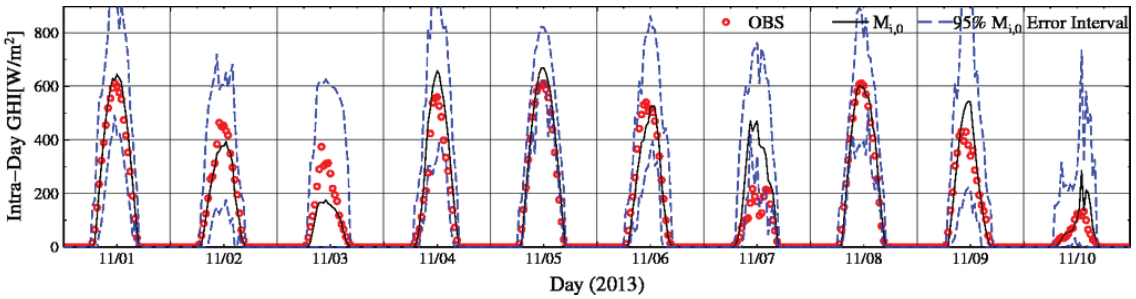

(e2) $M_{i,0}$ and 95% prediction interval

Fig. A.2 Time series of observed and forecasted solar irradiance (GHI) and its 50%, 80%, 90%, 95% prediction interval for the intra-day forecasting $M_{i,0}$ (61 observation-point average, from Nov 1st to 10th, 2013)

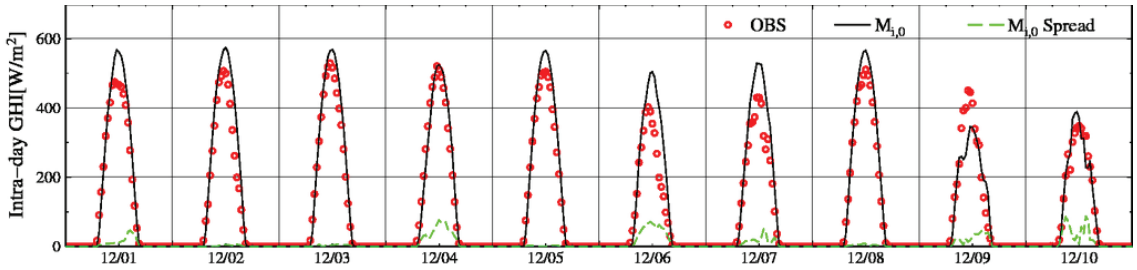

(a3) $M_{i,0}$ and Spread

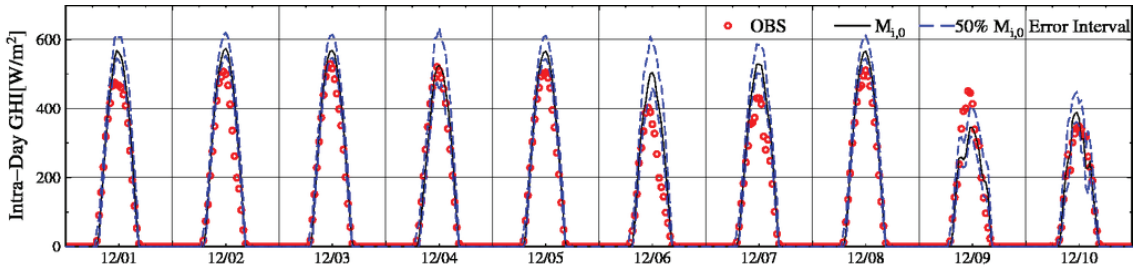

(b3) $M_{i,0}$ and 50% prediction interval

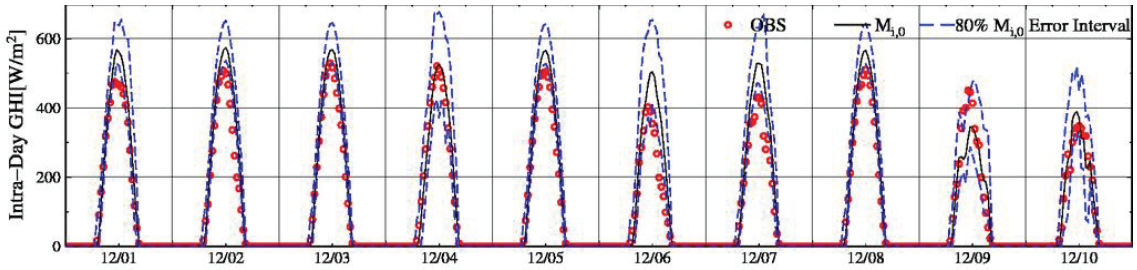

(c3) $M_{i,0}$ and 80% prediction interval

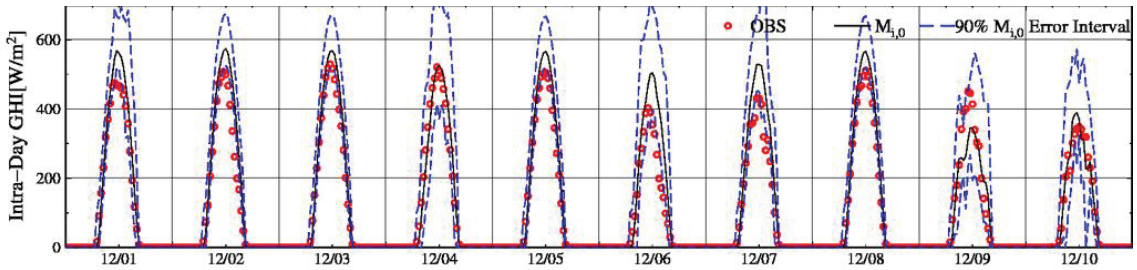

(d3) $M_{i,0}$ and 90% prediction interval

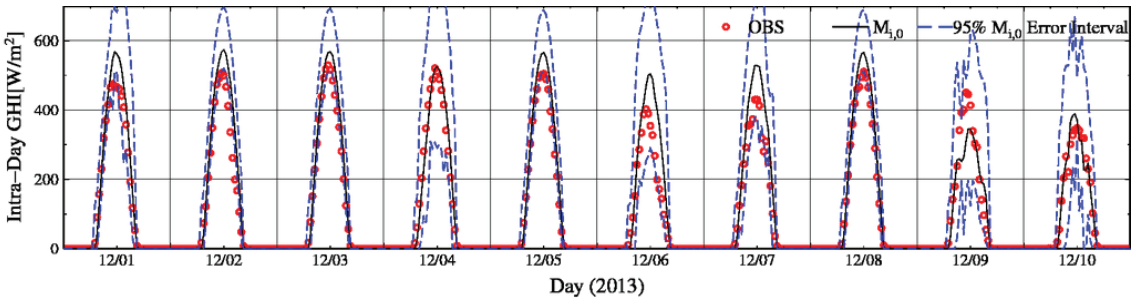

(e3) $M_{i,0}$ and 95% prediction interval

Fig. A.3 Time series of observed and forecasted solar irradiance (GHI) and its 50%, 80%, 90%, 95% prediction interval for the intra-day forecasting $M_{i,0}$ (61 observation-point average, from Dec 1st to 10th, 2013)

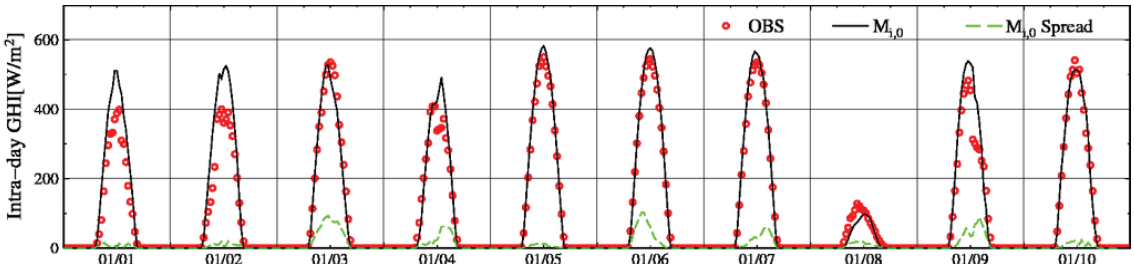

(a4) $M_{i,0}$ and Spread

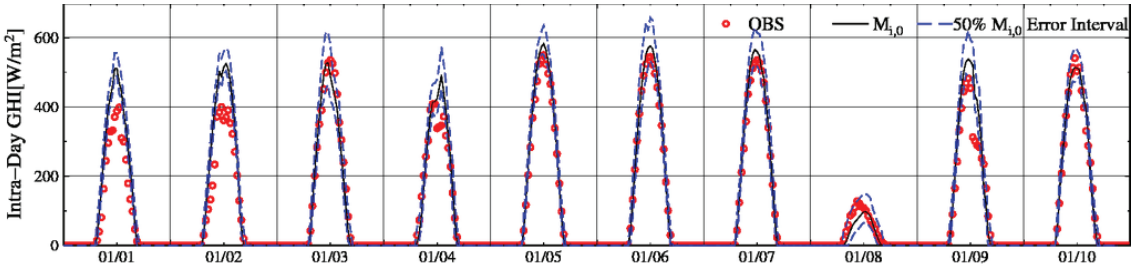

(b4) $M_{i,0}$ and 50% prediction interval

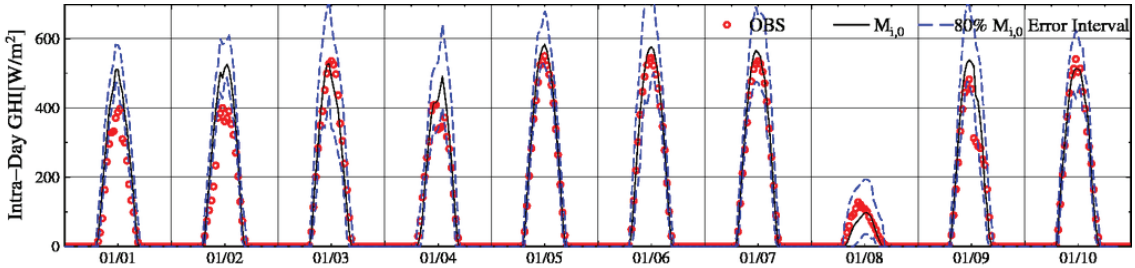

(c4) $M_{i,0}$ and 80% prediction interval

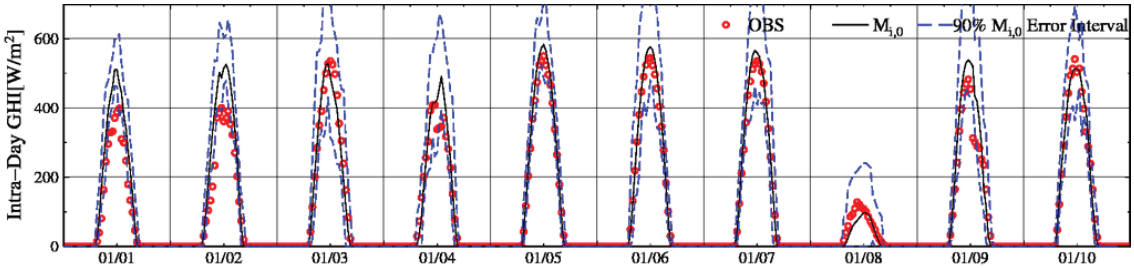

(d4) $M_{i,0}$ and 90% prediction interval

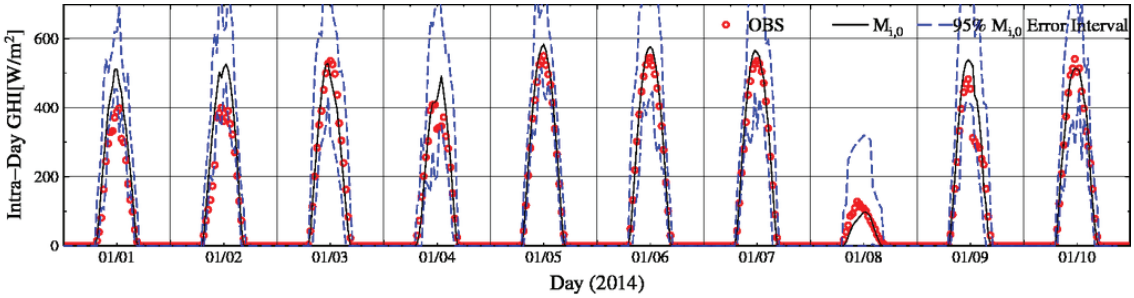

(e4) $M_{i,0}$ and 95% prediction interval

Fig. A.4 Time series of observed and forecasted solar irradiance (GHI) and its 50%, 80%, 90%, 95% prediction interval for the intra-day forecasting $M_{i,0}$ (61 observation-point average, from Jan 1st to 10th, 2014)

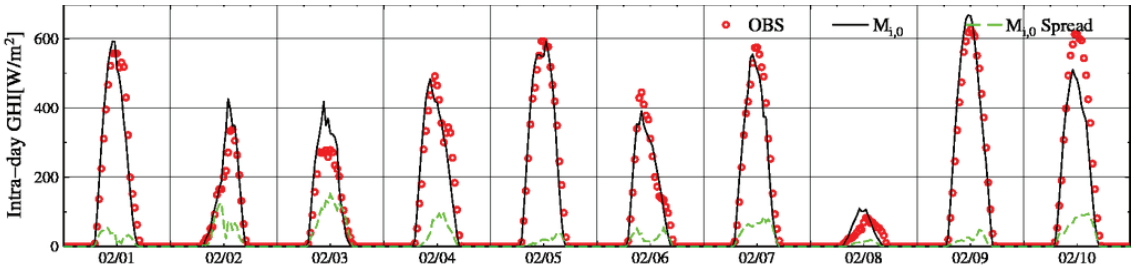

(a5) $M_{i,0}$ and Spread

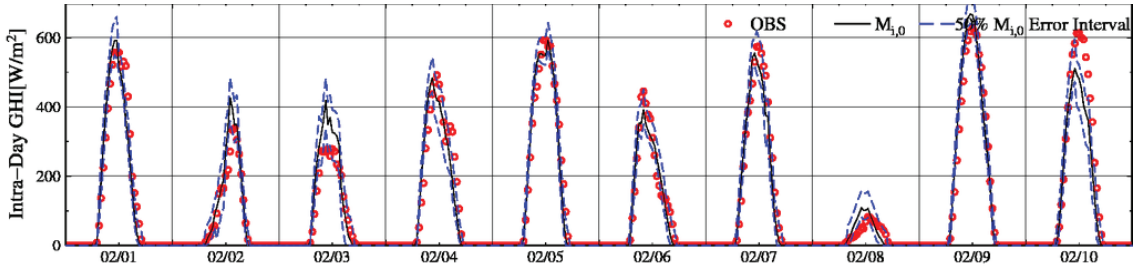

(b5) $M_{i,0}$ and 50% prediction interval

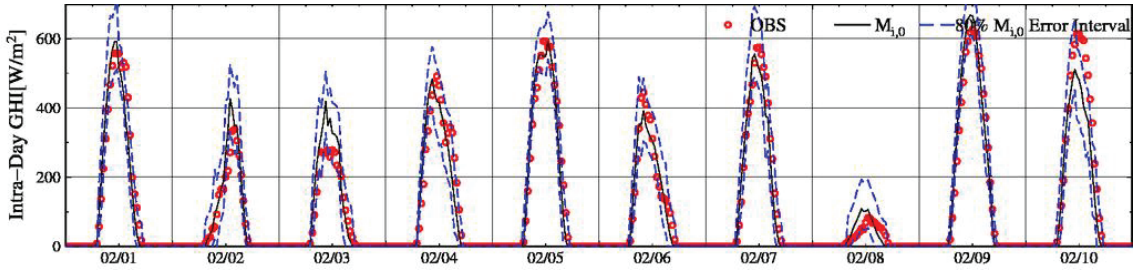

(c5) $M_{i,0}$ and 80% prediction interval

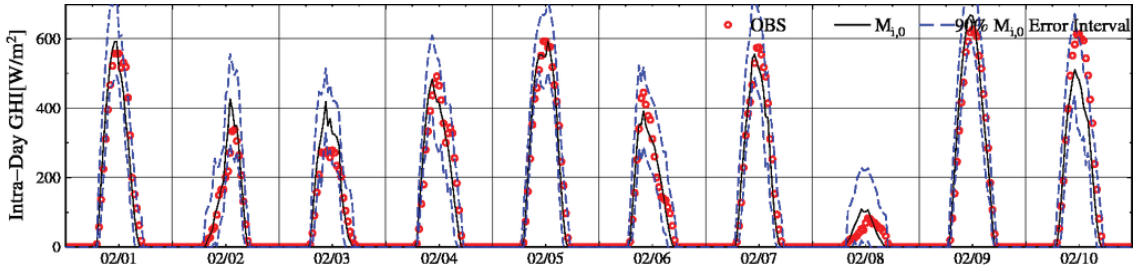

(d5) $M_{i,0}$ and 90% prediction interval

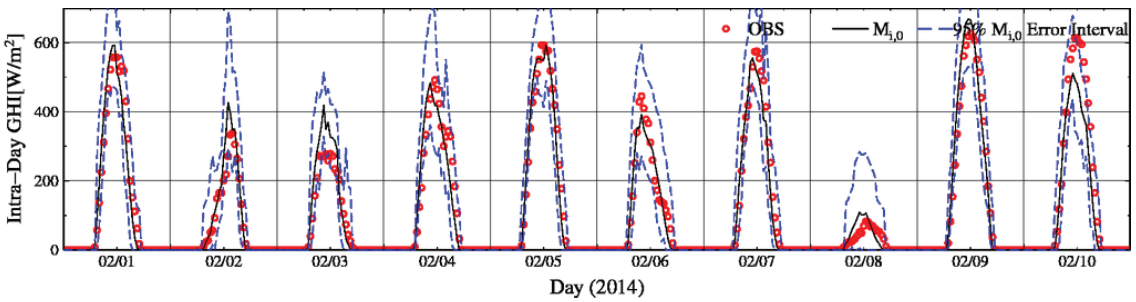

(e5) $M_{i,0}$ and 95% prediction interval

Fig. A.5 Time series of observed and forecasted solar irradiance (GHI) and its 50%, 80%, 90%, 95% prediction interval for the intra-day forecasting $M_{i,0}$ (61 observation-point average, from Feb 1st to 10th, 2014)

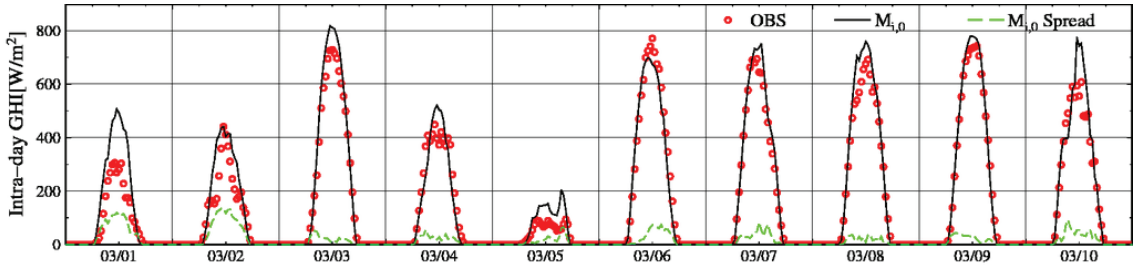

(a6) $M_{i,0}$ and Spread

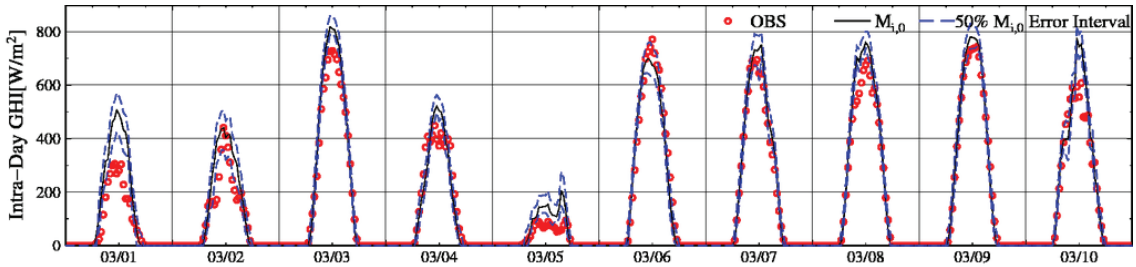

(b6) $M_{i,0}$ and 50% prediction interval

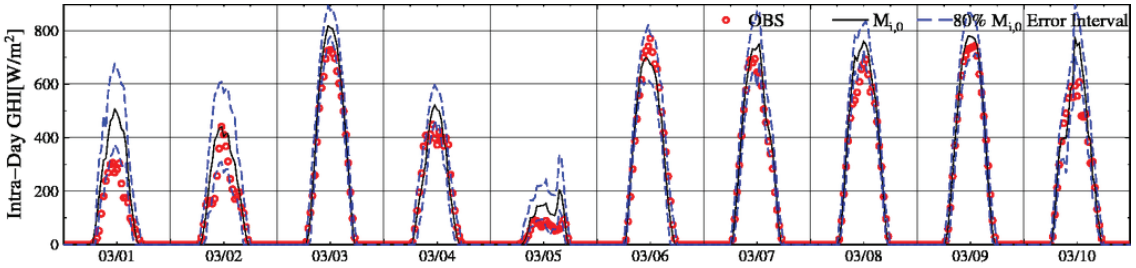

(c6) $M_{i,0}$ and 80% prediction interval

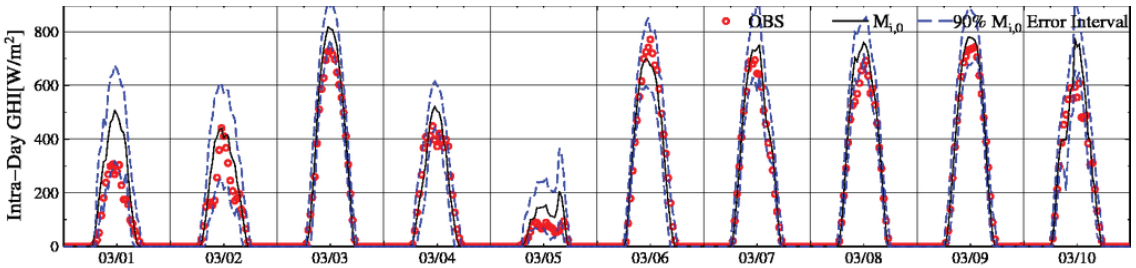

(d6) $M_{i,0}$ and 90% prediction interval

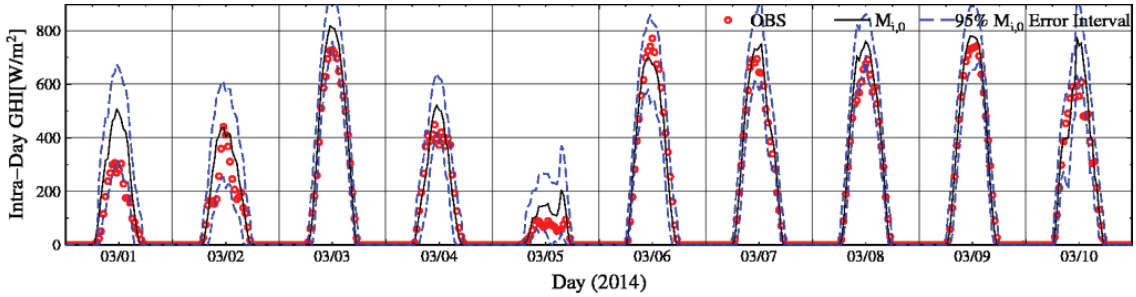

(e6) $M_{i,0}$ and 95% prediction interval

Fig. A.6 Time series of observed and forecasted solar irradiance (GHI) and its 50%, 80%, 90%, 95% prediction interval for the intra-day forecasting $M_{i,0}$ (61 observation-point average, from Mar 1st to 10th, 2014)

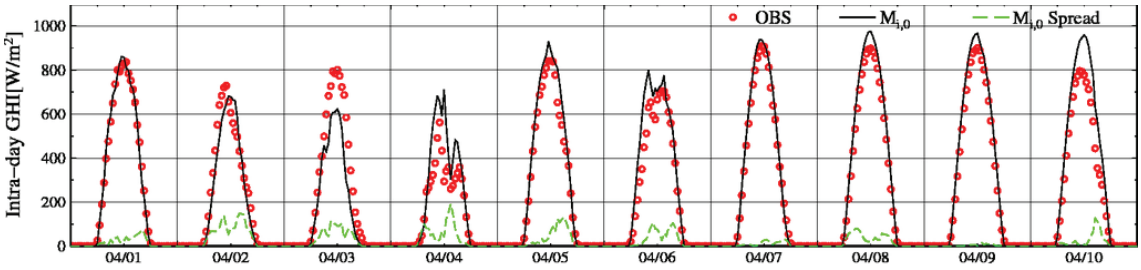

(a7) $M_{i,0}$ and Spread

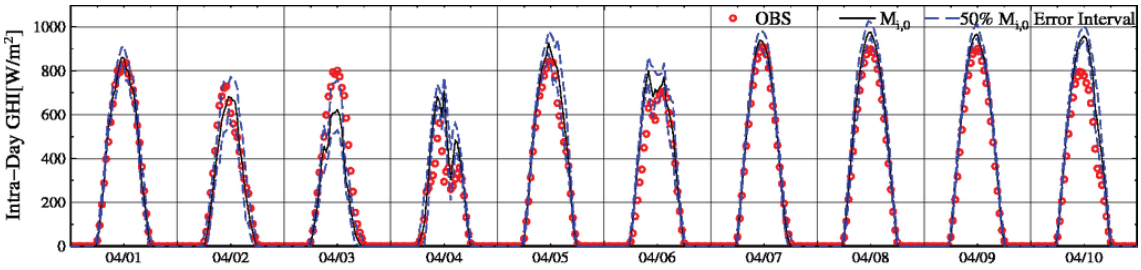

(b7) $M_{i,0}$ and 50% prediction interval

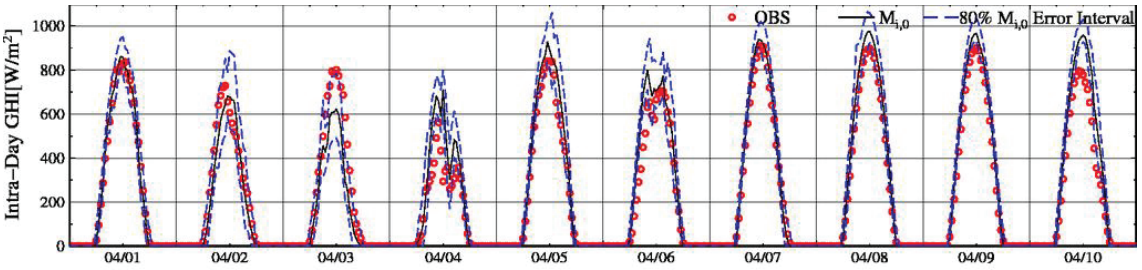

(c7) $M_{i,0}$ and 80% prediction interval

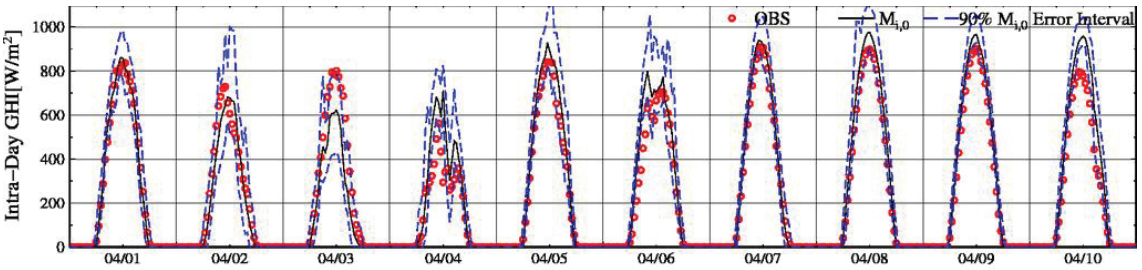

(d7) $M_{i,0}$ and 90% prediction interval

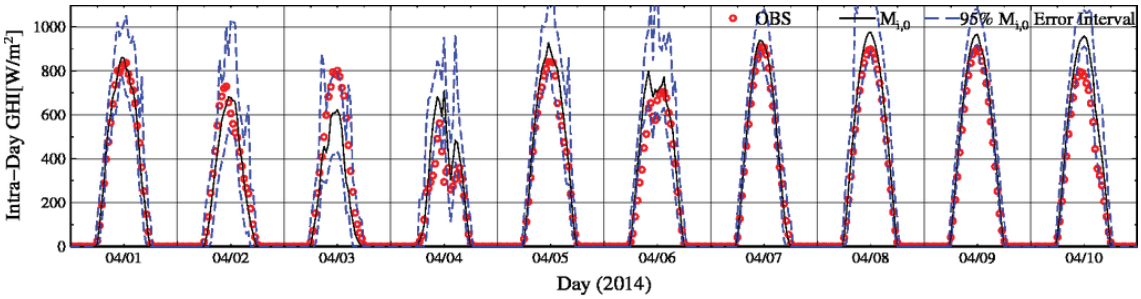

(e7) $M_{i,0}$ and 95% prediction interval

Fig. A.7 Time series of observed and forecasted solar irradiance (GHI) and its 50%, 80%, 90%, 95% prediction interval for the intra-day forecasting $M_{i,0}$ (61 observation-point average, from Apr 1st to 10th, 2014)

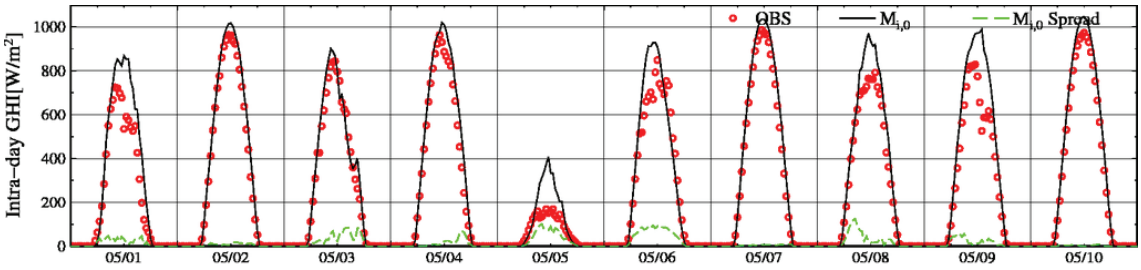

(a8) $M_{i,0}$ and Spread

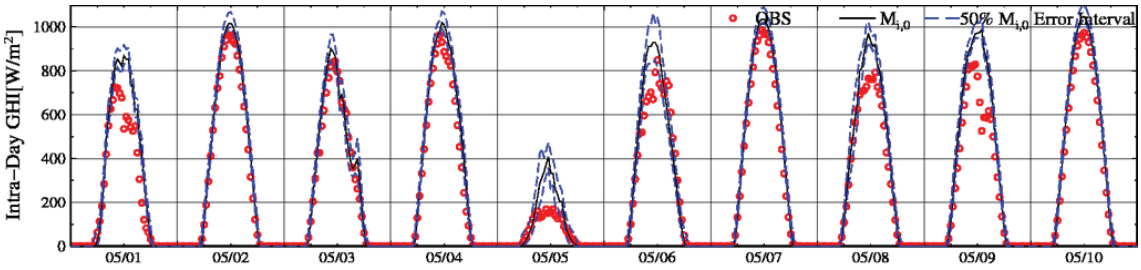

(b8) $M_{i,0}$ and 50% prediction interval

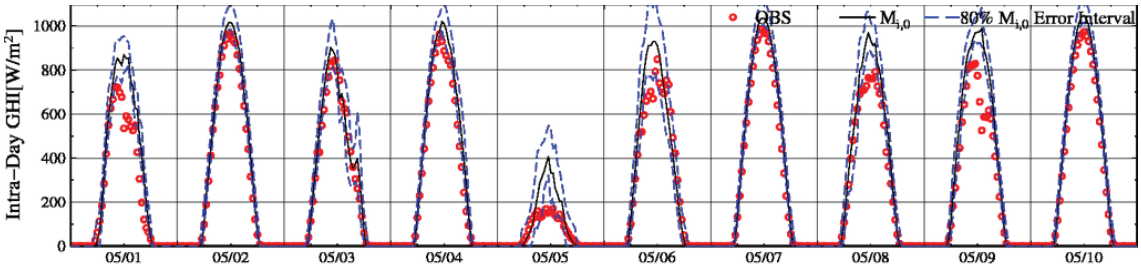

(c8) $M_{i,0}$ and 80% prediction interval

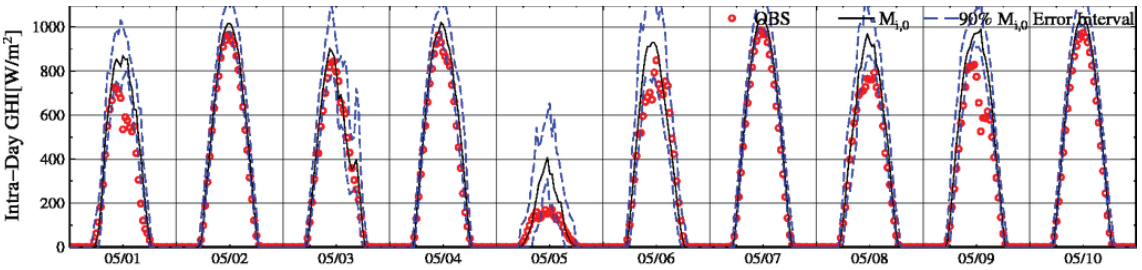

(d8) $M_{i,0}$ and 90% prediction interval

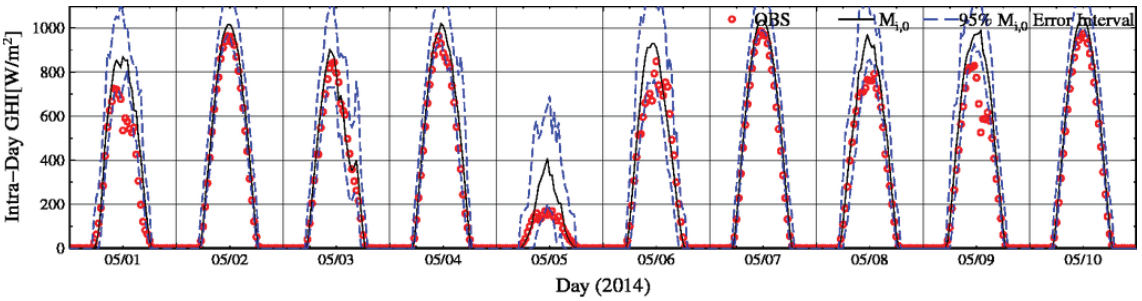

(e8) $M_{i,0}$ and 95% prediction interval

Fig. A.8 Time series of observed and forecasted solar irradiance (GHI) and its 50%, 80%, 90%, 95% prediction interval for the intra-day forecasting $M_{i,0}$ (61 observation-point average, from May 1st to 10th, 2014)

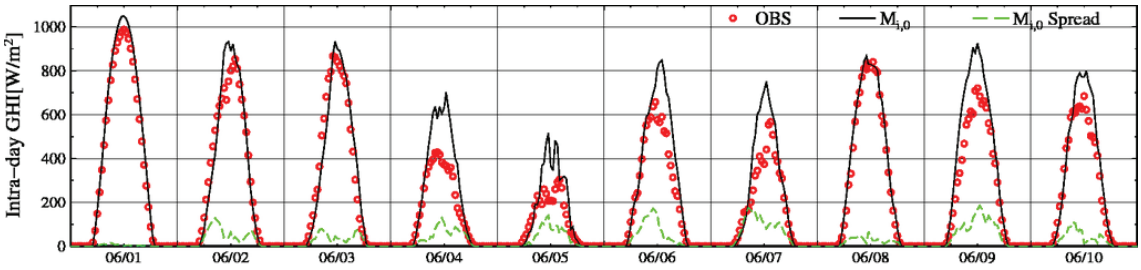

(a9) $M_{i,0}$ and Spread

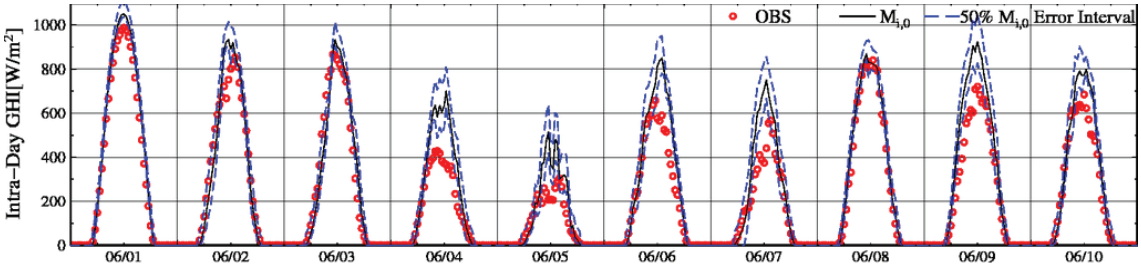

(b9) $M_{i,0}$ and 50% prediction interval

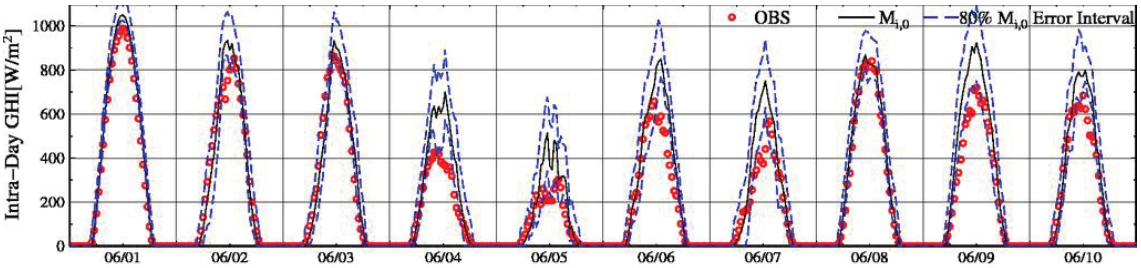

(c9) $M_{i,0}$ and 80% prediction interval

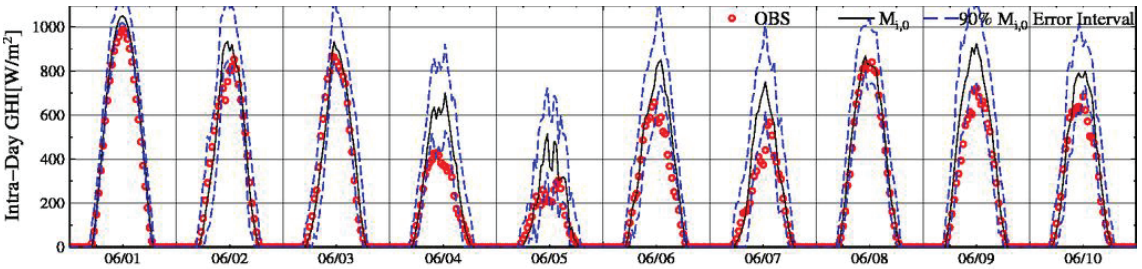

(d9) $M_{i,0}$ and 90% prediction interval

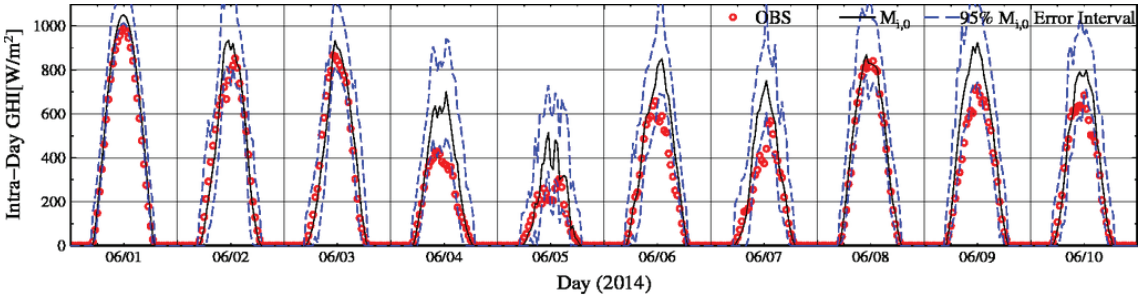

(e9) $M_{i,0}$ and 95% prediction interval

Fig. A.9 Time series of observed and forecasted solar irradiance (GHI) and its 50%, 80%, 90%, 95% prediction interval for the intra-day forecasting $M_{i,0}$ (61 observation-point average, from Jun 1st to 10th, 2014)

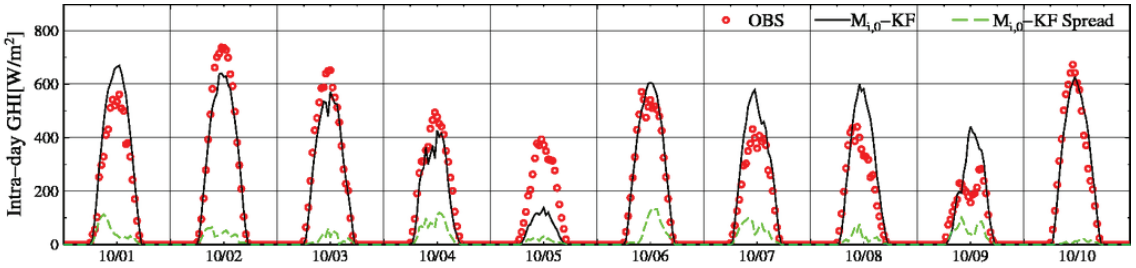

(a1') $M_{i,0}-KF$ and Spread

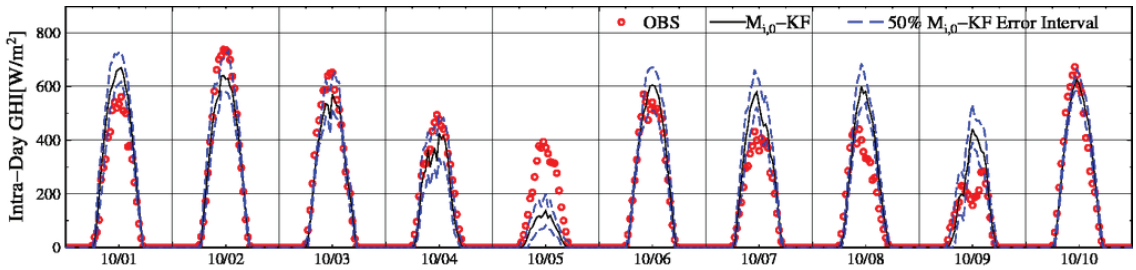

(b1') $M_{i,0}-KF$ and 50% prediction interval

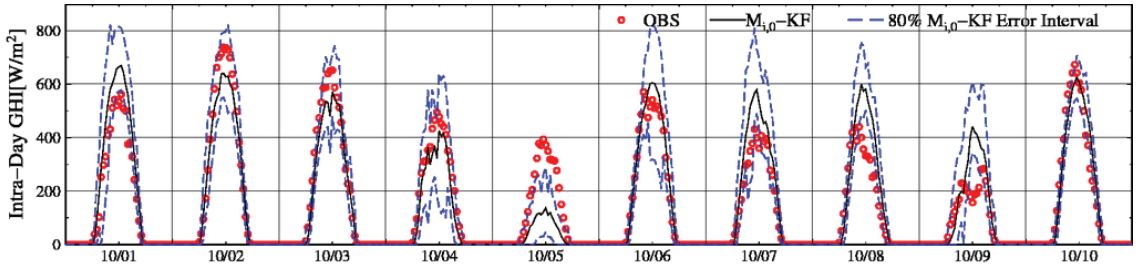

(c1') $M_{i,0}-KF$ and 80% prediction interval

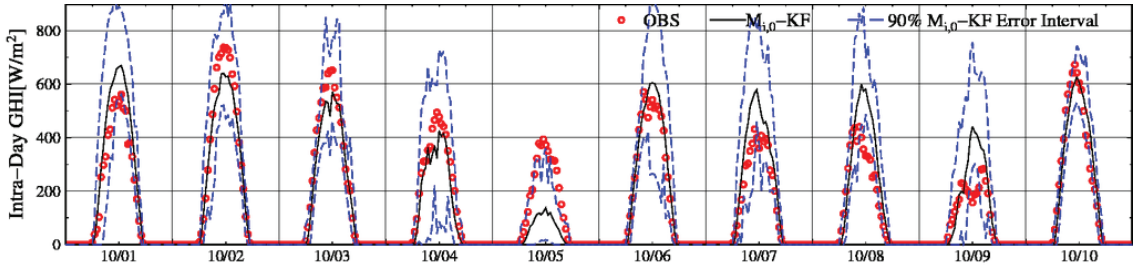

(d1') $M_{i,0}-KF$ and 90% prediction interval

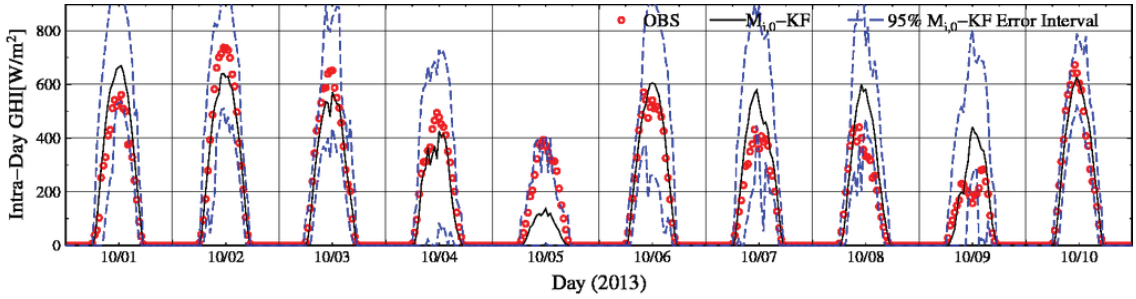

(e1') $M_{i,0}-KF$ and 95% prediction interval

Fig. B.1 Time series of observed and forecasted solar irradiance (GHI) and its 50%, 80%, 90%, 95% prediction interval for the intra-day forecasting $M_{i,0}-KF$ (61 observation-point average, from Oct 1st to 10th, 2013)

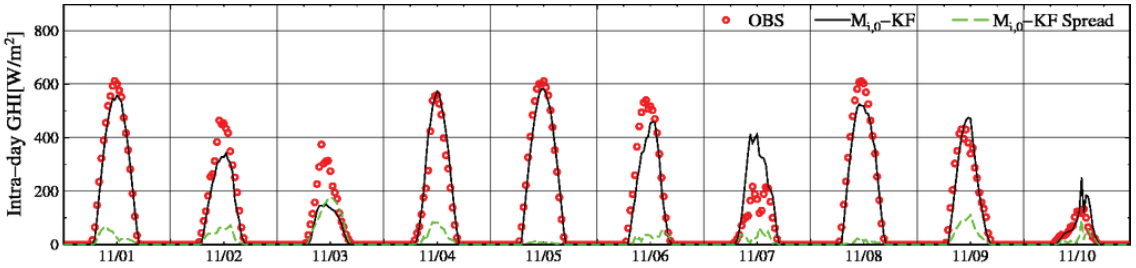

(a2') $M_{i,0}-KF$ and Spread

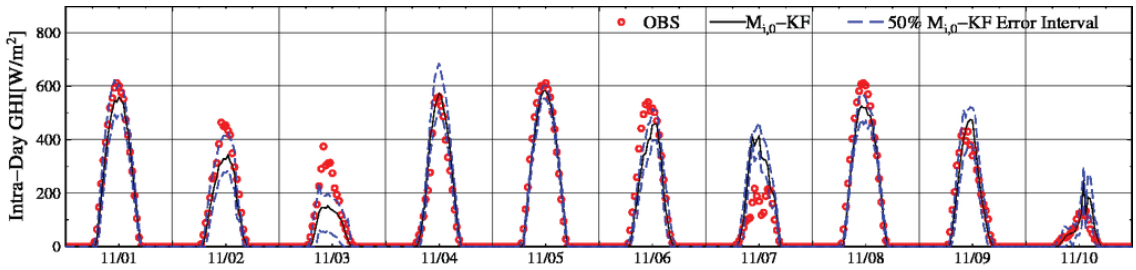

(b2') $M_{i,0}-KF$ and 50% prediction interval

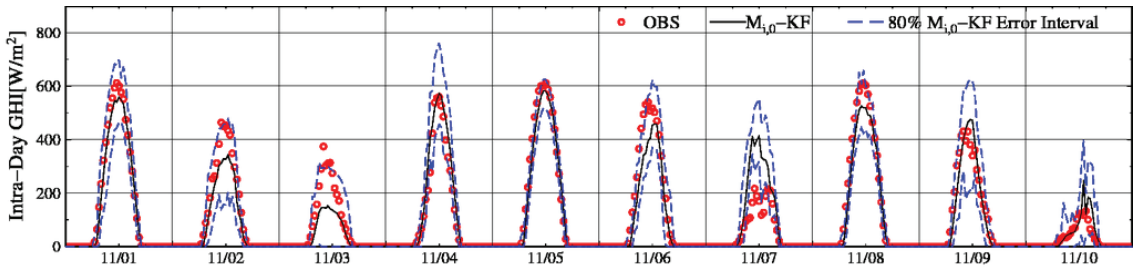

(c2') $M_{i,0}-KF$ and 80% prediction interval

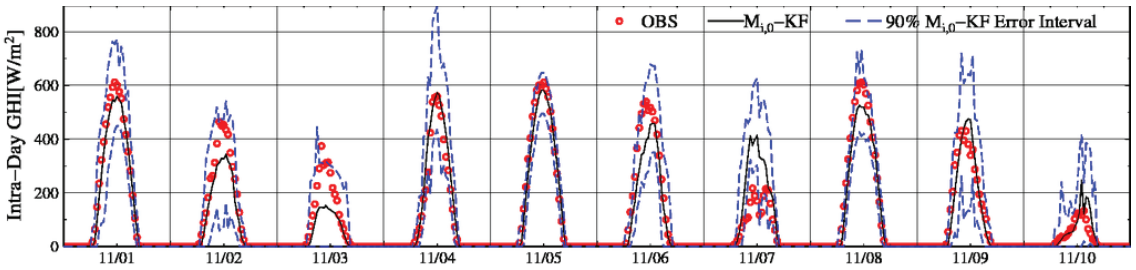

(d2') $M_{i,0}-KF$ and 90% prediction interval

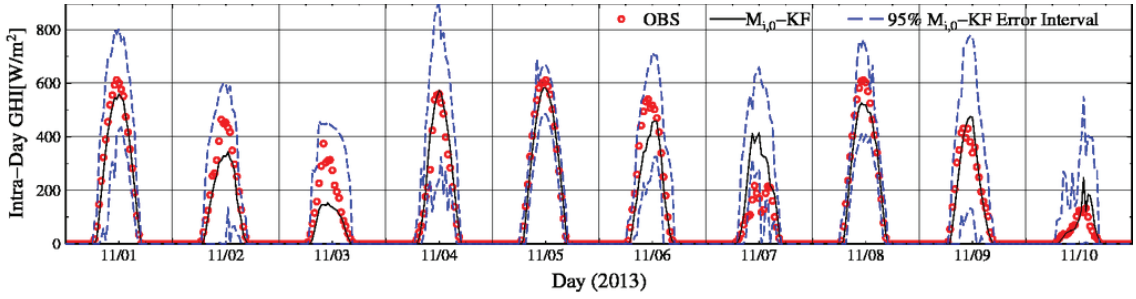

(e2') $M_{i,0}-KF$ and 95% prediction interval

Fig. B.2 Time series of observed and forecasted solar irradiance (GHI) and its 50%, 80%, 90%, 95% prediction interval for the intra-day forecasting $M_{i,0}-KF$ (61 observation-point average, from Nov 1st to 10th, 2013)

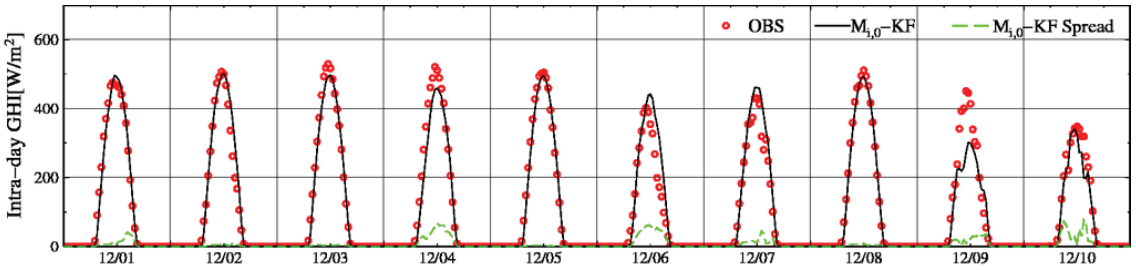

(a3') $M_{i,0}-KF$ and Spread

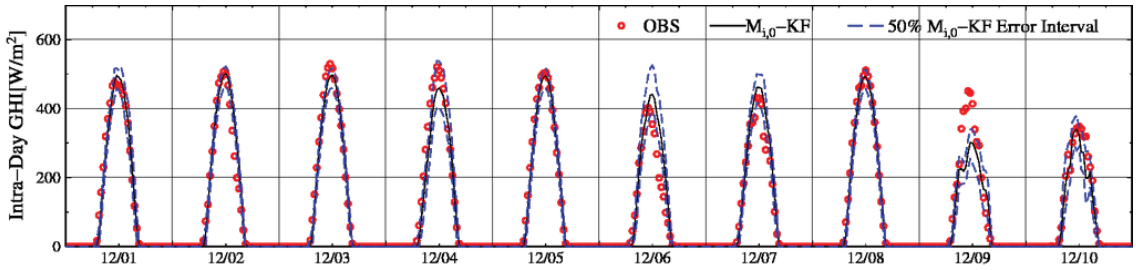

(b3') $M_{i,0}-KF$ and 50% prediction interval

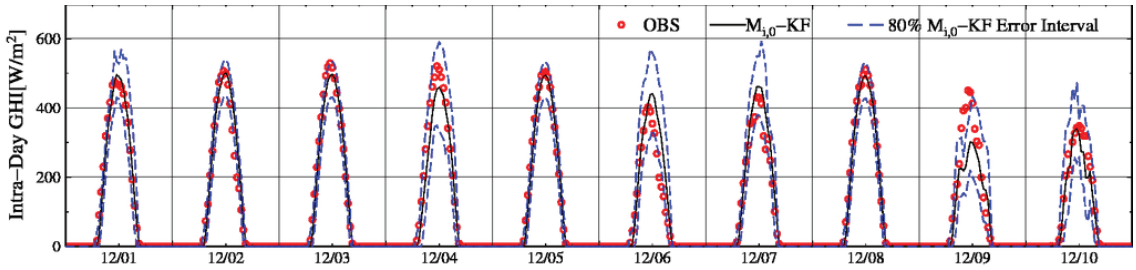

(c3') $M_{i,0}-KF$ and 80% prediction interval

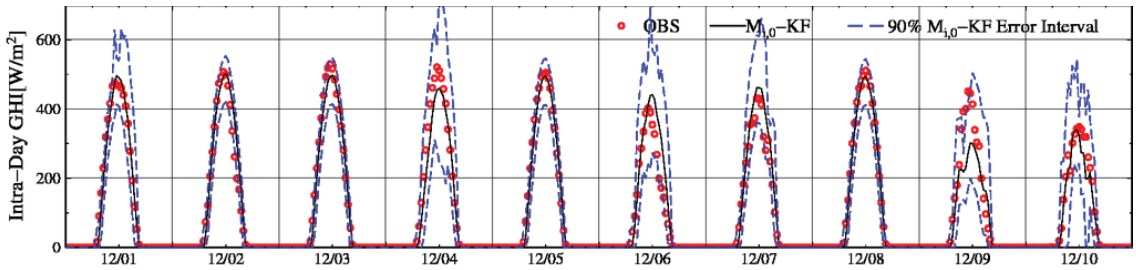

(d3') $M_{i,0}-KF$ and 90% prediction interval

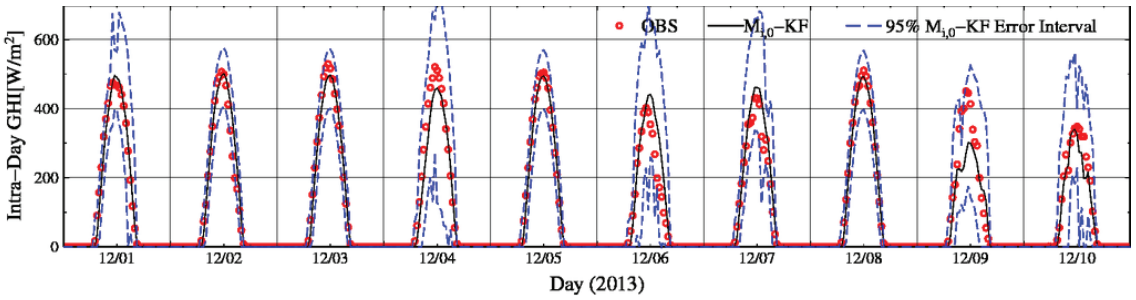

(e3') $M_{i,0}-KF$ and 95% prediction interval

Fig. B.3 Time series of observed and forecasted solar irradiance (GHI) and its 50%, 80%, 90%, 95% prediction interval for the intra-day forecasting $M_{i,0}-KF$ (61 observation-point average, from Dec 1st to 10th, 2013)

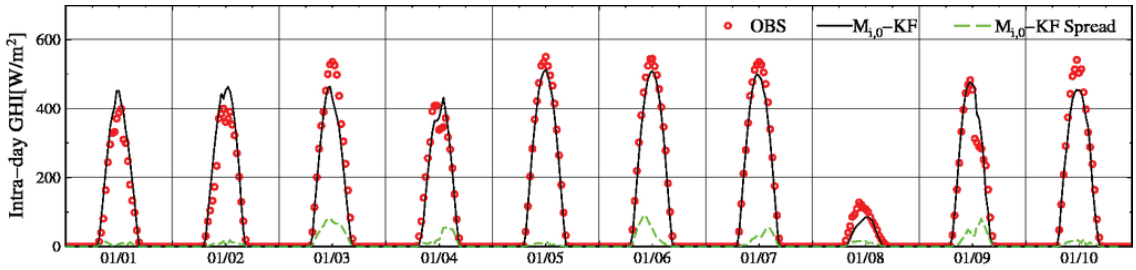

(a4') $M_{i,0}-KF$ and Spread

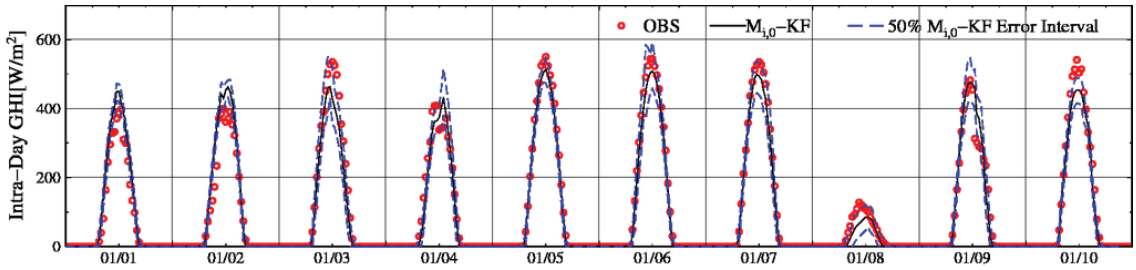

(b4') $M_{i,0}-KF$ and 50% prediction interval

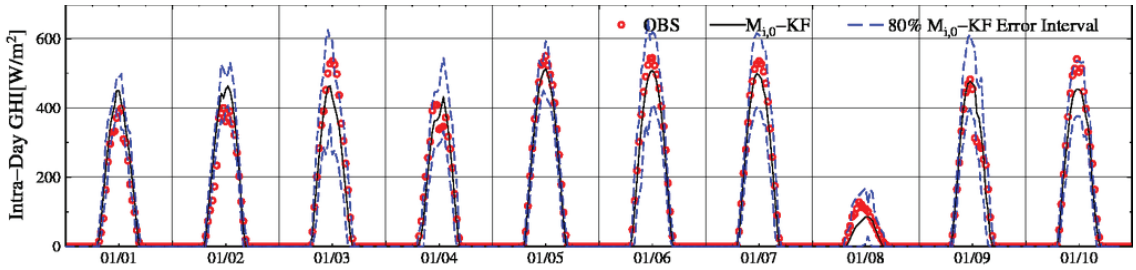

(c4') $M_{i,0}-KF$ and 80% prediction interval

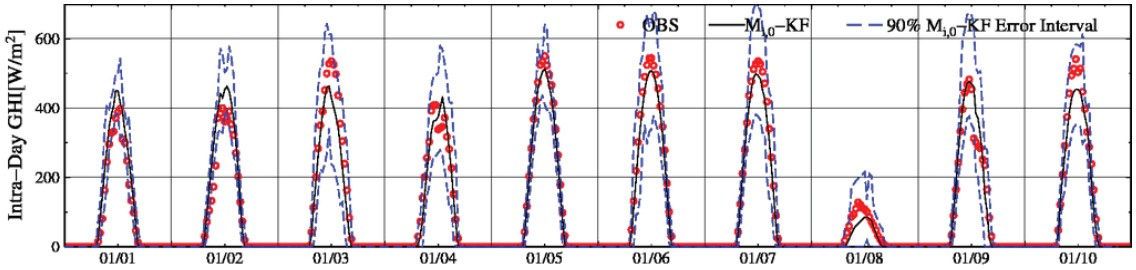

(d4') $M_{i,0}-KF$ and 90% prediction interval

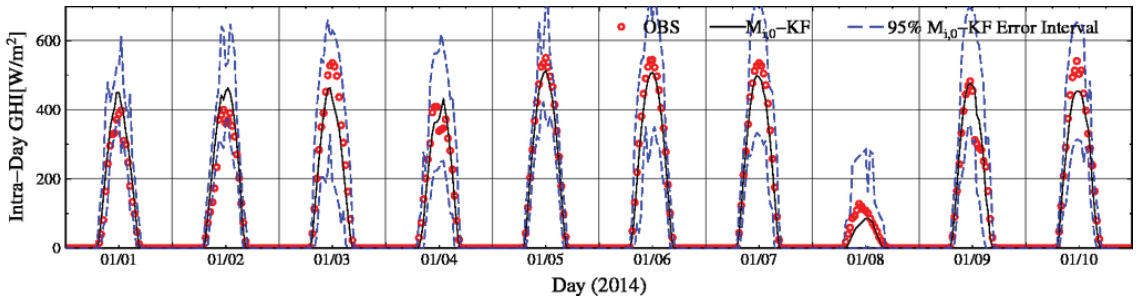

(e4') $M_{i,0}-KF$ and 95% prediction interval

Fig. B.4 Time series of observed and forecasted solar irradiance (GHI) and its 50%, 80%, 90%, 95% prediction interval for the intra-day forecasting $M_{i,0}-KF$ (61 observation-point average, from Jan 1st to 10th, 2014)

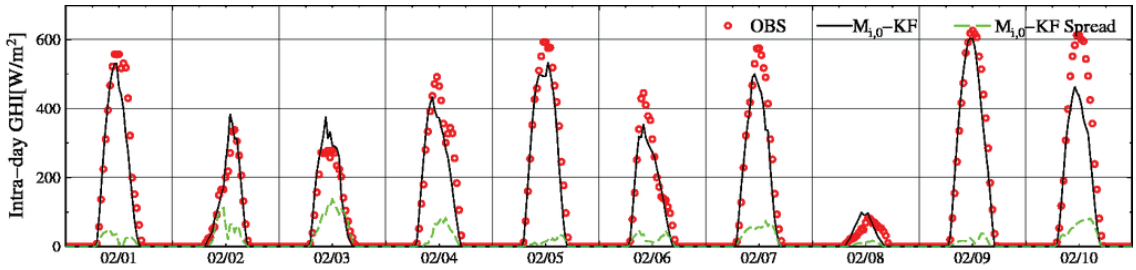

(a5') $M_{i,0}-KF$ and Spread

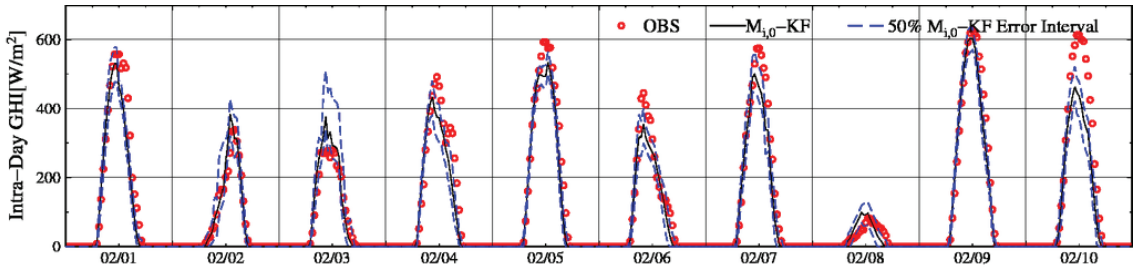

(b5') $M_{i,0}-KF$ and 50% prediction interval

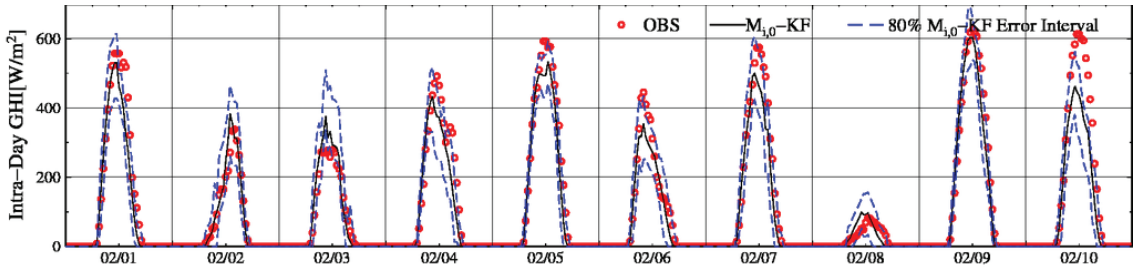

(c5') $M_{i,0}-KF$ and 80% prediction interval

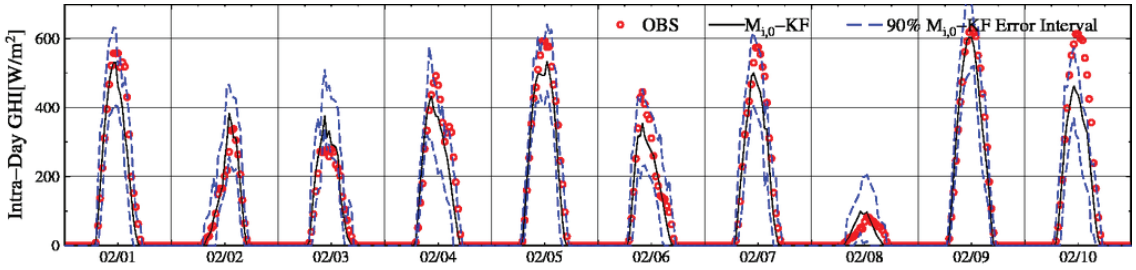

(d5') $M_{i,0}-KF$ and 90% prediction interval

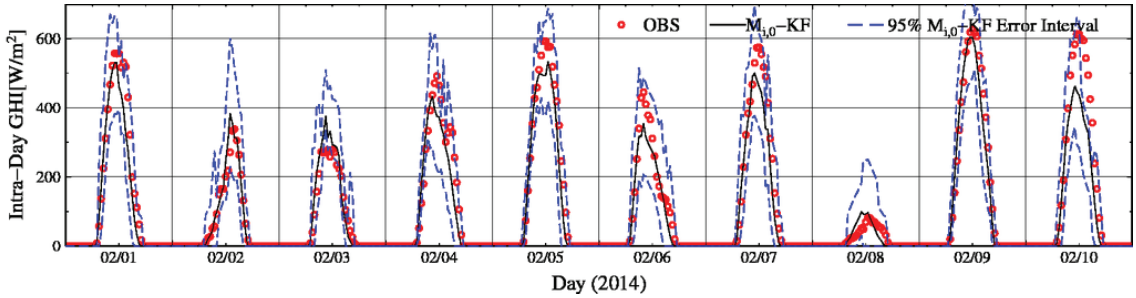

(e5') $M_{i,0}-KF$ and 95% prediction interval

Fig. B.5 Time series of observed and forecasted solar irradiance (GHI) and its 50%, 80%, 90%, 95% prediction interval for the intra-day forecasting $M_{i,0}-KF$ (61 observation-point average, from Feb 1st to 10th, 2014)

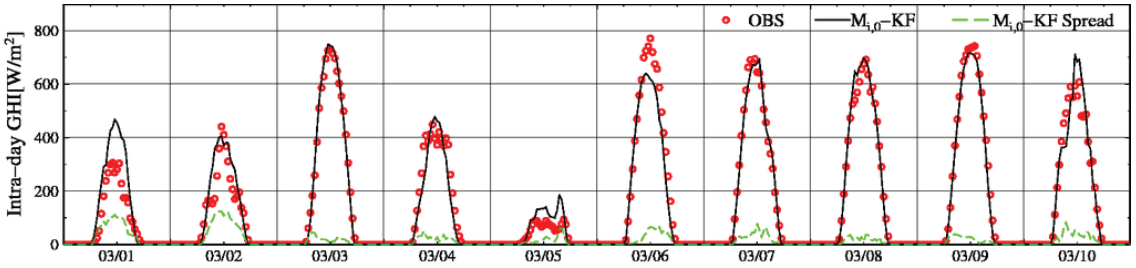

(a6') $M_{i,0}-KF$ and Spread

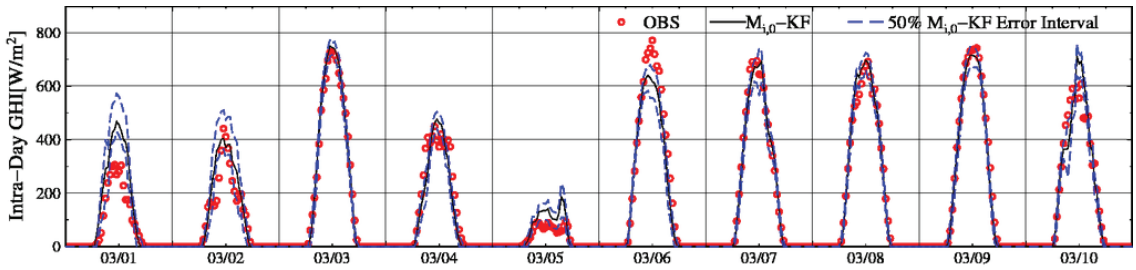

(b6') $M_{i,0}-KF$ and 50% prediction interval

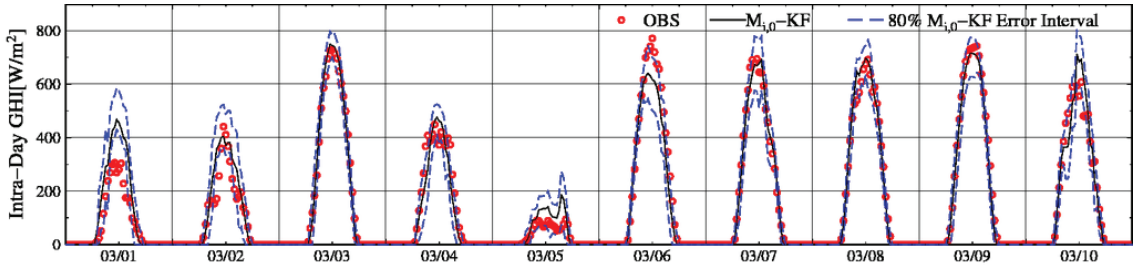

(c6') $M_{i,0}-KF$ and 80% prediction interval

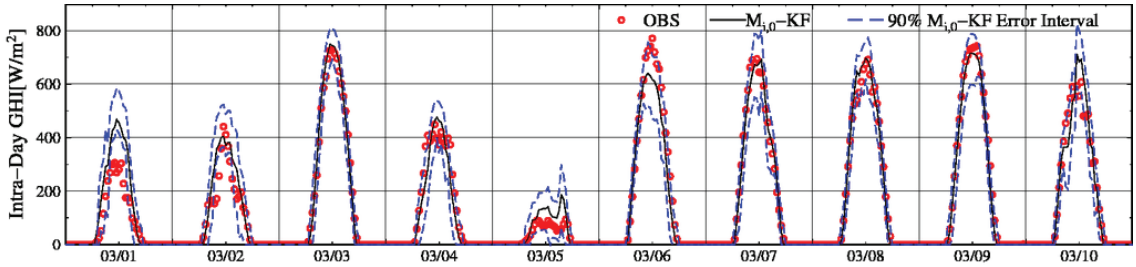

(d6') $M_{i,0}-KF$ and 90% prediction interval

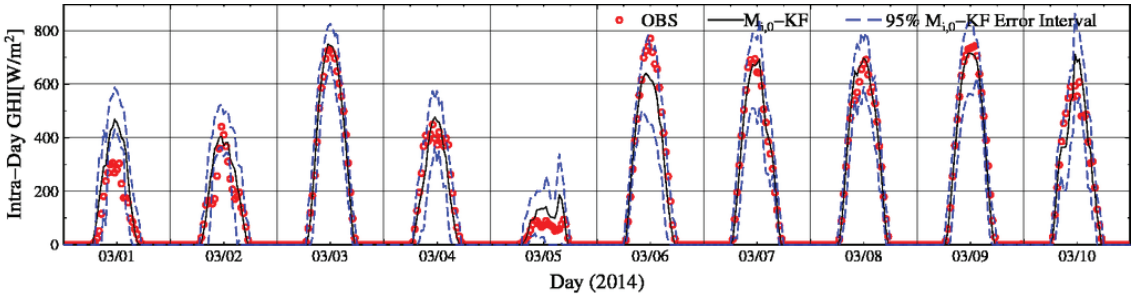

(e6') $M_{i,0}-KF$ and 95% prediction interval

Fig. B.6 Time series of observed and forecasted solar irradiance (GHI) and its 50%, 80%, 90%, 95% prediction interval for the intra-day forecasting $M_{i,0}-KF$ (61 observation-point average, from Mar 1st to 10th, 2014)

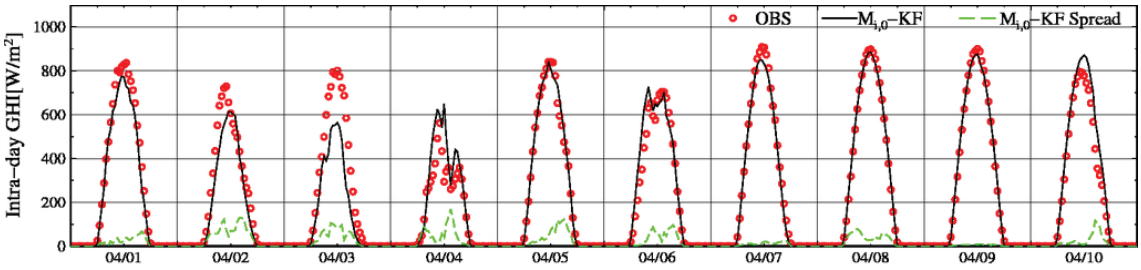

(a7') $M_{i,0}-KF$ and Spread

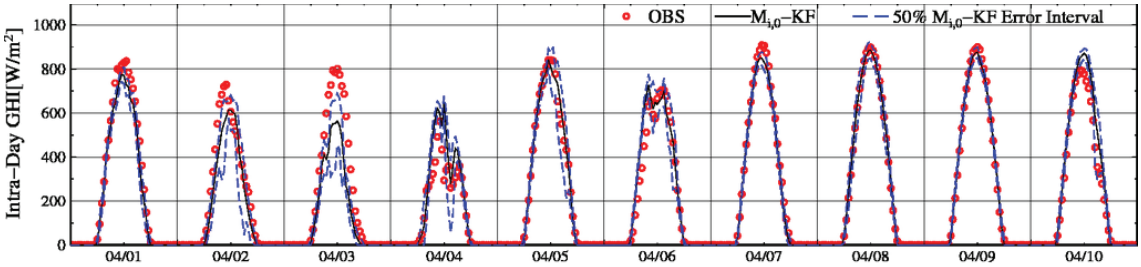

(b7') $M_{i,0}-KF$ and 50% prediction interval

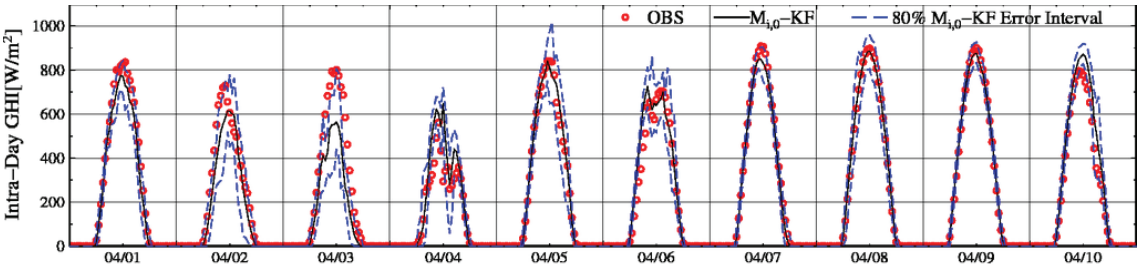

(c7') $M_{i,0}-KF$ and 80% prediction interval

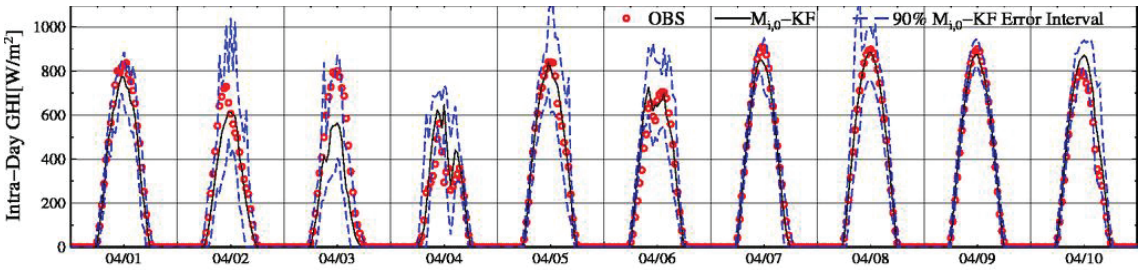

(d7') $M_{i,0}-KF$ and 90% prediction interval

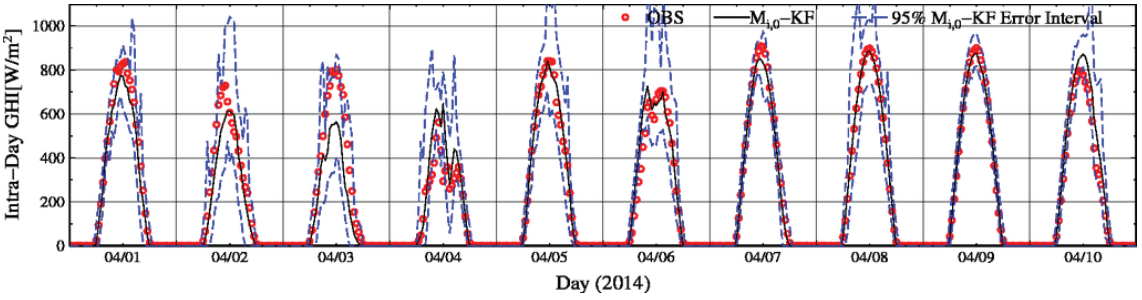

(e7') $M_{i,0}-KF$ and 95% prediction interval

Fig. B.7 Time series of observed and forecasted solar irradiance (GHI) and its 50%, 80%, 90%, 95% prediction interval for the intra-day forecasting $M_{i,0}-KF$ (61 observation-point average, from Apr 1st to 10th, 2014)

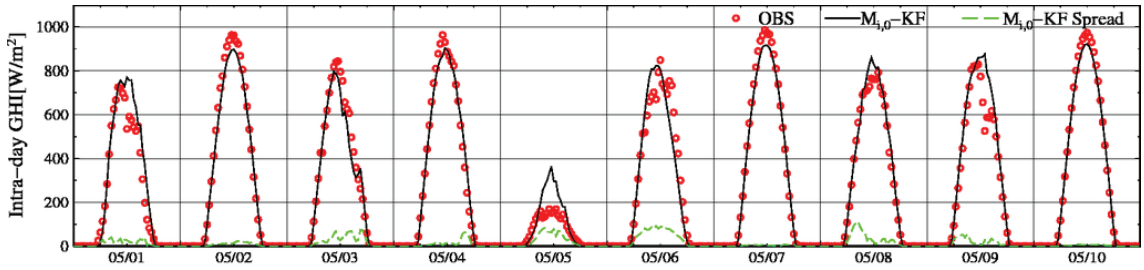

(a8') $M_{i,0}-KF$ and Spread

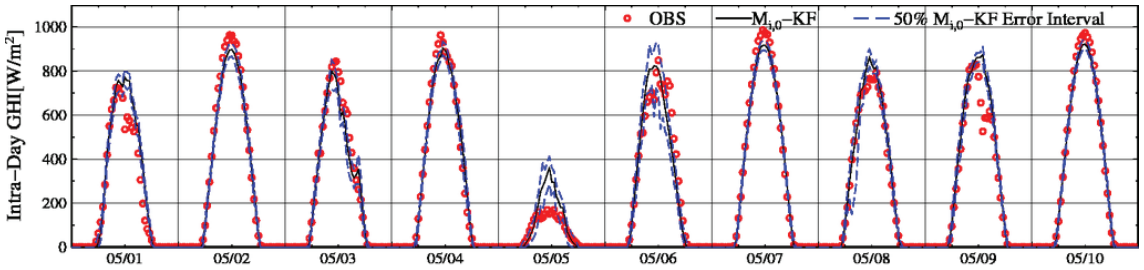

(b8') $M_{i,0}-KF$ and 50% prediction interval

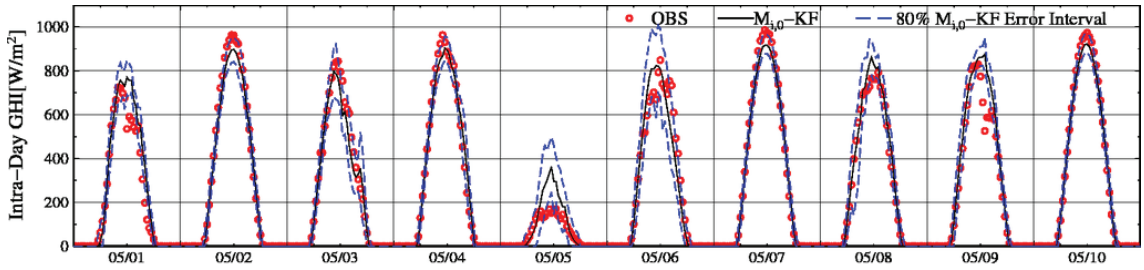

(c8') $M_{i,0}-KF$ and 80% prediction interval

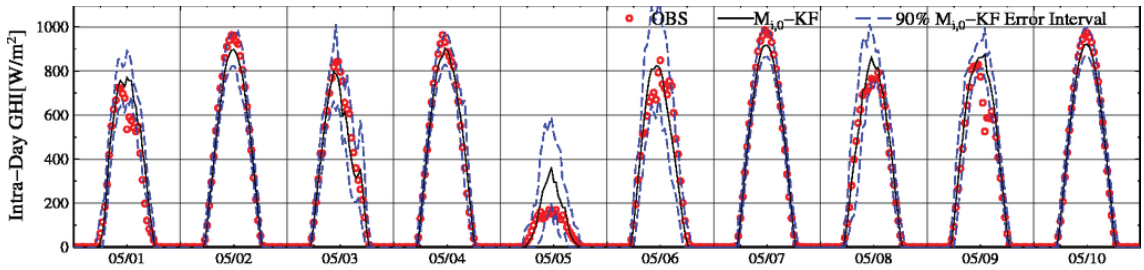

(d8') $M_{i,0}-KF$ and 90% prediction interval

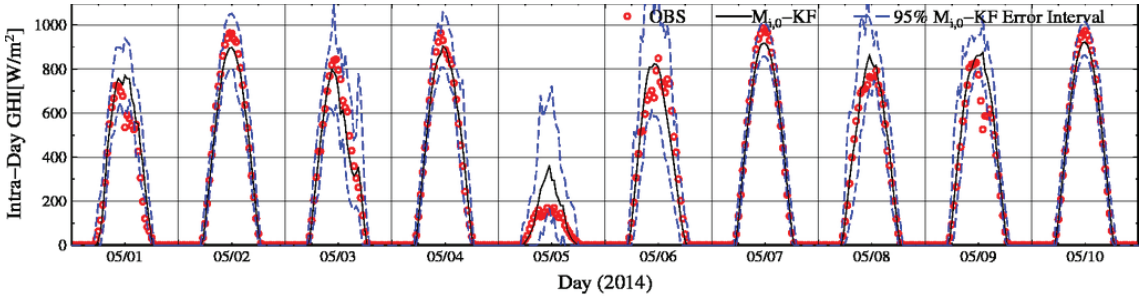

(e8') $M_{i,0}-KF$ and 95% prediction interval

Fig. B.8 Time series of observed and forecasted solar irradiance (GHI) and its 50%, 80%, 90%, 95% prediction interval for the intra-day forecasting $M_{i,0}-KF$ (61 observation-point average, from May 1st to 10th, 2014)

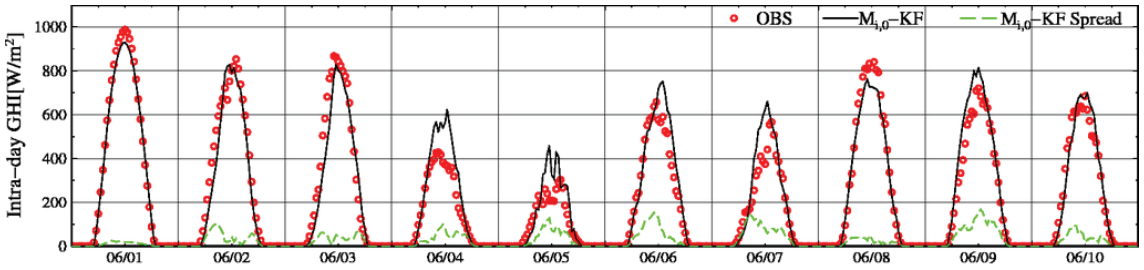

(a9') $M_{i,0}-KF$ and Spread

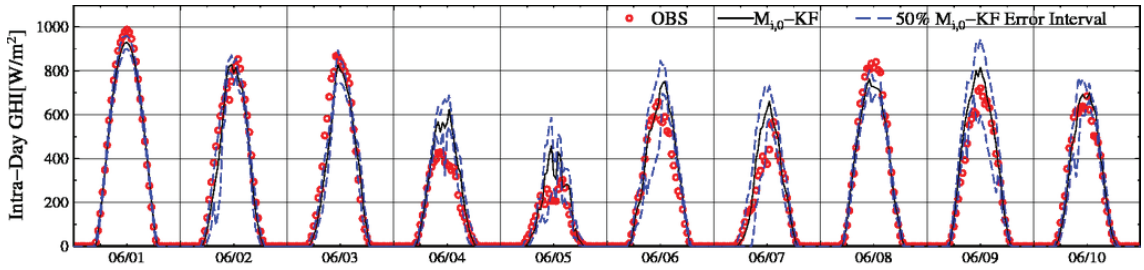

(b9') $M_{i,0}-KF$ and 50% prediction interval

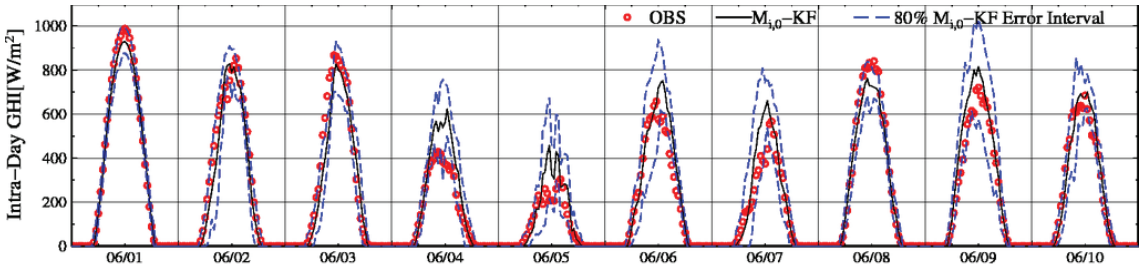

(c9') $M_{i,0}-KF$ and 80% prediction interval

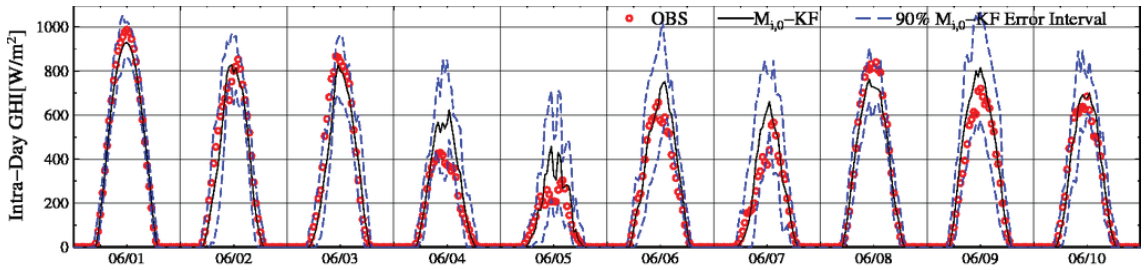

(d9') $M_{i,0}-KF$ and 90% prediction interval

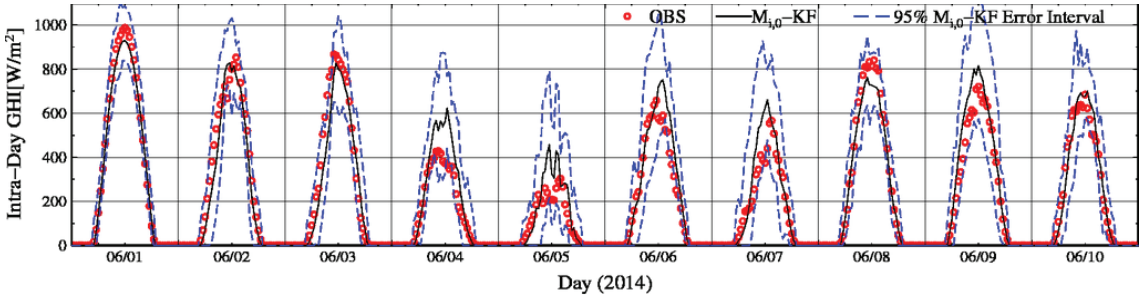

(e9') $M_{i,0}-KF$ and 95% prediction interval

Fig. B.9 Time series of observed and forecasted solar irradiance (GHI) and its 50%, 80%, 90%, 95% prediction interval for the intra-day forecasting $M_{i,0}-KF$ (61 observation-point average, from Jun 1st to 10th, 2014)

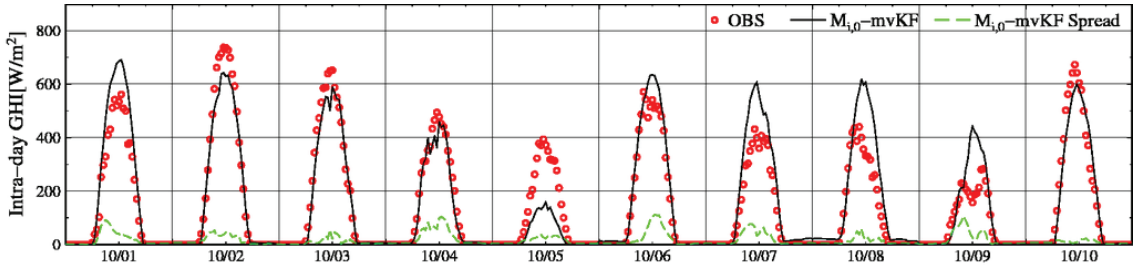

(a1") $M_{i,0}-mvKF$ and Spread

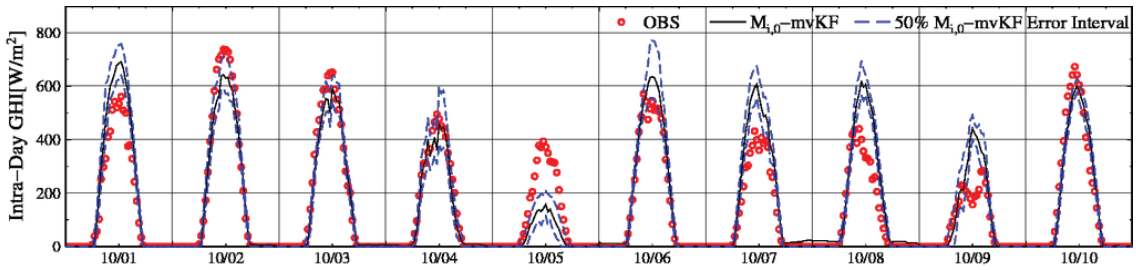

(b1") $M_{i,0}-mvKF$ and 50% prediction interval

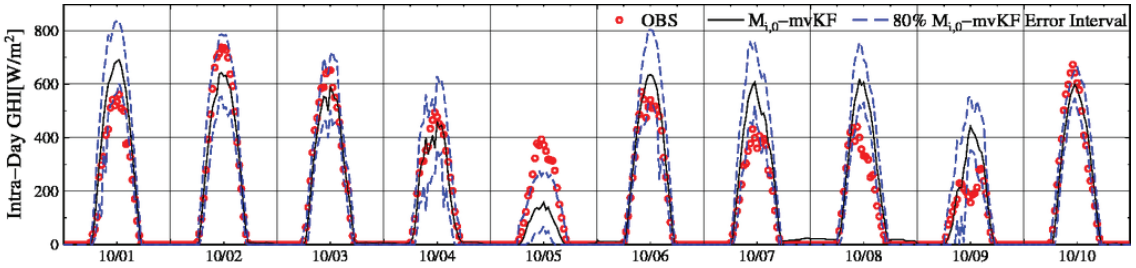

(c1") $M_{i,0}-mvKF$ and 80% prediction interval

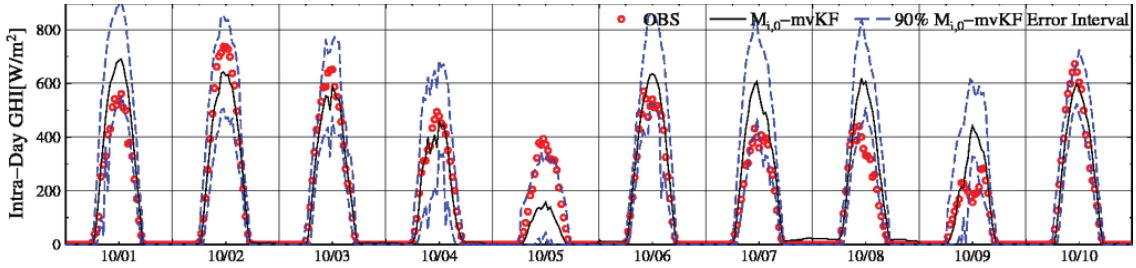

(d1") $M_{i,0}-mvKF$ and 90% prediction interval

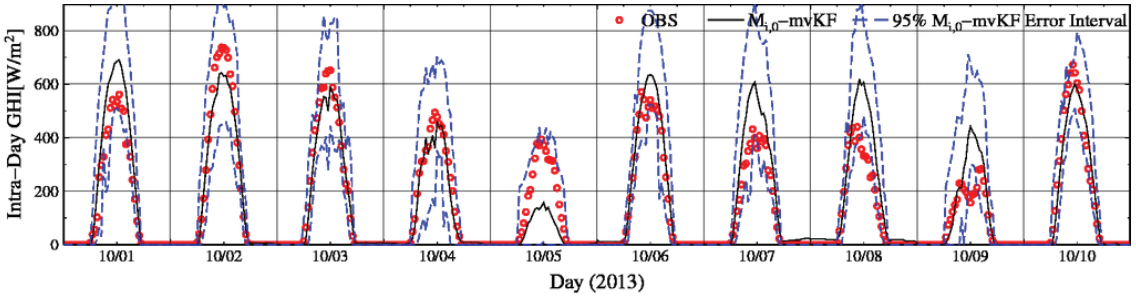

(e1") $M_{i,0}-mvKF$ and 95% prediction interval

Fig. C.1 Time series of observed and forecasted solar irradiance (GHI) and its 50%, 80%, 90%, 95% prediction interval for the intra-day forecasting $M_{i,0}-mvKF$ (61 observation-point average, from Oct 1st to 10th, 2013)

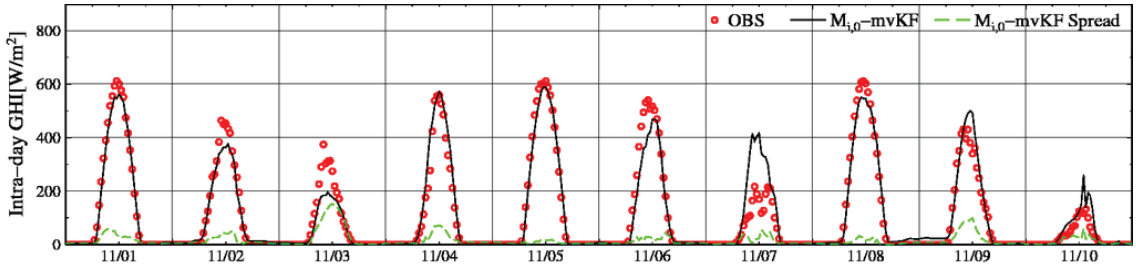

(a2") $M_{i,0}-mvKF$ and Spread

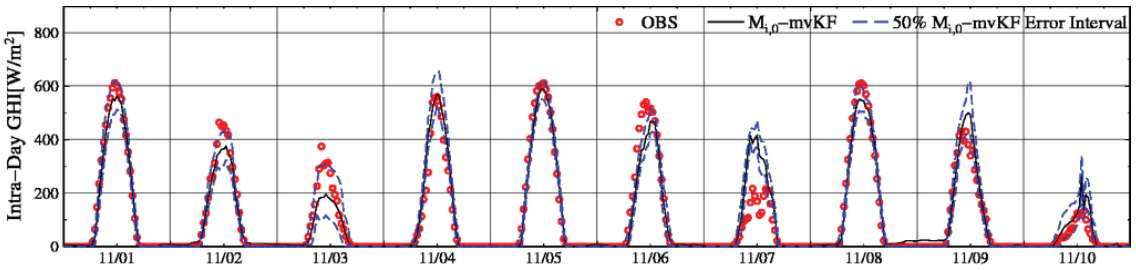

(b2") $M_{i,0}-mvKF$ and 50% prediction interval

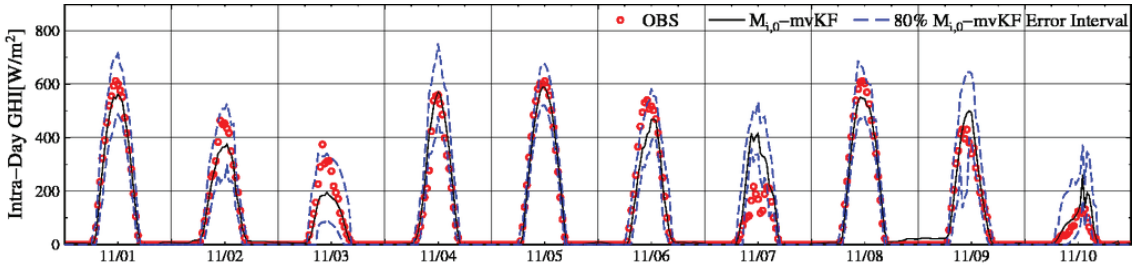

(c2") $M_{i,0}-mvKF$ and 80% prediction interval

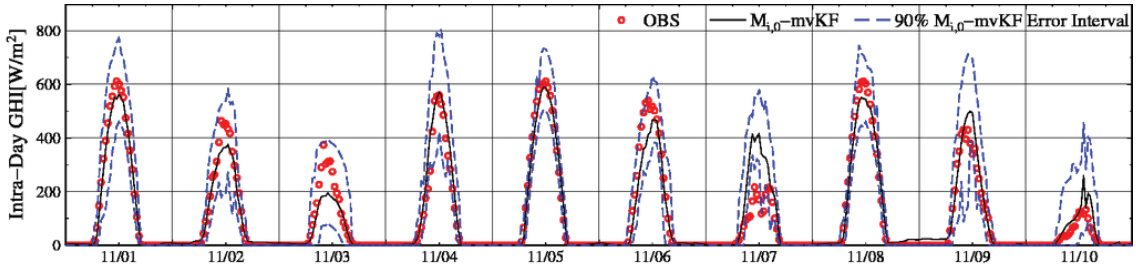

(d2") $M_{i,0}-mvKF$ and 90% prediction interval

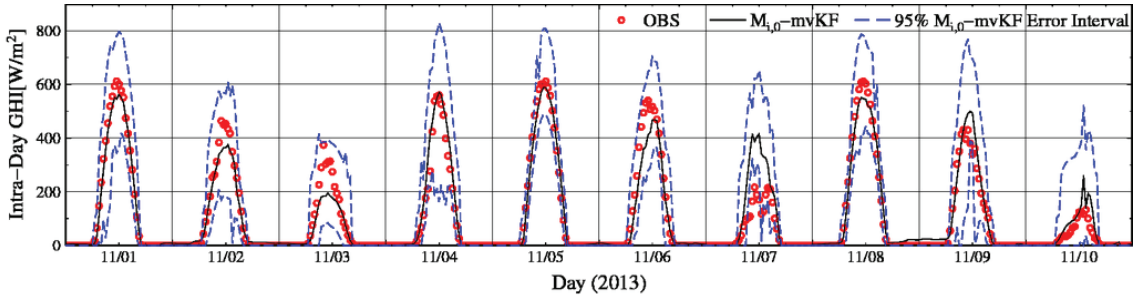

(e2") $M_{i,0}-mvKF$ and 95% prediction interval

Fig. C.2 Time series of observed and forecasted solar irradiance (GHI) and its 50%, 80%, 90%, 95% prediction interval for the intra-day forecasting $M_{i,0}-mvKF$ (61 observation-point average, from Nov 1st to 10th, 2013)

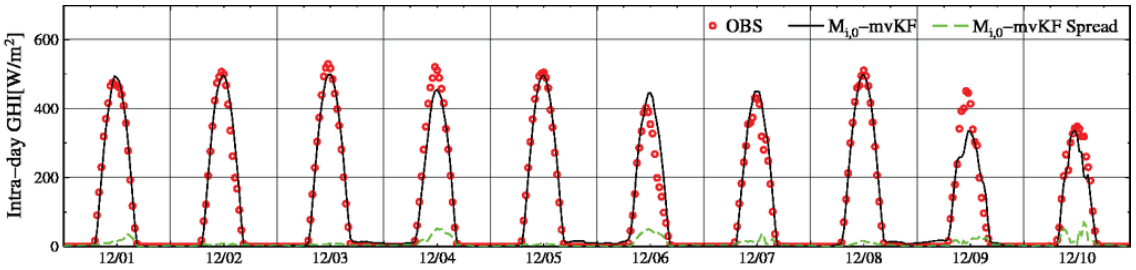

(a3") $M_{i,0}-mvKF$ and Spread

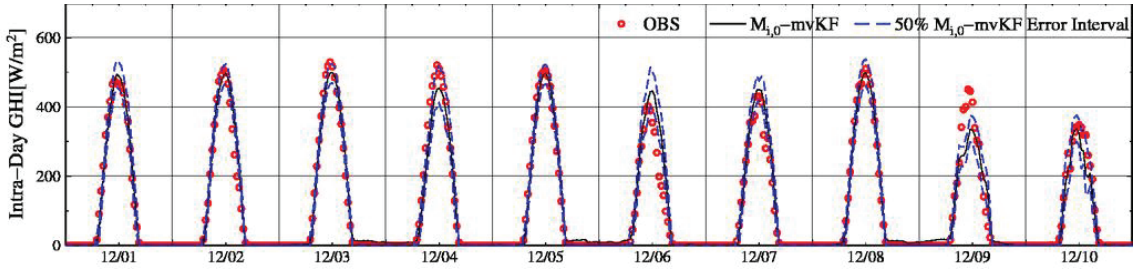

(b3") $M_{i,0}-mvKF$ and 50% prediction interval

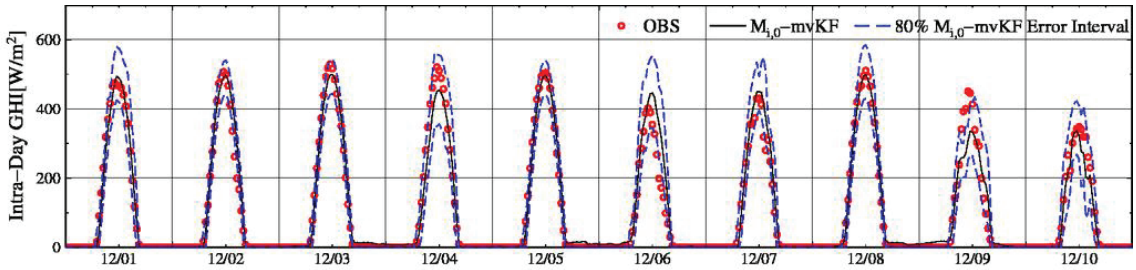

(c3") $M_{i,0}-mvKF$ and 80% prediction interval

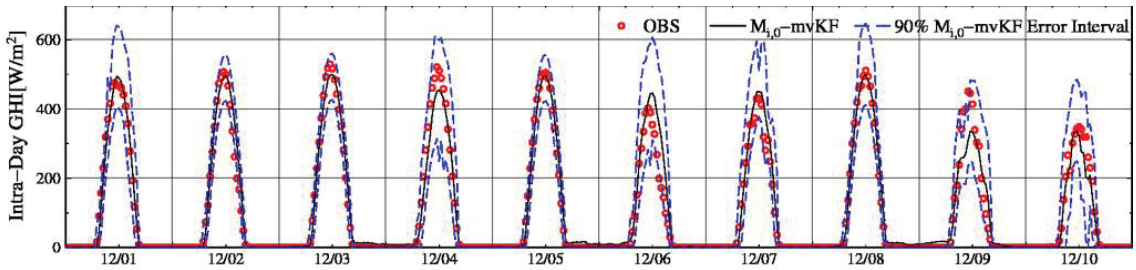

(d3") $M_{i,0}-mvKF$ and 90% prediction interval

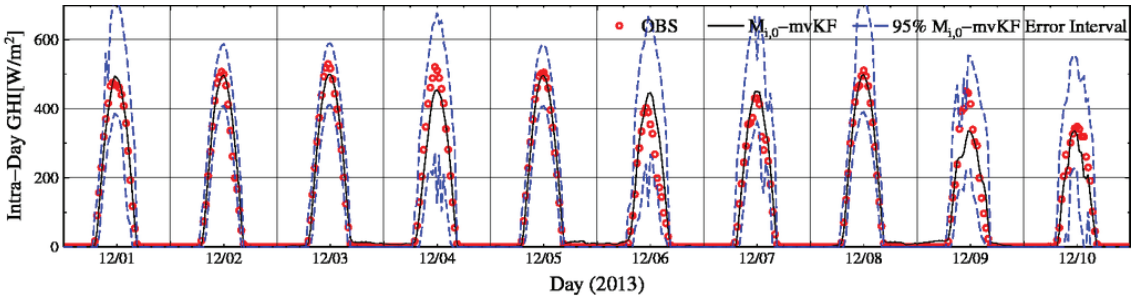

(e3") $M_{i,0}-mvKF$ and 95% prediction interval

Fig. C.3 Time series of observed and forecasted solar irradiance (GHI) and its 50%, 80%, 90%, 95% prediction interval for the intra-day forecasting $M_{i,0}-mvKF$ (61 observation-point average, from Dec 1st to 10th, 2013)

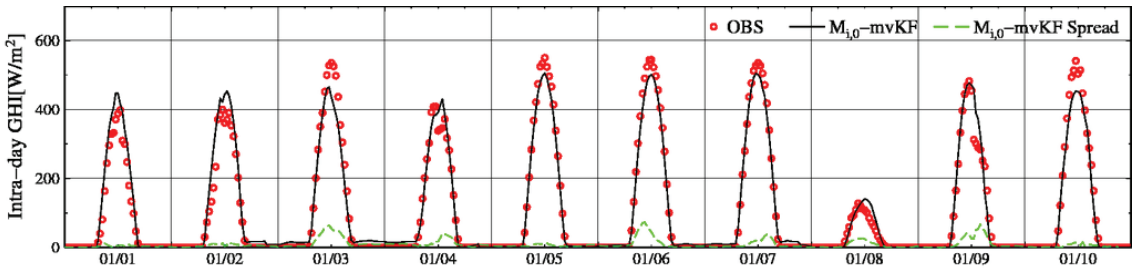

(a4") $M_{i,0}-mvKF$ and Spread

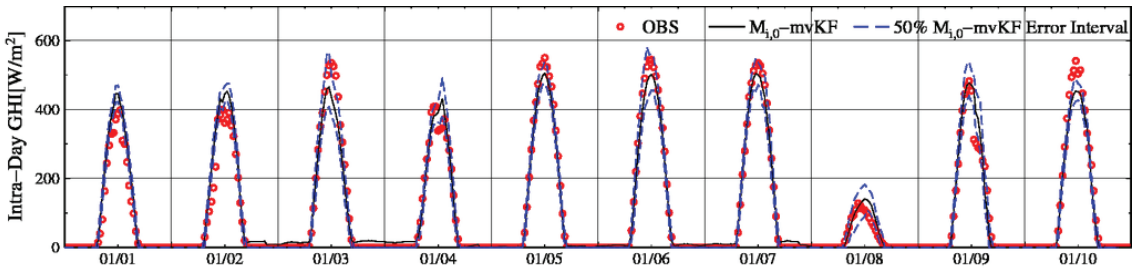

(b4") $M_{i,0}-mvKF$ and 50% prediction interval

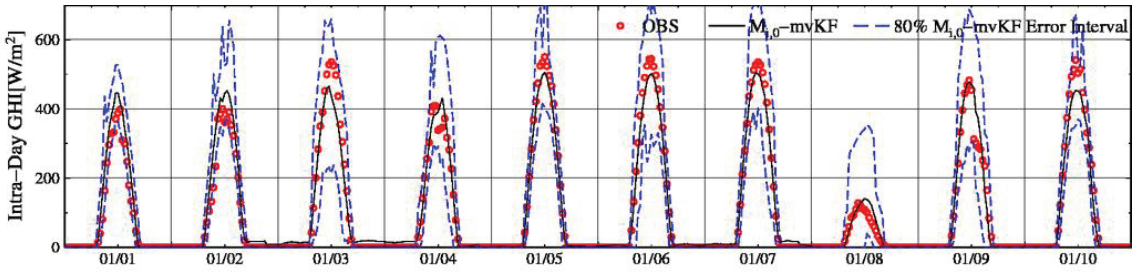

(c4") $M_{i,0}-mvKF$ and 80% prediction interval

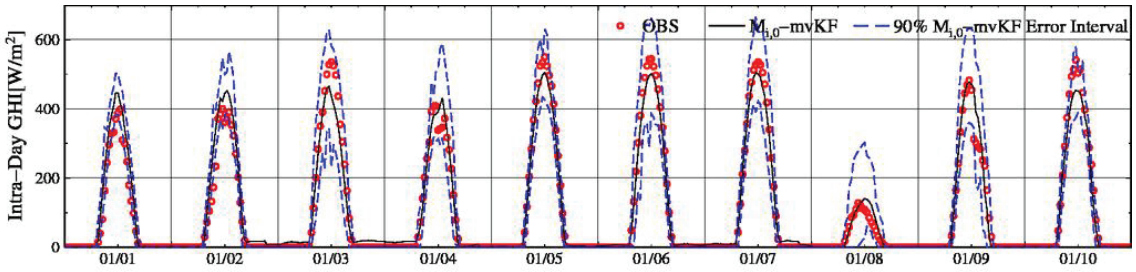

(d4") $M_{i,0}-mvKF$ and 90% prediction interval

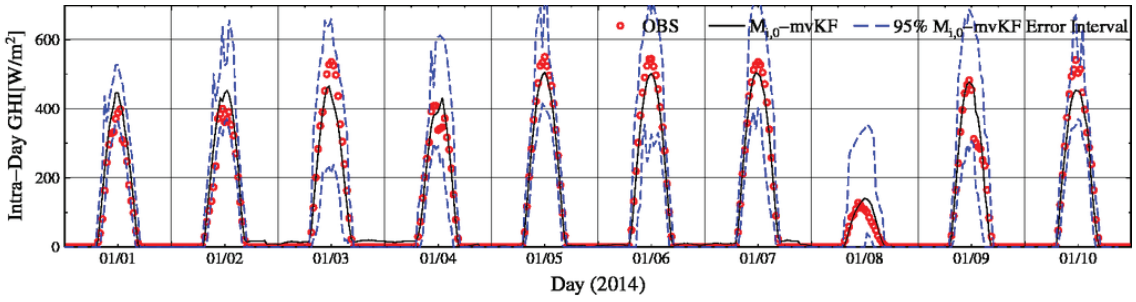

(e4") $M_{i,0}-mvKF$ and 95% prediction interval

Fig. C.4 Time series of observed and forecasted solar irradiance (GHI) and its 50%, 80%, 90%, 95% prediction interval for the intra-day forecasting $M_{i,0}-mvKF$ (61 observation-point average, from Jan 1st to 10th, 2014)

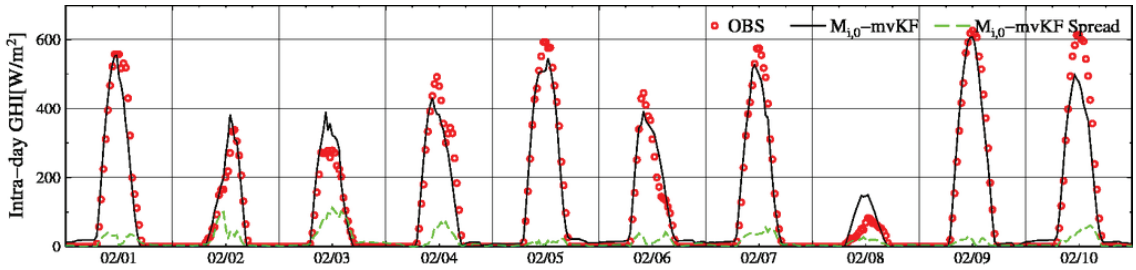

(a5") $M_{i,0}-mvKF$ and Spread

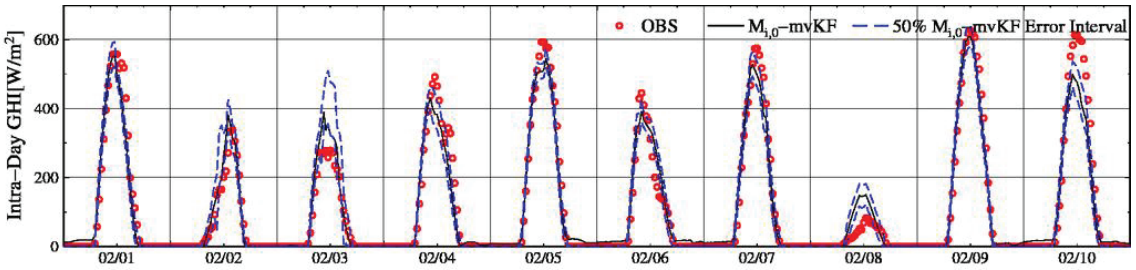

(b5") $M_{i,0}-mvKF$ and 50% prediction interval

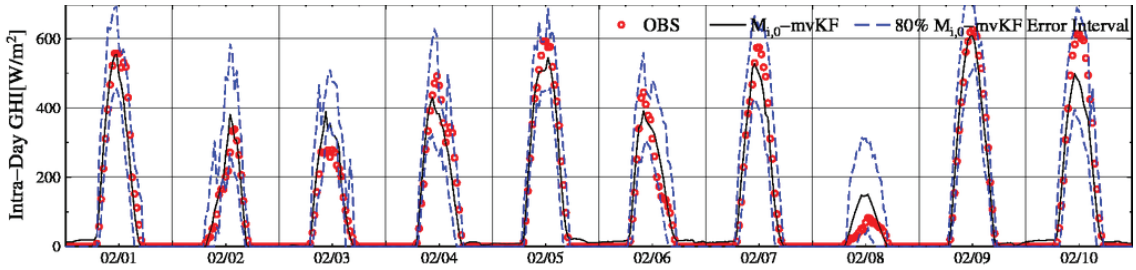

(c5") $M_{i,0}-mvKF$ and 80% prediction interval

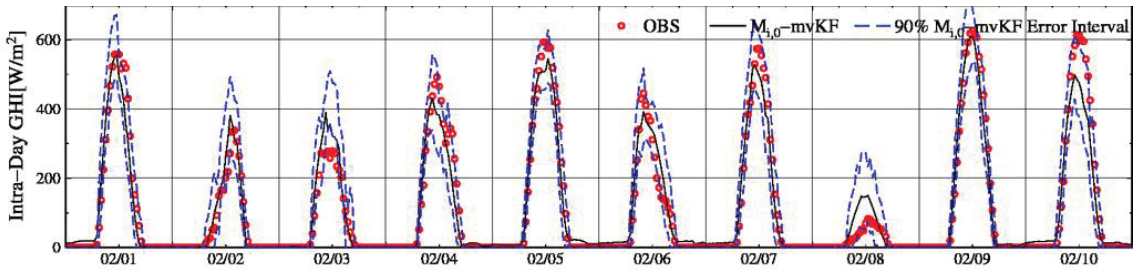

(d5") $M_{i,0}-mvKF$ and 90% prediction interval

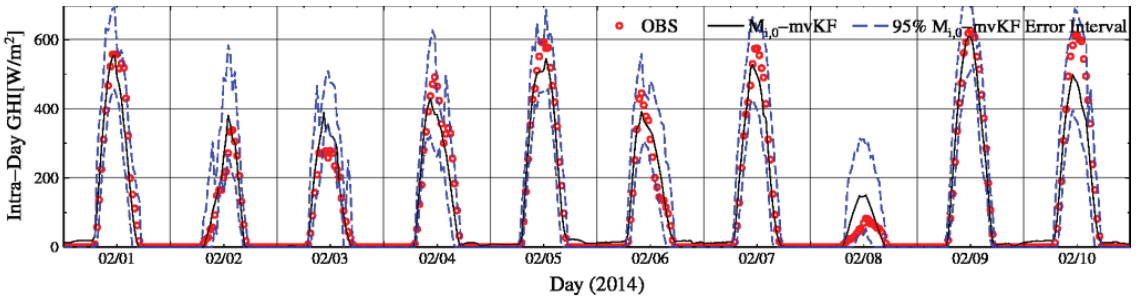

(e5") $M_{i,0}-mvKF$ and 95% prediction interval

Fig. C.5 Time series of observed and forecasted solar irradiance (GHI) and its 50%, 80%, 90%, 95% prediction interval for the intra-day forecasting $M_{i,0}-mvKF$ (61 observation-point average, from Feb 1st to 10th, 2014)

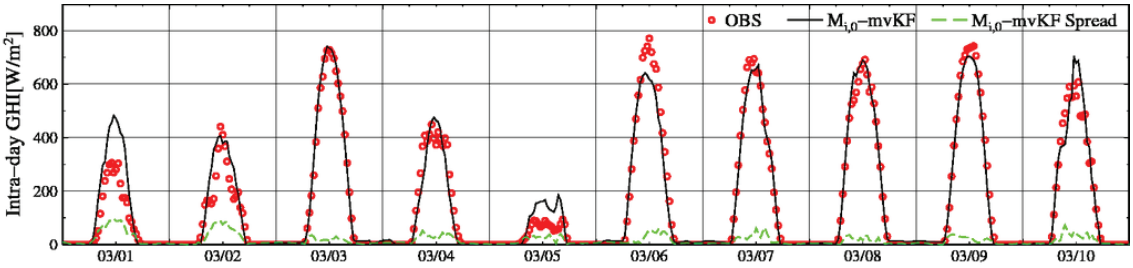

(a6") $M_{i,0}-mvKF$ and Spread

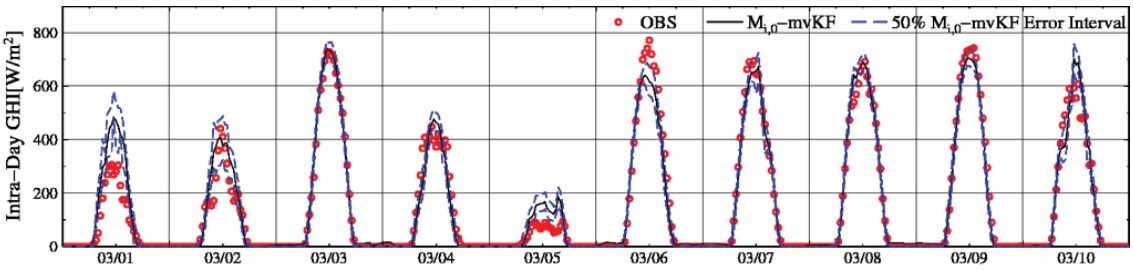

(b6") $M_{i,0}-mvKF$ and 50% prediction interval

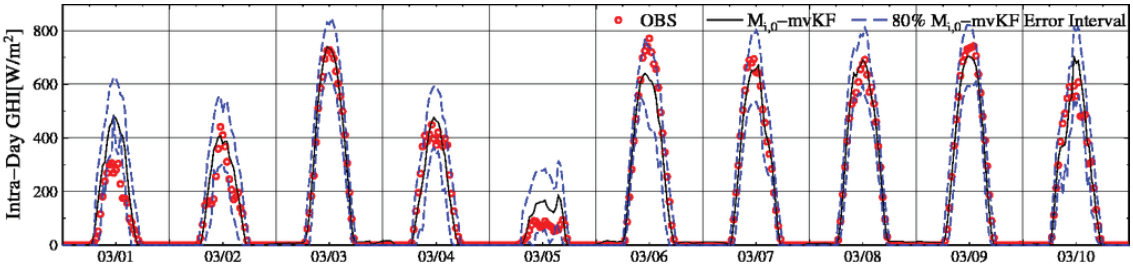

(c6") $M_{i,0}-mvKF$ and 80% prediction interval

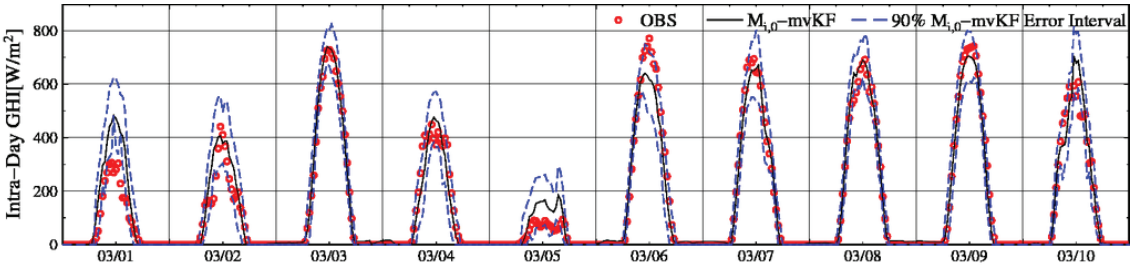

(d6") $M_{i,0}-mvKF$ and 90% prediction interval

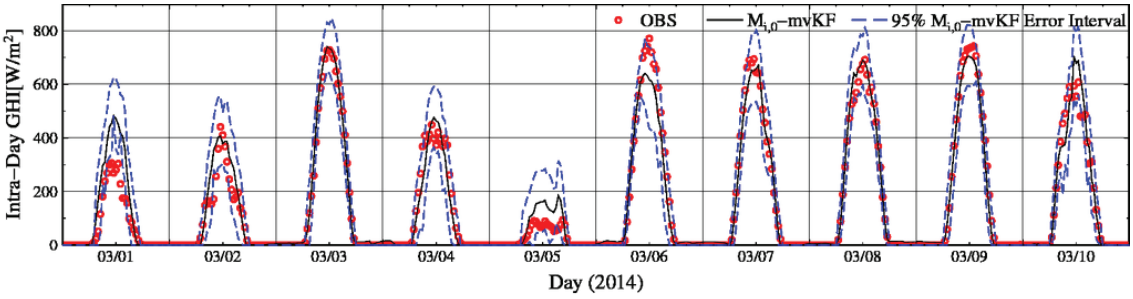

(e6") $M_{i,0}-mvKF$ and 95% prediction interval

Fig. C.6 Time series of observed and forecasted solar irradiance (GHI) and its 50%, 80%, 90%, 95% prediction interval for the intra-day forecasting $M_{i,0}-mvKF$ (61 observation-point average, from Mar 1st to 10th, 2014)

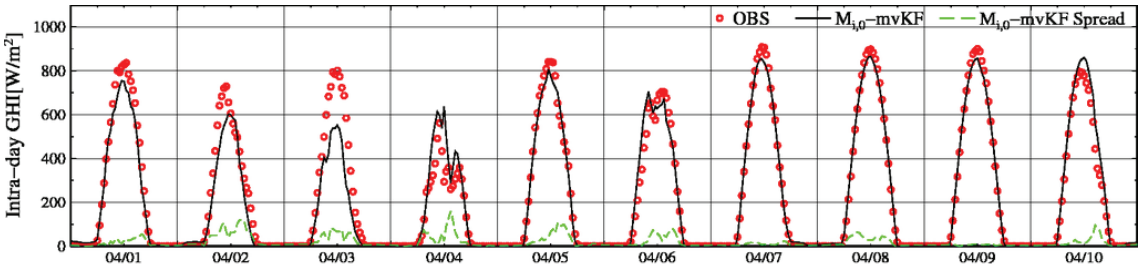

(a7") $M_{i,0}-mvKF$ and Spread

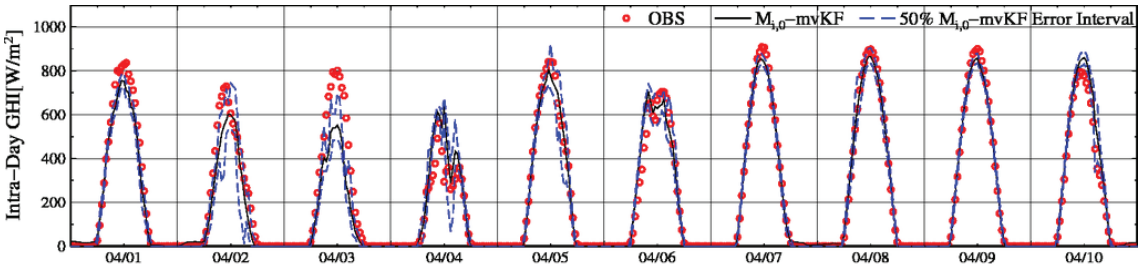

(b7") $M_{i,0}-mvKF$ and 50% prediction interval

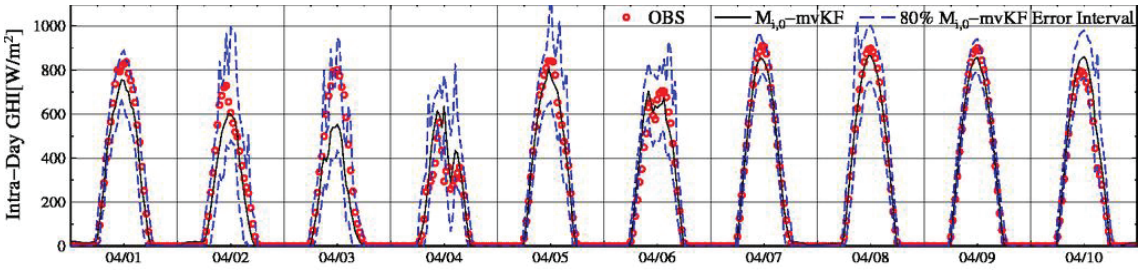

(c7") $M_{i,0}-mvKF$ and 80% prediction interval

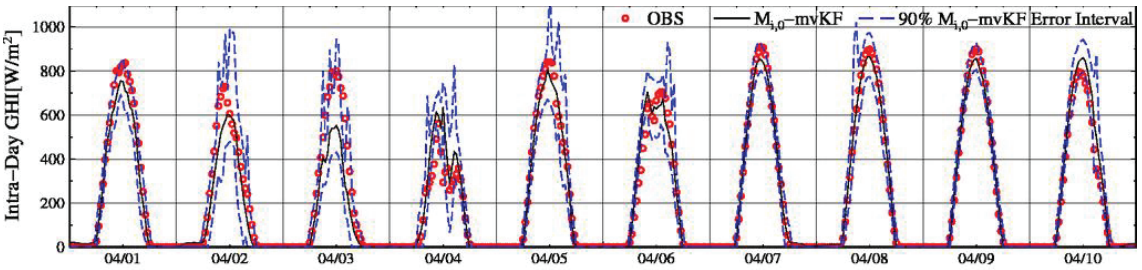

(d7") $M_{i,0}-mvKF$ and 90% prediction interval

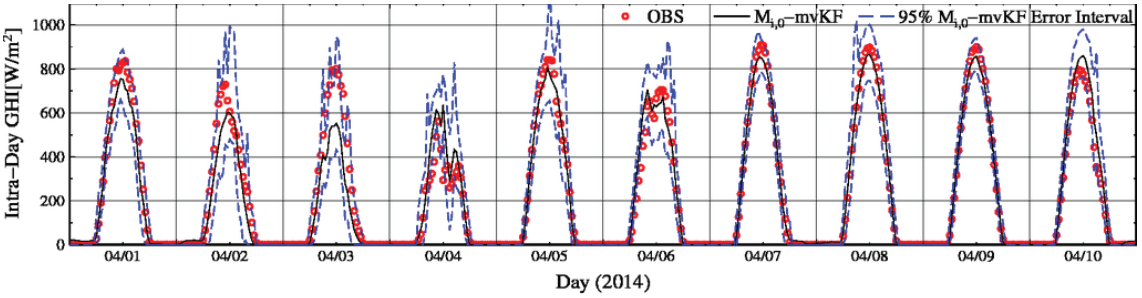

(e7") $M_{i,0}-mvKF$ and 95% prediction interval

Fig. C.7 Time series of observed and forecasted solar irradiance (GHI) and its 50%, 80%, 90%, 95% prediction interval for the intra-day forecasting $M_{i,0}-mvKF$ (61 observation-point average, from Apr 1st to 10th, 2014)

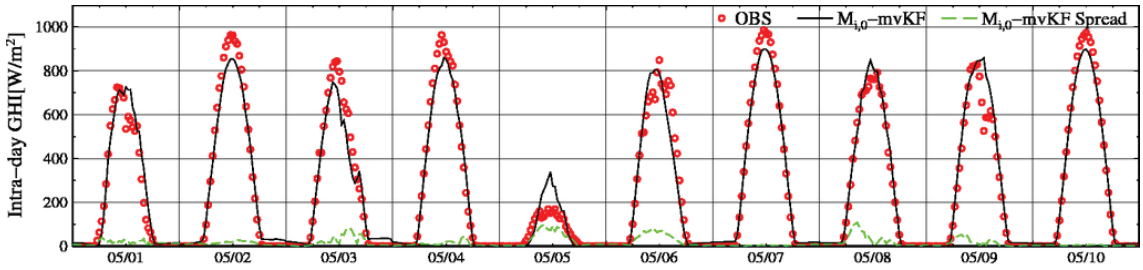

(a8") $M_{i,0}-mvKF$ and Spread

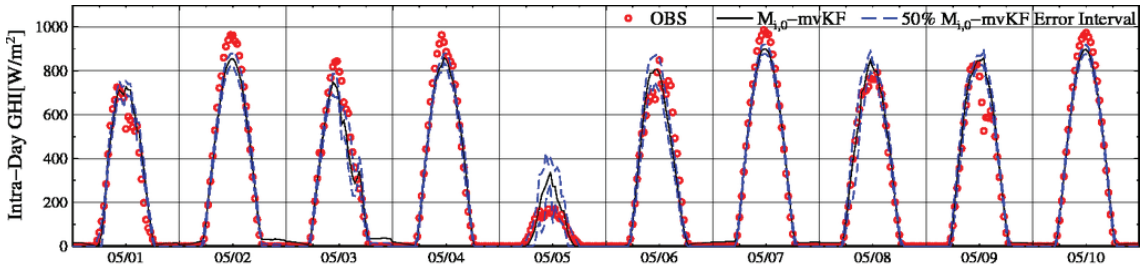

(b8") $M_{i,0}-mvKF$ and 50% prediction interval

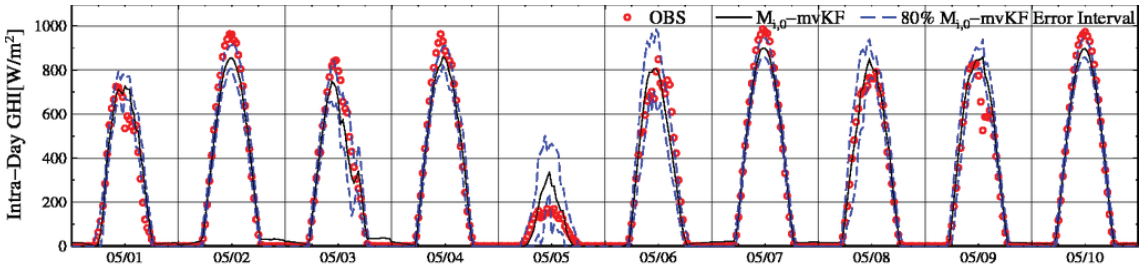

(c8") $M_{i,0}-mvKF$ and 80% prediction interval

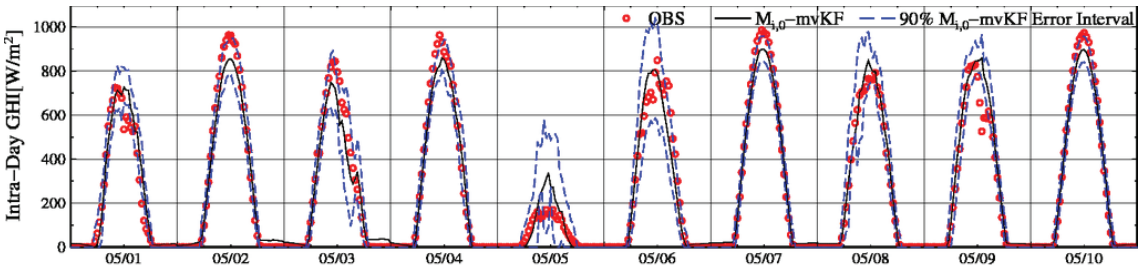

(d8") $M_{i,0}-mvKF$ and 90% prediction interval

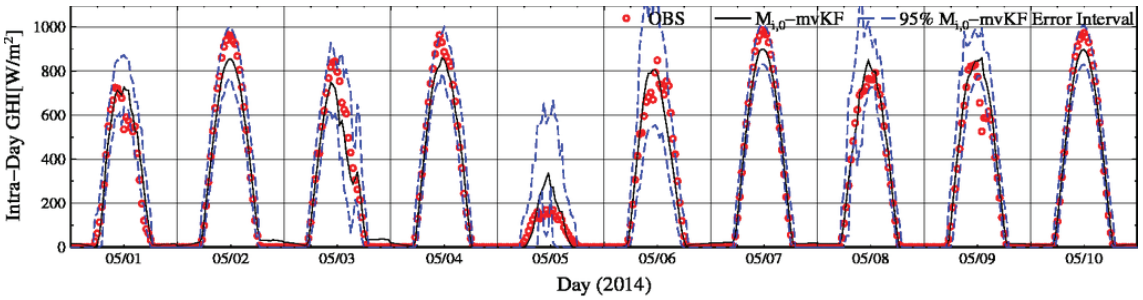

(e8") $M_{i,0}-mvKF$ and 95% prediction interval

Fig. C.8 Time series of observed and forecasted solar irradiance (GHI) and its 50%, 80%, 90%, 95% prediction interval for the intra-day forecasting $M_{i,0}-mvKF$ (61 observation-point average, from May 1st to 10th, 2014)

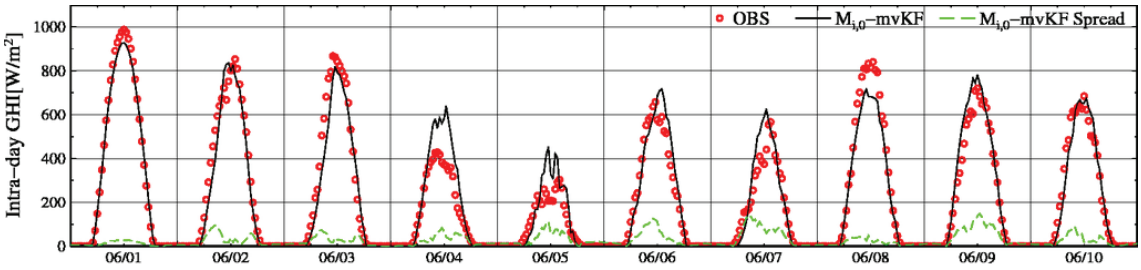

(a9") $M_{i,0}-mvKF$ and Spread

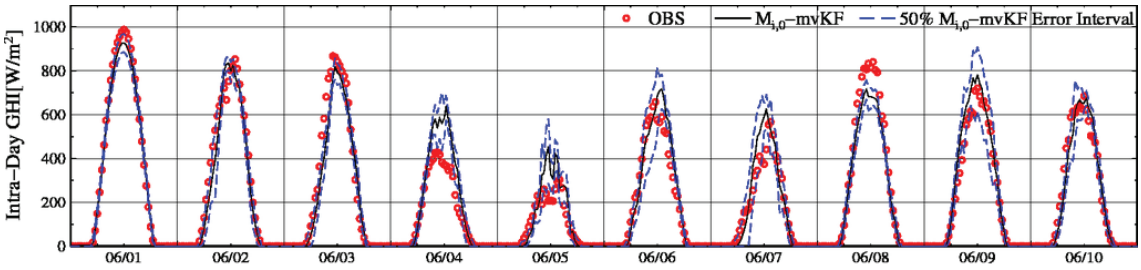

(b9") $M_{i,0}-mvKF$ and 50% prediction interval

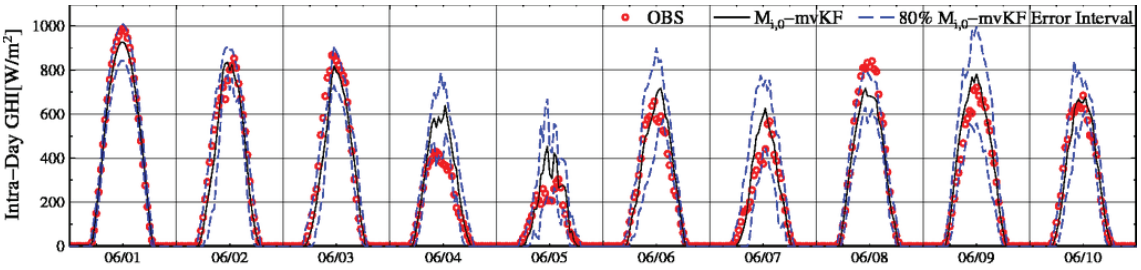

(c9") $M_{i,0}-mvKF$ and 80% prediction interval

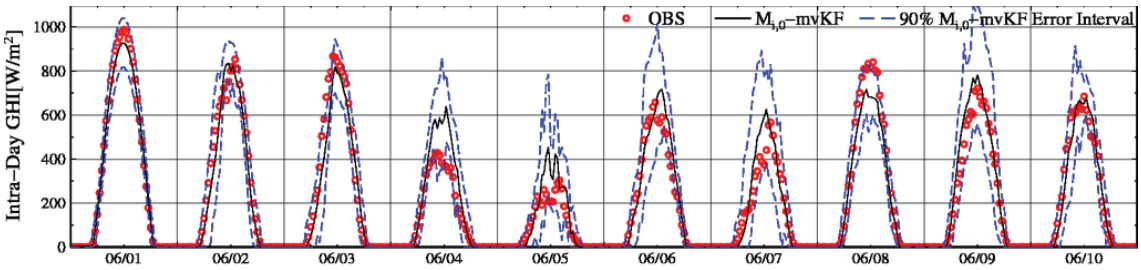

(d9") $M_{i,0}-mvKF$ and 90% prediction interval

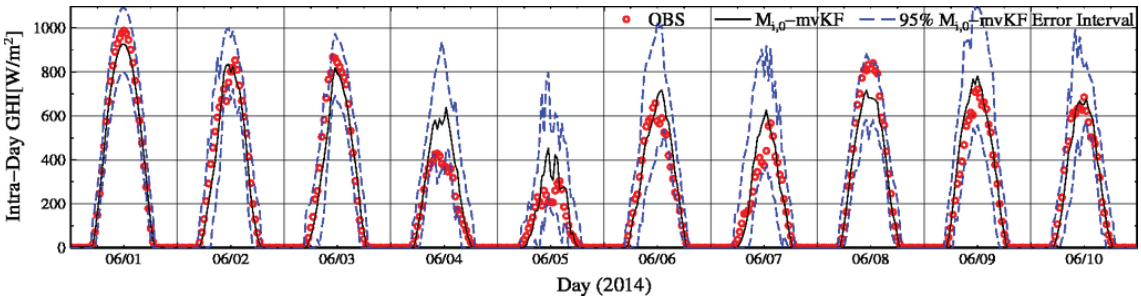

(e9") $M_{i,0}-mvKF$ and 95% prediction interval

Fig. C.9 Time series of observed and forecasted solar irradiance (GHI) and its 50%, 80%, 90%, 95% prediction interval for the intra-day forecasting $M_{i,0}-mvKF$ (61 observation-point average, from Jun 1st to 10th, 2014)

ACKNOWLEDGEMENTS

I would like to express my gratitude to all those who helped and encouraged me to complete this dissertation.

First of all, I would like to express my greatest gratitude to my supervisor, Prof. **Tomonao Kobayashi** at Graduate School of Engineering, Gifu University for the continuous support of my research. Without his patient instruction, insightful criticism and expert guidance, I could not finish writing my thesis. I gratefully acknowledge Assoc. Prof. **Jun Yoshino** for valuable suggestions and supports. Also, I would like to express my deepest appreciation to Dr. **Susumu Shimada** at National Institute of Advanced Industrial Science and Technology, Fukushima, who had helped and supported me a lot both academically and personally. His vision, rigorous attitude, enthusiasm and continual pursuit in research have always been an inspiration to me. I also want to thank all the members in Natural Energy Laboratory in Gifu University for their assistances and always being so helpful and friendly.

Furthermore, I would like to thank Prof. **Fusheng Li** who provided me an opportunity to study at Gifu University Rearing Program for Basin Water Environmental Leaders. I would also like to acknowledge the Japanese government (MEXT：Ministry of Education, Culture, Sports, Science and Technology) for financial support in the form of Monbukagakusho scholarship. Finally, I would also like to express my gratitude to my parents for their unconditional love, support, encouragement and dedication.

The observed solar irradiance (Global Horizontal Irradiance, GHI) data used in this work are measured by the Chubu Electric Power Co. Inc. under PV300 project, supported by the Ministry of Economy, Trade and Industry of Japan. I would like to express sincere gratitude to them here.